$\mathcal{H}_2$ and $\mathcal{H}_\infty$ Control of a Twin Lift Helicopter System

by

Carol J. Ouellette

B.S. Engineering, B.A. Mathematics
Swarthmore College (1996)

Submitted to the Department of Electrical Engineering and Computer Science
in partial fulfillment of the requirements for the degree of

Master of Science in Electrical Engineering and Computer Science

at the

MASSACHUSETTS INSTITUTE OF TECHNOLOGY

September 1999

Author .....
Department of Electrical Engineering and Computer Science
August 6, 1999

Certified by .....
Michael Athans
Professor of Electrical Engineering, Emeritus
Thesis Supervisor

Accepted by .....
Arthur C. Smith
Chairman, Department Committee on Graduate Students

$\mathcal{H}_2$ and $\mathcal{H}_\infty$ Control of a Twin Lift Helicopter System

by

Carol J. Ouellette

Submitted to the Department of Electrical Engineering and Computer Science
on August 6, 1999, in partial fulfillment of the
requirements for the degree of
Master of Science in Electrical Engineering and Computer Science

Abstract

The $\mathcal{H}_2$ (Linear Quadratic Gaussian) and $\mathcal{H}_\infty$ design methodologies are used to control a multi-input multi-output twin lift helicopter system (TLHS), consisting of two helicopters jointly carrying a payload. The control objectives include the rejection of specified external disturbances, and stability robustness to an unmodeled time delay. To achieve these objectives, the TLHS is incorporated into a generalized plant imposing frequency dependent weighting functions on selected control, disturbance, and output variables. Four different generalized plants are designed, two for $\mathcal{H}_2$ and two for $\mathcal{H}_\infty$ controller synthesis. Analysis of the resulting controllers reveals that both the $\mathcal{H}_2$ and $\mathcal{H}_\infty$ design methodologies, when used with frequency weightings, can meet the desired design specifications. Differences and performance trade offs amongst the controllers are shown to correlate intuitively with variations in the weighting functions and other parameters used in defining the generalized plant. In addition, the ability in $\mathcal{H}_\infty$ design, but not $\mathcal{H}_2$ design, to *directly* shape singular values, makes this former approach generally more efficient in producing the desired results. Suggestions for future work include applying and/or extending the methodologies in this thesis to design controllers for other multivariable linear systems.

Thesis Supervisor: Michael Athans
Title: Professor of Electrical Engineering, Emeritus

Acknowledgments

I have many people to thank for the completion of this thesis.

I would like to thank my thesis advisor, Michael Athans, who has been a constant source of encouragement and support, and a model of patience and understanding. I am extremely fortunate to have been his last graduate student advisee before his retirement from MIT.

I would like to thank my faculty advisor, Alan Willsky, the EECS department graduate administrators, and the MIT deans for graduate education, all of whom have shown particular care and concern for my well-being, academic and otherwise, during my time at MIT. Their support, understanding, and advice have been integral to my successfully completing this work.

I would like to thank Bethany Block, Margaret Ross, and Marcia Yousik for all of the care and kindness they have shown me during the last couple of years. I would not have earned my degree without them, and I will miss them dearly after I graduate.

Finally, I would like thank Randie Margolis, whose helpfulness to me throughout the writing of this thesis cannot be put into words. She has been a light for me during the darkest of times. And it is by that light that I continued to write, and continued to move forward. I am grateful and indebted to her for the encouragement she provided and the motivation she inspired.

This research was carried out at the Laboratory for Information and Decision Systems (LIDS) at MIT, and was supported financially by a Department of Defense (DOD) National Defense Science and Engineering Graduate (NDSEG) Fellowship.

Contents

List of Figures

List of Tables

Chapter 1

Introduction

1.1 Motivation

From fighting fires, to providing video surveillance of disaster areas, to transporting heavy cargo, the helicopter has become vital to achieving tasks in a wide variety of fields. As a means of transporting heavy cargo, in particular, the helicopter has seen use in tasks ranging from construction projects to military expeditions to natural disaster clean-ups. The increasing number and variety of such projects has led to a need for helicopters with increased power capable of transporting heavier cargo. The high costs associated with developing and producing such helicopters, however, have led engineers to search for a more economical alternative. This alternative is provided by the twin lift helicopter system (TLHS), in which two helicopters work together to transport a payload heavier than either could transport singly.

1.2 Previous Research

In the 1960's, recognizing the large expenditures required to produce helicopters with increased load capacities, the Department of Defense began investigating the possibility of joint helicopter lifting missions [1]. Advances in this area came in the late 1960's and early 1970's, when Sikorsky Aircraft demonstrated that twin lift operations using a spreader bar were feasible for short distances at low speeds. This demonstration involved a 20-ton twin lift configuration in which the command pilot, in the "master" helicopter, controls his helicopter while the "slave" helicopter is controlled automatically.

Some of the most recent research on twin lift helicopter dynamics was done in the 1980's by H. C. Curtiss (Princeton University) and F. W. Warburton (Sikorsky Aircraft) [1]. Together they developed a linear seven degree of freedom hover model for the longitudinal dynamics of a TLHS to study how changing parameters in the twin lift configuration affects the modes of motion and control response characteristics. This work was followed by that of Armando A. Rodriguez (MIT) who, for his Master's thesis, used this linearized model to develop a multi-input multi-output automatic flight control system (AFCS) for a TLHS consisting of two Sikorsky UH-60A Blackhawks [2]. After thoroughly analyzing the dynamics of the linearized model, Rodriguez used the Linear Quadratic Gaussian with Loop Transfer Recovery (LQG/LTR) methodology with integral control to develop an AFCS for two different TLHS configurations, one with equal and one with unequal helicopter tether lengths. In his designs, he demonstrated the trade off between desired performance and stability robustness to model uncertainty, and also showed that unequal tethered flight offers little advantage over equal tethered flight.

1.3 Contributions of Research

The research in this thesis applies the $\mathcal{H}_2$, or Linear Quadratic Gaussian (LQG), and $\mathcal{H}_\infty$ design methodologies to design automatic flight control systems for the TLHS model developed by Curtiss and Warburton. These two multivariable approaches to control design optimally minimize particular closed loop transfer function matrix norms [4], [5]. Within a generalized plant framework, frequency weightings on selected disturbance, control, and output variables are constructed to achieve specific objectives for performance and stability robustness. Final controller designs are analyzed in both the time and frequency domains, and performance trade offs interpreted in terms of variations in both the generalized plant and the synthesis method used. The results illustrate how the $\mathcal{H}_2$ and $\mathcal{H}_\infty$ design methodologies, used with frequency weightings, can provide an intuitive and efficient means within the multivariable setting for targeting and hence achieving specific requirements on closed loop system behavior.

1.4 Outline of Thesis

The remainder of the thesis is organized as follows:

Chapter 2 describes the model of the TLHS developed by Curtiss and Warburton. After the relevant variables, controls, and modeling parameters are introduced, the model is presented in state space form, linearized about hovering equilibrium.

Chapter 3 explores the open loop behavior of the TLHS model. The various motions of the TLHS are described in relation to the control commands and to the model structure. The natural modes of the TLHS are discussed and corresponding modal responses illustrated.

Chapter 4 explains the theory of $\mathcal{H}_2$ and $\mathcal{H}_\infty$ design. The framework of the generalized plant is introduced, and the $\mathcal{H}_2$ and $\mathcal{H}_\infty$ transfer function matrix norms are defined and interpreted. Synthesis methods for the two types of controllers are then presented, and characteristics of each discussed. The chapter concludes with a discussion of how appropriately chosen design weights incorporated into the generalized plant can lead to the more effective meeting of specific performance and stability robustness criteria. The discussion illustrates and motivates in particular depth the use of design weights in $\mathcal{H}_\infty$ design, where the singular values of various transfer functions can be shaped directly.

Chapter 5 presents the actual $\mathcal{H}_2$ and $\mathcal{H}_\infty$ generalized plant designs for the TLHS controllers. To motivate these designs, assumed external disturbances to the TLHS are described, and specifications given for the rejection of these disturbances. A specification is also given to ensure stability robustness to an unmodeled time delay of up to 0.05 s. After establishing the design specifications, four generalized plants, two for $\mathcal{H}_2$ and two for $\mathcal{H}_\infty$ synthesis, are described. The selection of design parameters and frequency weighting functions for these plants is explained with respect to the performance and stability robustness objectives.

Chapter 6 presents the resulting closed loop system behavior for each of the controller designs. The systems are analyzed in both the time and frequency domains, with their performance measured against the specifications put forward in chapter 5. Differences and performance trade offs amongst the controllers are interpreted in terms of variations in both the generalized plant parameters and synthesis method used. In the chapter's conclusion, the $\mathcal{H}_2$ and $\mathcal{H}_\infty$ design methodologies are each evaluated on their respective efficiency in achieving the desired performance objectives.

Chapter 7 summarizes the thesis and gives suggestions for future applications and/or extensions of the $\mathcal{H}_2$ and $\mathcal{H}_\infty$ controller design methodologies.

Chapter 2

Model of a Twin Lift Helicopter System

2.1 Model Configuration

The twin lift helicopter configuration to be studied is shown in Figure 2-1 [1]. This configuration is referred to as the *longitudinal configuration* because the longitudinal axes of the helicopters are parallel to the spreader bar.[1] In studying this configuration, it is assumed that the twin lift longitudinal dynamics decouple from the lateral motion. Each helicopter is modeled as a UH-60A Blackhawk, and the AFCS is designed to completely control both helicopters. The helicopter tethers are of equal length and are attached below the helicopters' centers of gravity (c. g.). The payload is suspended a fixed distance below the spreader bar by two equal length load cables. In modeling, the spreader bar is assumed rigid, while the tethers and load cables are assumed to always be in tension.

2.2 TLHS Variables and Controls

Because the TLHS longitudinal model developed by Curtiss and Warburton has seven degrees of freedom, the TLHS dynamics described by this model may be fully described by any seven independent variables. One possible choice for these variables is

(1) x_m : horizontal coordinate of master helicopter c. g. with respect to hover point,

[1]With a few simple variable substitutions, the same model can also be used to describe the case where the helicopter centerlines are perpendicular to the spreader bar.

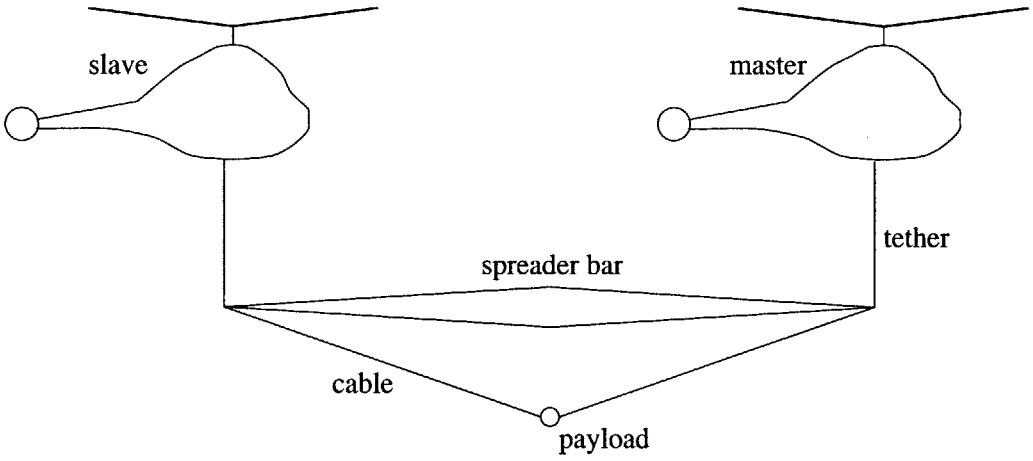

Figure 2-1: TLHS Longitudinal Configuration

(2) x_s : horizontal coordinate of slave helicopter c. g. with respect to hover point,

(3) z_m : vertical coordinate of master helicopter c. g. with respect to hover point,

(4) z_s : vertical coordinate of slave helicopter c. g. with respect to hover point,

(5) θ_m : pitch angle of master helicopter,

(6) θ_s : pitch angle of slave helicopter,

(7) $x_L - \Sigma x$: load deviation from center,

where Σx represents the average of the master and slave horizontal coordinate. These seven degrees of freedom correspond to the helicopters' horizontal motion (2), vertical motion (2), pitching motion (2), and to the horizontal motion of the load (1). Figure 2-2 [2] illustrates a visualization of these motions.

The longitudinal motion of the TLHS is governed by four independent helicopter controls. For control of vertical motion, each helicopter is equipped with a *collective pitch* control. This control affects lift by causing an increase in the angle with which the main rotor blades cut through the air [2]. The horizontal and pitching motions of each helicopter are controlled by a *cyclic pitch* control. This control operates by changing the point in the main rotor cycle at which maximum blade pitch occurs. The collective and cyclic controls are denoted:

(1) Θ_{cm} : master collective control,

(2) Θ_{cs} : slave collective control,

(3) B_{lcm} : master cyclic control,

(4) B_{lcs} : slave cyclic control.

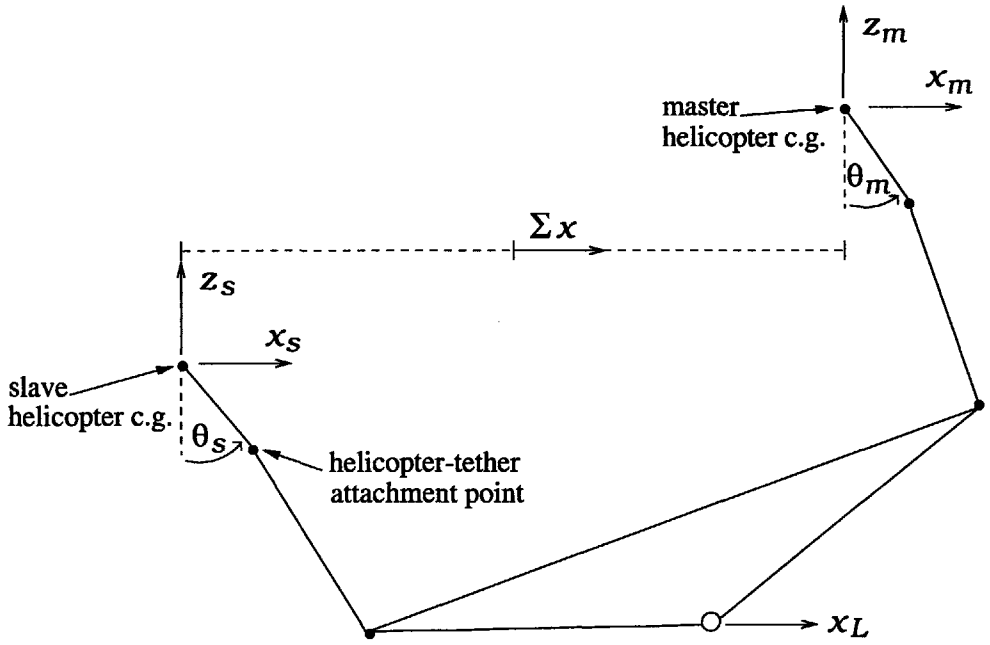

Figure 2-2: Visualization of TLHS Motions

In actuality, the collective and cyclic controls do exhibit coupling. For modeling purposes, however, this coupling is assumed to be small and hence is neglected.

2.3 TLHS Parameters and Derivatives

Table 2.1 lists the nominal values of the parameters needed to characterize the TLHS configuration. These parameters include geometric measurements as well as masses associated with the helicopters and load-bar assembly. The numerical values listed are identical to those used by Curtiss and Warburton and by Rodriguez. In addition to the parameters in Table 2.1, the linear model includes two sets of constants referred to respectively as *control derivatives* and *aerodynamic derivatives.* Control derivatives relate the action of the helicopters' collective and cyclic controls to the TLHS motion. Similarly, aerodynamic derivatives relate the aerodynamic forces and moments on the helicopters to the TLHS motion. Aerodynamic forces and moments acting on the spreader bar assembly and load are assumed negligible in comparison to those acting on the helicopters [2]. Table 2.2 lists the nominal values of the control and aerodynamic derivatives near hover. As was true of the TLHS parameter values, the derivative values are identical to those used by Curtiss and Warburton and by Rodriguez.

TLHS Parameters	Symbols	Nominal Values
helicopter mass	M_H	434.78 slugs
helicopter moment of inertia about pitch axis	I_y	434.78 slug $\cdot$ ft^2
distance from helicopter c. g. to helicopter-tether attachment point	h	3.6 ft
helicopter tether lengths	H	13.25 ft
spreader bar length	L	69 ft
spreader bar mass	M_B	20 slugs
distance of load below spreader bar c. g.	Z	34.5 ft
mass of load	M_L	372.67 slugs

Table 2.1: TLHS Nominal Parameter Values

TLHS Control Derivatives	Symbols	Nominal Values
horizontal acceleration per radian of cyclic	X_{Blc}	$27.4 \frac{ft}{rad \cdot s^2}$
vertical acceleration per radian of collective	$Z_{\Theta c}$	$340.9 \frac{ft}{rad \cdot s^2}$
angular acceleration per radian of cyclic	M_{Blc}	$-47.24 \frac{rad}{rad \cdot s^2}$
TLHS Aerodynamic Derivatives	**Symbols**	**Nominal Values**
characterization of horizontal drag forces due to horizontal motion	X_u	$-0.06 \frac{ft \cdot s^{-2}}{ft \cdot s^{-1}}$
characterization of vertical drag forces due to vertical motion	Z_w	$-0.346 \frac{ft \cdot s^{-2}}{ft \cdot s^{-1}}$
characterization of pitching moments due to forward motion	M_u	$0.041 \frac{rad \cdot s^{-2}}{ft \cdot s^{-1}}$
characterization of rotational damping due to pitching motion	M_q	$-3.1 \frac{rad \cdot s^{-2}}{rad \cdot s^{-1}}$

Table 2.2: Nominal Values of TLHS Control and Aerodynamic Derivatives

2.4 Development of Linear Model

The linear seven degree of freedom model used throughout this thesis originates from seven second order nonlinear ordinary differential equations written in terms of the aerodynamic forces and moments acting on the helicopters. These equations can be developed using the Lagrangian method [2]. The equations are then linearized about a hovering equilibrium with the tethers vertical and spreader bar horizontal as shown in Figure 2-1. To obtain this linearization, it is necessary to determine the equilibrium values of all motion variables, forces, and moments. Denoting these values with the subscript "o", we have

$$\dot{x}_{mo} = \dot{x}_{so} = 0, \tag{2.1}$$

$$\dot{z}_{mo} = \dot{z}_{so} = 0, \tag{2.2}$$

$$\theta_{mo} = \theta_{so} = 0,^{2} \tag{2.3}$$

$$x_{Lo} - \Sigma x_o = 0. \tag{2.4}$$

Each motion variable, force, and moment is then written as the sum of an equilibrium component and an incremental component, as in $x_m = x_{mo} + \delta x_m$. Neglecting products of the incremental components produces seven linear ordinary differential equations written in terms of the incremental variables. For notational convenience, the δ's on the incremental motion variables are dropped.

The seven linear differential equations developed thus far still include incremental aerodynamic forces and moments. These forces and moments are eliminated from the equations by writing each in terms of aerodynamic derivatives multiplied by incremental motion variables and control derivatives multiplied by incremental control variables. These substitutions then complete the development of the linearized model. It should be emphasized that the control variables appearing in this linear model represent deviations from the controls necessary to produce hovering equilibrium. Hence in writing $\Theta_{cm} = \Theta_{cmo} + \delta\Theta_{cm}$, where Θ_{cmo} is the equilibrium component of the master collective, it is $\delta\Theta_{cm}$ which appears in the final model. Throughout the thesis, the incremental collectives and cyclics are assumed to

[2]Condition (2.3) follows from an assumption that the helicopter main rotor shafts pass through their c. g.'s when at hover [2].

satisfy

$$|\delta\Theta_c| < 10^\circ \qquad \text{and} \qquad |\delta B_{lc}| < 15^\circ. \tag{2.5}$$

As with the motion variables, the δ's on the control variables shall be suppressed.

The linear model developed above may be written in a more convenient form by introducing alternative sets of TLHS motion and control variables. The seven new independent variables needed to describe the TLHS motion are defined as

(1) $\Sigma x \equiv \frac{x_m + x_s}{2}$: average horizontal helicopter coordinate,

(2) $\Sigma z \equiv \frac{z_m + z_s}{2}$: average vertical helicopter coordinate,

(3) $\Sigma\theta \equiv \frac{\theta_m + \theta_s}{2}$: average helicopter pitch angle,

(4) $\Delta x \equiv x_m - x_s$: horizontal separation between helicopters,

(5) $\Delta z \equiv z_m - z_s$: vertical separation between helicopters,

(6) $\Delta\theta \equiv \theta_m - \theta_s$: differential pitch angle,

(7) $x_L{}' \equiv x_L - \Sigma x - (\mathrm{h} + \mathrm{H})\,\Sigma\theta - \frac{\mathrm{Z}}{\mathrm{L}}\Delta z$: generalized load coordinate.

Similarly, the four new controls are defined as

(1) $\Sigma\Theta_c \equiv \frac{\Theta_{cm} + \Theta_{cs}}{2}$: average collective control,

(2) $\Sigma B_{lc} \equiv \frac{B_{lcm} + B_{lcs}}{2}$: average cyclic control,

(3) $\Delta\Theta_c \equiv \Theta_{cm} - \Theta_{cs}$: differential collective control,

(4) $\Delta B_{lc} \equiv B_{lcm} - B_{lcs}$: differential cyclic control.

Using these new variables has the advantage that the seven degree of freedom model decouples into three simpler subsystems. These subsystems are referred to respectively as the average vertical motion (AVM) plant, the symmetric motion (SM) plant, and the antisymmetric motion (ASM) plant. Elaborating upon the reasons for these names shall be postponed until chapter 3. The degrees of freedom and controls associated with each sub-

Plant	Degrees of Freedom	Controls
AVM	Σz	$\Sigma\Theta_c$
SM	Δx, $\Delta\theta$	ΔB_{lc}
ASM	Σx, $\Sigma\theta$, Δz, $x_L{}'$	ΣB_{lc}, $\Delta\Theta_c$

Table 2.3: Three Subsystems of TLHS Linear Model

system are listed in Table 2.3. Note that the newly introduced average and difference variables still represent *incremental* quantities, that is, perturbations from their equilibrium

counterparts.

For design purposes, it is most convenient to have a model in state space form. The seven degree of freedom linear model describing the TLHS longitudinal dynamics near hover can be transformed into a twelfth order state space model with three decoupled subsystems of orders one, four, and seven. This model is written:

$$\dot{\vec{x}}_p = A_p \vec{x}_p + B_p \vec{u}_p; \qquad \vec{x}_p \in \Re^{12},\ \vec{u}_p \in \Re^4, \tag{2.6}$$

where

$$\vec{x}_p \equiv \left[\ \Sigma\dot{z} \parallel \Delta x\ \Delta\theta\ \Delta\dot{x}\ \Delta\dot{\theta} \parallel \Sigma\theta\ \Delta z\ {x_L}'\ \Sigma\dot{x}\ \Sigma\dot{\theta}\ \Delta\dot{z}\ {\dot{x}_L}'\ \right]', \tag{2.7}$$

$$\vec{u}_p \equiv [\ \Sigma\Theta_c \parallel \Delta B_{lc} \parallel \Delta\Theta_c\ \Sigma B_{lc}\ ]', \tag{2.8}$$

$$
A_p = \begin{bmatrix}
\frac{Z_w}{1+\mu} & 0 & 0 & 0 & 0 & 0 & 0 & 0 & 0 & 0 & 0 & 0 \\
0 & 0 & 0 & 1 & 0 & 0 & 0 & 0 & 0 & 0 & 0 & 0 \\
0 & 0 & 0 & 0 & 1 & 0 & 0 & 0 & 0 & 0 & 0 & 0 \\
0 & -\mu\omega_A^2 & -\left(g(1+\mu)+\mu\omega_A^2 h\right) & X_u & 0 & 0 & 0 & 0 & 0 & 0 & 0 & 0 \\
0 & -\epsilon\mu\omega_A^2 & -\epsilon\mu\omega_A^2\,(h+H) & M_u & M_q & 0 & 0 & 0 & 0 & 0 & 0 & 0 \\
0 & 0 & 0 & 0 & 0 & 0 & 0 & 0 & 0 & 1 & 0 & 0 \\
0 & 0 & 0 & 0 & 0 & 0 & 0 & 0 & 0 & 0 & 1 & 0 \\
0 & 0 & 0 & 0 & 0 & 0 & 0 & 0 & 0 & 0 & 0 & 1 \\
0 & 0 & 0 & 0 & 0 & -g & 0 & \mu\omega_A^2 & X_u & 0 & 0 & 0 \\
0 & 0 & 0 & 0 & 0 & 0 & 0 & \epsilon\mu\omega_A^2 & M_u & M_q & 0 & 0 \\
0 & 0 & 0 & 0 & 0 & 4TH & -4T\hat{H} & 4T & 0 & 0 & Z_w TJ & 0 \\
0 & 0 & 0 & 0 & 0 & g & 4T\delta_L\hat{Z}\hat{H} & D & E & -M_q\,(h+H) & -Z_w TJ\delta_L\hat{Z} & 0
\end{bmatrix}, \tag{2.9}
$$

$$B_p = \begin{bmatrix} \frac{Z_{\Theta c}}{1+\mu} & 0 & 0 & 0 \\ 0 & 0 & 0 & 0 \\ 0 & 0 & 0 & 0 \\ 0 & X_{Blc} & 0 & 0 \\ 0 & M_{Blc} & 0 & 0 \\ 0 & 0 & 0 & 0 \\ 0 & 0 & 0 & 0 \\ 0 & 0 & 0 & 0 \\ 0 & 0 & 0 & X_{Blc} \\ 0 & 0 & 0 & M_{Blc} \\ 0 & 0 & Z_{\Theta c} TJ & 0 \\ 0 & 0 & -Z_{\Theta c} TJ\delta_L \hat{Z} & -(X_{Blc} + M_{Blc}(h+H)) \end{bmatrix}, \qquad (2.10)$$

with

$$\begin{aligned} \mu &\equiv \tfrac{M_L+M_B}{2M_H}, & \delta_L &\equiv \tfrac{M_L}{M_L+M_B}, & \omega_A^2 &\equiv \tfrac{g}{H},^3 \\ \hat{H} &\equiv \tfrac{H}{L}, & \epsilon &\equiv \tfrac{M_H h}{I_y}, & \hat{Z} &\equiv \tfrac{Z}{L}, \\ e_b &\equiv \tfrac{2I_B}{M_H L^2}, & I_B &\equiv \tfrac{1}{12M_B L^2}, & J &\equiv \tfrac{1}{\mu\delta_L \hat{Z}\omega_A^2}, \\ \Psi &\equiv 1 + e_b + 4\mu\hat{Z}^2\delta_L(1-\delta_L), & T &\equiv \tfrac{1}{J\Psi}, & F &\equiv -\omega_A^2 H - 4T\delta_L \hat{Z} H, \\ E &\equiv -(X_u + M_u(h+H)), & D &\equiv -\omega_A^2\left(1+\mu+(h+H)\mu\epsilon + \tfrac{4T\delta_L\hat{Z}}{\omega_A^2}\right). \end{aligned}$$

The symbol $\|$ is used to partition the state and control vectors in (2.7) and (2.8) into the three decoupled subsystems. The superscript "$\prime$" outside of the brackets in these equations denotes the vector transpose. Using the parameter and derivative values listed in Tables 2.1 and 2.2, and changing units from radians to degrees, the matrices A_p and B_p are given numerically by

[3] $g = 32.2 \frac{ft}{s^2}$ is the acceleration due to gravity.

$$
\mathrm{A}_p = \begin{bmatrix}
-0.2384 & 0 & 0 & 0 & 0 & 0 & 0 & 0 & 0 & 0 & 0 & 0 \\
0 & 0 & 0 & 1.000 & 0 & 0 & 0 & 0 & 0 & 0 & 0 & 0 \\
0 & 0 & 0 & 0 & 1.000 & 0 & 0 & 0 & 0 & 0 & 0 & 0 \\
0 & -1.097 & -0.8847 & -0.0600 & 0 & 0 & 0 & 0 & 0 & 0 & 0 & 0 \\
0 & -17.27 & -5.078 & 2.349 & -3.100 & 0 & 0 & 0 & 0 & 0 & 0 & 0 \\
0 & 0 & 0 & 0 & 0 & 0 & 0 & 0 & 0 & 1.000 & 0 & 0 \\
0 & 0 & 0 & 0 & 0 & 0 & 0 & 0 & 0 & 0 & 1.000 & 0 \\
0 & 0 & 0 & 0 & 0 & 0 & 0 & 0 & 0 & 0 & 0 & 1.000 \\
0 & 0 & 0 & 0 & 0 & -0.5620 & 0 & 1.097 & -.0600 & 0 & 0 & 0 \\
0 & 0 & 0 & 0 & 0 & 0 & 0 & 17.27 & 2.349 & -3.100 & 0 & 0 \\
0 & 0 & 0 & 0 & 0 & 0.4679 & -0.3885 & 2.023 & 0 & 0 & -0.3361 & 0 \\
0 & 0 & 0 & 0 & 0 & -0.2220 & 0.1844 & -9.565 & -0.6308 & 0.9117 & 0.1595 & 0
\end{bmatrix}, \qquad (2.11)
$$

$$B_p = \begin{bmatrix} 4.099 & 0 & 0 & 0 \\ 0 & 0 & 0 & 0 \\ 0 & 0 & 0 & 0 \\ 0 & 0.4782 & 0 & 0 \\ 0 & -47.24 & 0 & 0 \\ 0 & 0 & 0 & 0 \\ 0 & 0 & 0 & 0 \\ 0 & 0 & 0 & 0 \\ 0 & 0 & 0 & 0.4782 \\ 0 & 0 & 0 & -47.24 \\ 0 & 0 & 5.779 & 0 \\ 0 & 0 & -2.743 & 13.41 \end{bmatrix}. \tag{2.12}$$

All AFCS designs in this thesis are developed for the above state space model.

Chapter 3

Open Loop Analysis of TLHS Model

3.1 The Three Subsystems

The state space model presented in chapter 2 decouples into three subsystems, referred to respectively as the AVM plant, the SM plant, and the ASM plant. The AVM plant is of first order and describes the motion of the average vertical velocity of the helicopters ($\Sigma\dot{z}$). This motion is controlled by the average collective command ($\Sigma\Theta_c$). The SM plant is of fourth order and involves the Δx and $\Delta\theta$ degrees of freedom. Hence this plant describes that motion of the helicopters which is symmetric about the equilibrium configuration. This motion is controlled by the differential cyclic command (ΔB_{lc}). The ASM plant is of seventh order and involves the Σx, $\Sigma\theta$, Δz, and $x_L{}'$ degrees of freedom. Hence this plant describes the TLHS motion which is not symmetric about the equilibrium configuration. This motion is controlled by the differential collective ($\Delta\Theta_c$) and average cyclic (ΣB_{lc}) commands. Figures 3-1 and 3-2 [2] illustrate the TLHS motion associated with the SM and ASM plants respectively.

3.2 Natural Modes

The natural modes of the TLHS linear system are found by solving the homogeneous system (no commands issued)

$$\dot{\vec{x}}(t) = A_p\vec{x}(t); \qquad \vec{x}(0) = \vec{x}_0 \in \Re^{12}. \tag{3.1}$$

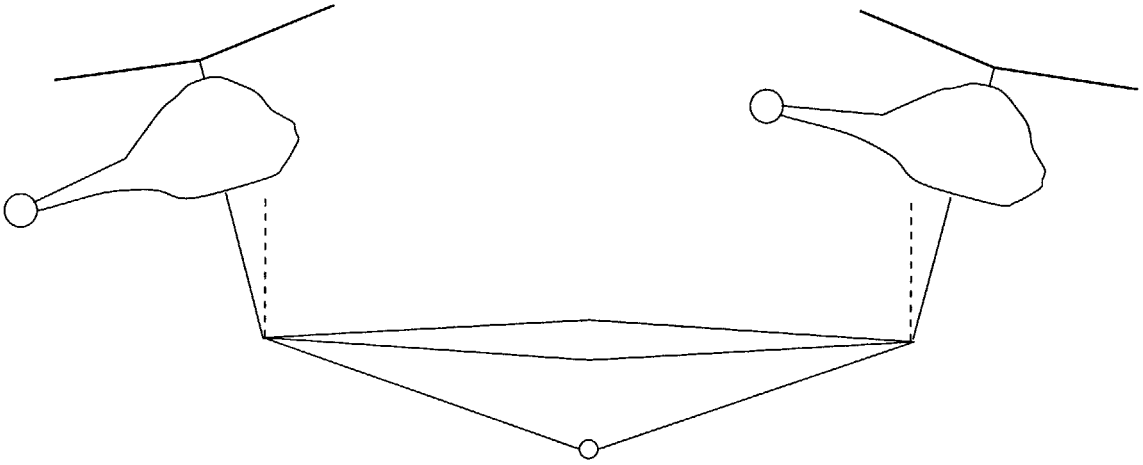

Figure 3-1: Visualization of TLHS Symmetric Motion

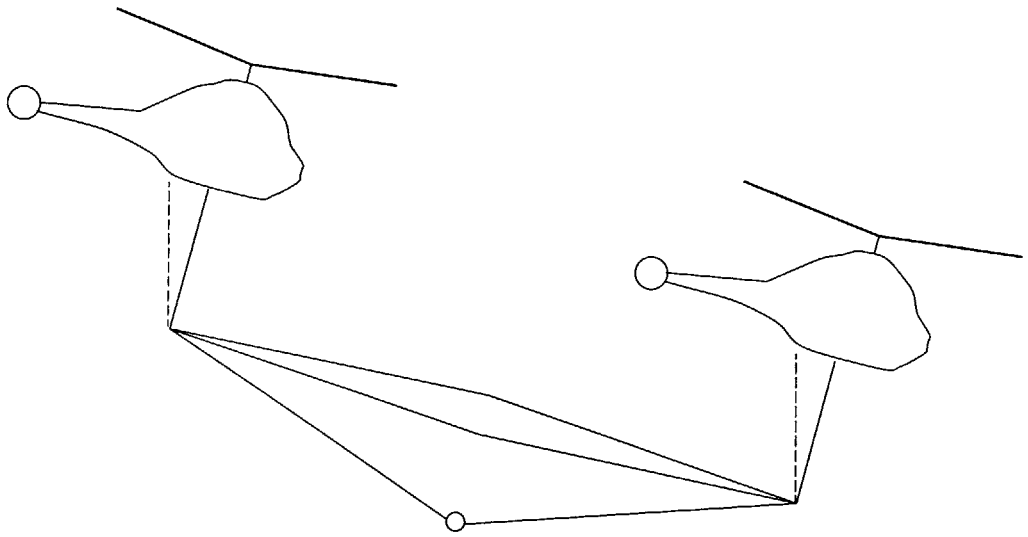

Figure 3-2: Visualization of TLHS Anti-Symmetric Motion

Identifying each mode by λ_i, $i = 1, 2, \ldots, 12$, and assuming A_p is diagonalizable, the solution of (3.1) is given by

$$\vec{x}(t) = e^{A_p t}\vec{x}_0 = \sum_{i=1}^{12} e^{\lambda_i t}\vec{v}_i \left(\vec{w}_i{}'\vec{x}_0\right), \tag{3.2}$$

where the superscript "$'$" denotes the complex conjugate transpose, and $\vec{v}_i$ and $\vec{w}_i$ are respectively the right and left eigenvectors of A_p associated with the eigenvalue λ_i. Because

$$\vec{w}_i{}'\vec{v}_j = \begin{cases} 1 & \text{if } i = j \\ 0 & \text{if } i \neq j \end{cases}, \tag{3.3}$$

it follows that

$$\vec{x}_0 = \vec{v}_i \qquad \Longrightarrow \qquad \vec{x}(t) = e^{\lambda_i t}\vec{v}_i. \tag{3.4}$$

In the case of complex modes $\lambda_{i,\,i+1} = \sigma \pm j\omega$, with associated eigenvectors $\vec{v}_{i,\,i+1} = \vec{a} \pm j\vec{b}$, where $\vec{a}$, $\vec{b} \in \Re^{12}$, it can be shown that

$$\begin{aligned} \vec{x}_0 &= k_1\vec{a} + k_2\vec{b}; \qquad k_1,\ k_2 \in \Re \qquad \Longrightarrow \\ \vec{x}(t) &= \sqrt{k_1^2 + k_2^2}\, e^{\sigma t}\left[\vec{a}\cos\left(\omega t - \arctan\left(\tfrac{k_2}{k_1}\right)\right) - \vec{b}\sin\left(\omega t - \arctan\left(\tfrac{k_2}{k_1}\right)\right)\right]. \end{aligned} \tag{3.5}$$

The natural modes and corresponding eigenvectors of the TLHS linear model are listed in Table 3.1. A plot of these modes, shown in Figure 3-3, reveals that the SM and ASM plants are both unstable in the open loop. Figures 3-4 through 3-6 illustrate several of the TLHS modal responses. In Figure 3-4, equation (3.1) is solved with $\vec{x}_0 = \vec{v}_1$. As predicted by (3.4), $\Sigma\dot{z}$ decays exponentially with a time constant (τ) of 4.25 s, while all the other states remain identically equal to zero. Figure 3-5 shows the solution of (3.1) with $\vec{x}_0 = \vec{v}_2$. Again, as predicted by (3.4), the states of the SM system grow exponentially ($\lambda_2 > 0$) with $\tau = 1.32$ s. Also predicted by (3.4), the response remains pointed in the direction of $\vec{v}_2$, and thus the states of the AVM and ASM systems remain identically equal to zero. To illustrate a TLHS response associated with complex conjugate eigenvalues, Figure 3-6 shows the solution of (3.1) with $\vec{x}_0 = \mathrm{Re}\,[\vec{v}_{10}] + \mathrm{Im}\,[\vec{v}_{10}]$. As predicted by (3.5), the seven states of the AVM system respond as damped sinusoids with $\tau = 1.88$ s and an oscillation frequency of 2.62 rad/s. A more in depth discussion of the TLHS natural modes can be found in [2].

Plant	AVM	SM			ASM			
i	1	2	3, 4	5	6, 7	8, 9	10, 11	12
Eigenvalues (λ_i)	-0.2384	0.7561	$-0.8121 \pm \jmath 2.2226$	-2.2919	$0.0402 \pm \jmath 0.4785$	$-0.1976 \pm \jmath 0.7364$	$-0.5313 \pm \jmath 2.6243$	-2.1187
Eigenvectors ($\vec{v}_i$)	1.	0.	0.	0.	0.	0.	0.	0.
	0.	-0.3658	$0.0078 \mp \jmath 0.0709$	-0.0564	0.	0.	0.	0.
	0.	0.7088	$0.3071 \mp \jmath 0.2283$	0.3959	0.	0.	0.	0.
	0.	-0.2766	$0.1512 \pm \jmath 0.0749$	0.1292	0.	0.	0.	0.
	0.	0.5360	$0.2580 \pm \jmath 0.8680$	-0.9074	0.	0.	0.	0.
	0.	0.	0.	0.	$-0.2167 \mp \jmath 0.2855$	$-0.0400 \pm \jmath 0.3966$	$0.3000 \mp \jmath 0.0219$	-0.4158
	0.	0.	0.	0.	$-0.7465 \pm \jmath 0.0850$	$-0.0932 \mp \jmath 0.6216$	$0.0148 \mp \jmath 0.0306$	-0.0124
	0.	0.	0.	0.	$-0.0227 \mp \jmath 0.0002$	$0.0042 \mp \jmath 0.0341$	$-0.1450 \pm \jmath 0.0879$	0.0706
	0.	0.	0.	0.	$0.3615 \mp \jmath 0.1267$	$-0.3482 \pm \jmath 0.0282$	$0.0619 \pm \jmath 0.1138$	-0.1512
	0.	0.	0.	0.	$0.1279 \mp \jmath 0.1152$	$-0.2841 \mp \jmath 0.1079$	$-0.1019 \pm \jmath 0.7899$	0.8809
	0.	0.	0.	0.	$-0.0707 \mp \jmath 0.3538$	$0.4762 \pm \jmath 0.0542$	$0.0725 \pm \jmath 0.0551$	0.0263
	0.	0.	0.	0.	$-0.0008 \mp \jmath 0.0109$	$0.0243 \pm \jmath 0.0098$	$-0.1536 \mp \jmath 0.4272$	-0.1297

Table 3.1: Eigenvalues and Eigenvectors of TLHS Linear Model

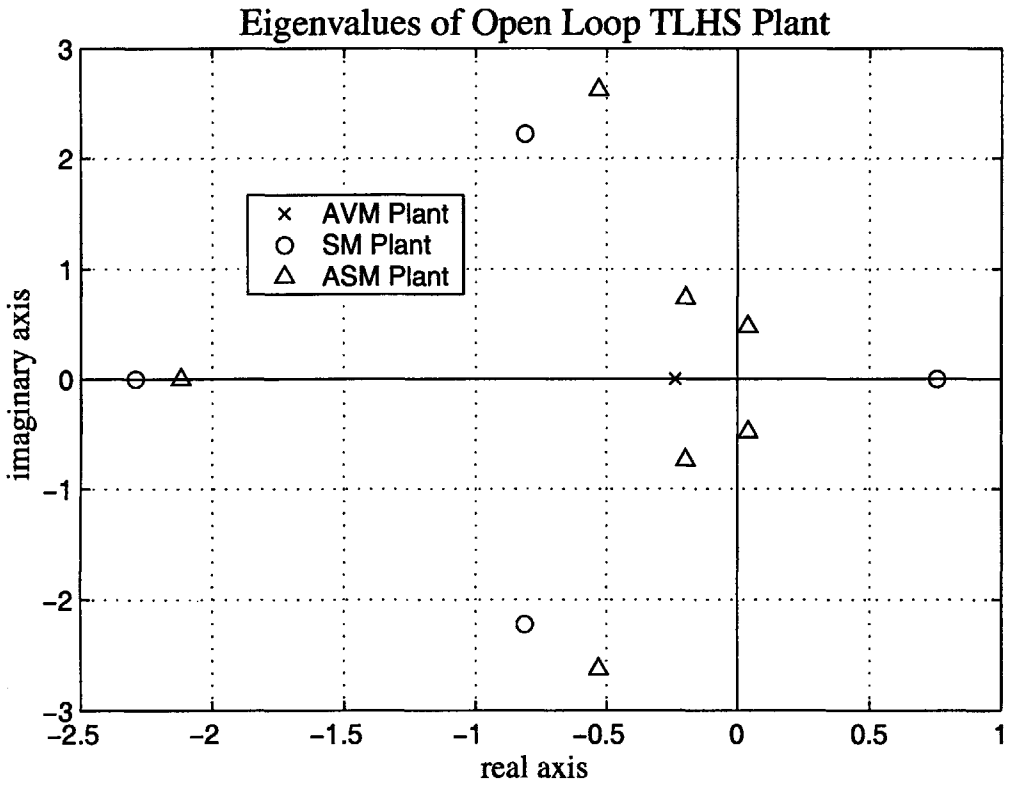

Figure 3-3: Natural Modes of Linearized TLHS Model

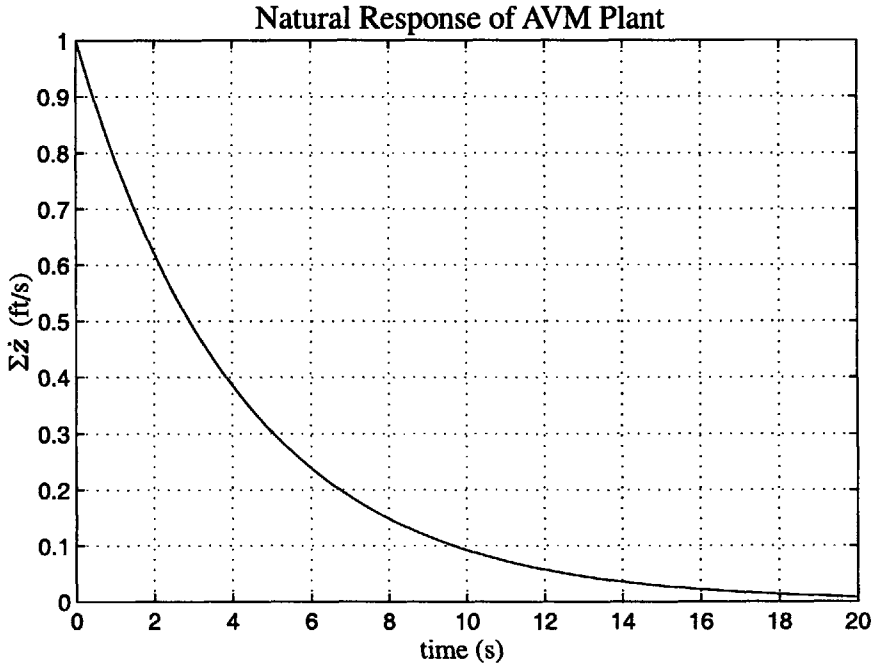

Figure 3-4: Natural Response of AVM Plant: $\vec{x}_0 = \vec{v}_1$

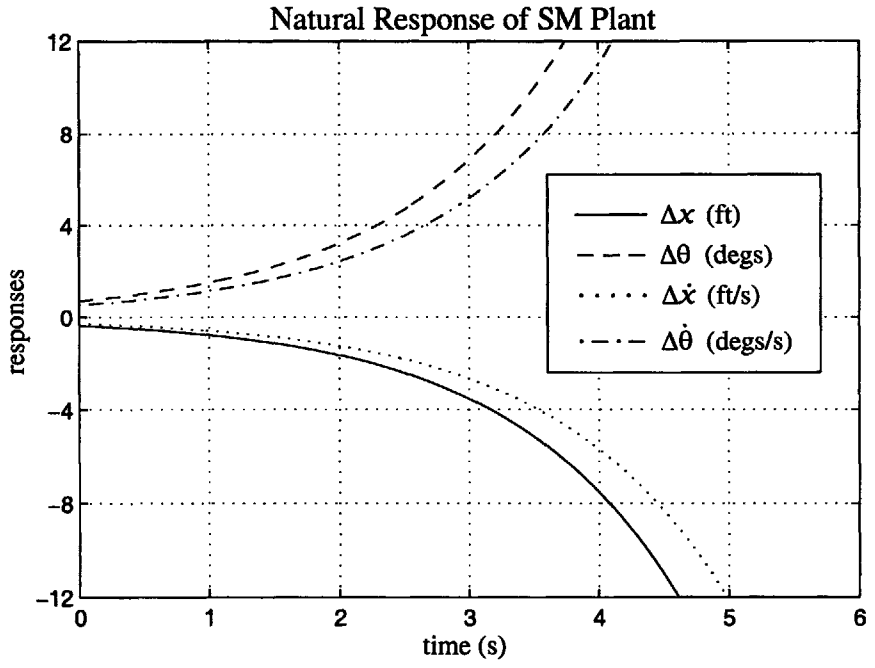

Figure 3-5: Natural Response of SM Plant: $\vec{x}_0 = \vec{v}_2$

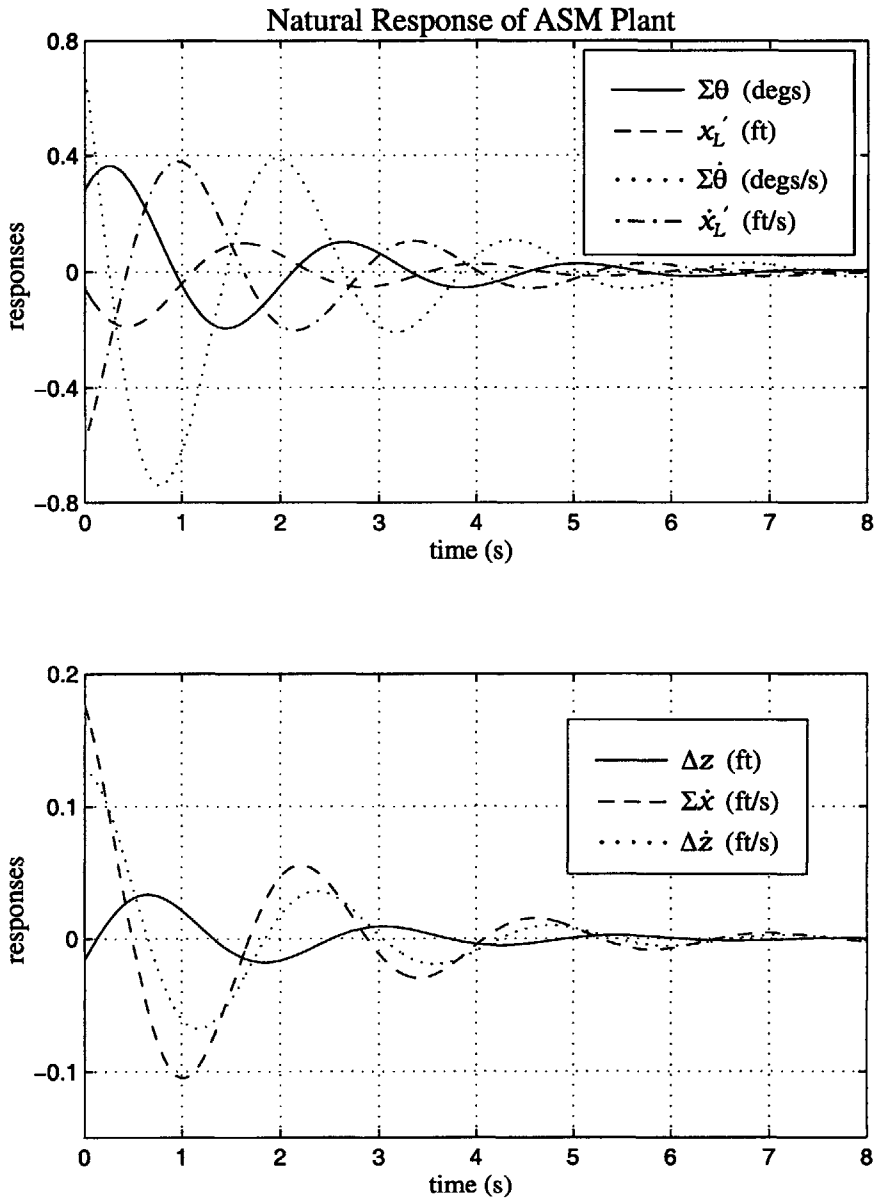

Figure 3-6: Natural Response of ASM Plant: $\vec{x}_0 = \mathrm{Re}\,[\vec{v}_{10}] + \mathrm{Im}\,[\vec{v}_{10}]$

3.3 Selection of Outputs

The outputs of the TLHS are those states or linear combinations of states which will be measured and used as inputs to the AFCS. It will be assumed as well that weighted versions of only these outputs (i. e. no other linear combinations of states) can be included among the performance variables to be penalized in the designs' cost functionals. Therefore, the best selection of outputs will include those quantities most important to regulate. With only

four independent controls, however, selections of greater than four outputs will necessitate performance trade offs among these outputs. Factors governing output selection, as well as the specific choices of outputs used for controller design, will be discussed further in chapter 5.

Chapter 4

$\mathcal{H}_2$ (LQG) and $\mathcal{H}_\infty$ Design Methodology

4.1 The Generalized Plant

Before describing the methodologies used to control the TLHS, it is necessary to introduce the framework under which the designs are developed. Throughout this thesis, the TLHS is incorporated into a generalized plant P with exogenous inputs w and performance

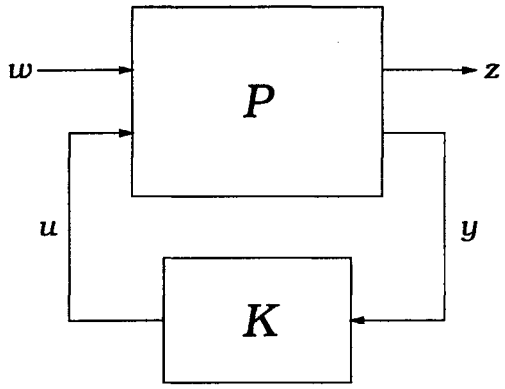

Figure 4-1: Block Diagram of Generalized Plant

variables z, as shown in Figure 4-1 [4], [5]. The inputs to the controller K are noisy sensor measurements y, and the controller generated plant inputs are denoted by u. In general, w, z, y, and u are vectors. To simplify notation, however, the overhead arrow will be suppressed through the remainder of the thesis. In addition to the nominal model of the TLHS, the

generalized plant incorporates design weights on selected disturbance, control, and output variables. These weightings reflect the performance and stability robustness desired from the control system. The goal of $\mathcal{H}_2$ and $\mathcal{H}_\infty$ syntheses within this framework is to minimize the "size" of the closed loop transfer function $T_{zw}(s)$. The norms used to measure the size of this transfer function matrix are what differentiate the two methodologies.

4.2 System Norms

4.2.1 Introduction

A norm of a transfer function matrix $G(s)$ is a non-negative real number which quantifies the size of $G(s)$ over all complex numbers s. In this discussion, $G(s)$ is assumed to be a stable, linear, time-invariant system with the state space representation

$$\begin{aligned} \dot{x}(t) &= Ax(t) + Bw(t), \\ y(t) &= Cx(t), \end{aligned} \tag{4.1}$$

where $x(t)$, $w(t)$, and $y(t)$ may be scalar or vector quantities. It follows that $G(s)$ may be written as

$$G(s) = C\,(sI - A)^{-1}\,B. \tag{4.2}$$

4.2.2 $\mathcal{H}_2$ Norms

The $\mathcal{H}_2$ norm of a stable transfer function matrix $G(s)$, denoted $\|G\|_2$, is defined as

$$\|G\|_2 = \left(\frac{1}{2\pi}\int_{-\infty}^{\infty} \text{trace}[G(\jmath\omega)G'(\jmath\omega)]\text{d}\omega\right)^{\frac{1}{2}} = \left(\frac{1}{2\pi}\int_{-\infty}^{\infty}\sum_{i=1}^{r}\sigma_i^2[G(\jmath\omega)]\text{d}\omega\right)^{\frac{1}{2}}, \tag{4.3}$$

where σ_i denotes the i-th singular value, $G'(\jmath\omega)$ is the complex conjugate transpose of $G(\jmath\omega)$, and r is the rank of $G(\jmath\omega)$ [4], [5]. Hence minimizing the $\mathcal{H}_2$ norm is equivalent to minimizing the area under the sum of the squared singular values of $G(\jmath\omega)$, with this sum plotted versus ω.

In the stochastic setting, the $\mathcal{H}_2$ norm has an especially useful interpretation. If $w(t)$ is zero mean, unit intensity white noise, then $y(t)$ (in steady state) is also a zero mean

stochastic process, and

$$\|G\|_2 = \left(\mathrm{E}\left[y'(t)y(t)\right]\right)^{\frac{1}{2}} = \left(\mathrm{trace}\left[\mathrm{cov}\left[y(t);y(t)\right]\right]\right)^{\frac{1}{2}}. \tag{4.4}$$

In equation (4.4), "E" denotes the expected value and "cov" denotes the covariance matrix. Hence the squared $\mathcal{H}_2$ norm equals the sum of the steady state variances of the components of $y(t)$, given a unit intensity white noise input. In the case of a scalar output, $\|G\|_2$ equals the steady state Root Mean Squared (RMS) value of $y(t)$.

The above interpretation allows the $\mathcal{H}_2$ norm to be computed in a straightforward manner [4]. From stochastic systems theory, it is known that if the system $G(s)$ is driven by zero mean, unit intensity white noise, then (in steady state)

$$\mathrm{cov}\left[y(t);y(t)\right] = C\,\Sigma_x C', \tag{4.5}$$

where Σ_x is the state covariance matrix (in steady state) and is found by solving the Lyapunov equation

$$A\Sigma_x + \Sigma_x A' + BB' = 0. \tag{4.6}$$

Hence $\|G\|_2$ is calculated using equations (4.5) and (4.6) together with (4.4). This method of computing $\|G\|_2$ is clearly far simpler than a computation done directly from the definition in (4.3).

4.2.3 $\mathcal{H}_\infty$ Norms

The $\mathcal{H}_\infty$ norm of a stable transfer function matrix $G(s)$, denoted $\|G\|_\infty$, is defined as

$$\|G\|_\infty = \sup_\omega \sigma_{\max}[G(j\omega)]. \tag{4.7}$$

Hence minimizing the $\mathcal{H}_\infty$ norm is equivalent to minimizing the peak of the maximum singular value of $G(j\omega)$, when plotted versus ω. The $\mathcal{H}_\infty$ norm may be interpreted as representing the largest possible amplification by $G(s)$ of a unit sinusoid input. It is also a measure of the maximum energy amplification by $G(s)$ of finite energy ($\mathcal{L}_2$) inputs [6].

Computation of the $\mathcal{H}_\infty$ norm can be done using an iterative procedure which relies on the following theorem [5].

Theorem 4.1 *For the transfer function* $G(s) = C(sI - A)^{-1}B$ *with* A *stable and* $\gamma > 0$, $\|G\|_\infty < \gamma$ *if and only if the Hamiltonian matrix*

$$H = \begin{bmatrix} A & \frac{1}{\gamma^2}BB' \\ -C'C & -A' \end{bmatrix} \tag{4.8}$$

has no eigenvalues on the $j\omega$*-axis.*

By Theorem 4.1, $\|G\|_\infty = \gamma_{\min}$, where $\gamma_{\min}$ is the infimum over all γ such that (4.8) has no eigenvalues on the $j\omega$-axis. This infimum can be computed within a desired tolerance with a bisection search over γ.

Because the $\mathcal{H}_\infty$ norm measures the maximum energy amplification of $\mathcal{L}_2$ signals, it is (unlike the $\mathcal{H}_2$ norm) a true induced norm. As a consequence, the $\mathcal{H}_\infty$ norm satisfies the following two properties [4].

Property 4.1

$$\|G\|_\infty < \gamma \quad \Longrightarrow \quad \|G_{i,j}\|_\infty < \gamma \;\forall\; i,\; j \tag{4.9}$$

where $G_{i,j}$ *denotes a submatrix of the stable, linear, time-invariant transfer function matrix* G.

Property 4.2 (Submultiplicative Property) *Given two stable, linear, time-invariant transfer function matrices* G_1 *and* G_2,

$$\|G_1 G_2\|_\infty \leq \|G_1\|_\infty \|G_2\|_\infty. \tag{4.10}$$

During $\mathcal{H}_\infty$ synthesis, Property 4.1 enables frequency weightings to directly shape the maximum singular values (as functions of ω) of transfer functions between various TLHS inputs and outputs. Hence the $\mathcal{H}_\infty$ design can be explicitly targeted to meet specific performance and stability robustness bounds.

4.3 $\mathcal{H}_2$ and $\mathcal{H}_\infty$ Controllers

$\mathcal{H}_2$ and $\mathcal{H}_\infty$ syntheses produce controllers K which minimize respectively the closed loop transfer function matrix norms $\|T_{zw}\|_2$ and $\|T_{zw}\|_\infty$ of the generalized plant introduced in

section 4.1. The procedures for constructing $\mathcal{H}_2$ and $\mathcal{H}_\infty$ controllers are relatively simple once the generalized plant P has been defined.

4.3.1 Assumptions on the Generalized Plant

The generalized plant P is assumed to have the state space realization

$$P \equiv \left[\begin{array}{c|cc} A & B_1 & B_2 \\ \hline C_1 & D_{11} & D_{12} \\ C_2 & D_{21} & D_{22} \end{array}\right], \tag{4.11}$$

which is shorthand for

$$\begin{aligned} \dot{x}(t) &= Ax(t) + B_1 w(t) + B_2 u(t), \\ z(t) &= C_1 x(t) + D_{11} w(t) + D_{12} u(t), \\ y(t) &= C_2 x(t) + D_{21} w(t) + D_{22} u(t). \end{aligned} \tag{4.12}$$

The following assumptions are then made on P.

Assumptions on P

(A.1) $D_{11} = 0$.[1]

(A.2) $[A\ B_2]$ is stabilizable and $[A\ C_2]$ is detectable.

(A.3) $[A\ B_1]$ is stabilizable and $[A\ C_1]$ is detectable.

(A.4) $V \equiv \left[\begin{array}{c} B_1 \\ D_{21} \end{array}\right] [B_1' D_{21}'] \equiv \left[\begin{array}{cc} V_{xx} & V_{xy} \\ V_{xy}' & V_{yy} \end{array}\right] \geq 0$ with $V_{yy} > 0$.

(A.5) $R \equiv \left[\begin{array}{c} C_1' \\ D_{12}' \end{array}\right] [C_1 D_{12}] \equiv \left[\begin{array}{cc} R_{xx} & R_{xu} \\ R_{xu}' & R_{uu} \end{array}\right] \geq 0$ with $R_{uu} > 0$.

[1] This assumption may be removed for $\mathcal{H}_\infty$ synthesis [5].

4.3.2 $\mathcal{H}_2$ Synthesis

Given the generalized plant P defined by (4.11) and satisfying (A.1)-(A.5), the unique, stabilizing, optimal controller which minimizes the $\mathcal{H}_2$ norm of $T_{zw}(s)$ is

$$K_2 \equiv \left[\begin{array}{c|c} A + B_2F_2 + L_2C_2 + L_2D_{22}F_2 & -L_2 \\ \hline F_2 & 0 \end{array}\right], \tag{4.13}$$

where

$$F_2 = -R_{uu}^{-1}\left(R_{xu}' + B_2'X_2\right), \qquad L_2 = -\left(Y_2C_2' + V_{xy}\right)V_{yy}^{-1}, \tag{4.14}$$

and X_2 and Y_2 are the unique, positive, semi-definite solutions to the Riccati equations

$$0 = X_2A_r + A_r'X_2 + R_{xx} - R_{xu}R_{uu}^{-1}R_{xu}' - X_2B_2R_{uu}^{-1}B_2'X_2, \tag{4.15}$$

$$0 = A_eY_2 + Y_2A_e' + V_{xx} - V_{xy}V_{yy}^{-1}V_{xy}' - Y_2C_2'V_{yy}^{-1}C_2Y_2, \tag{4.16}$$

where

$$A_r = A - B_2R_{uu}^{-1}R_{xu}' \qquad \text{and} \qquad A_e = A - V_{xy}V_{yy}^{-1}C_2. \tag{4.17}$$

4.3.3 $\mathcal{H}_\infty$ Synthesis

Given the generalized plant P defined by (4.11) and satisfying (A.1)-(A.5), a stabilizing controller which satisfies $\|T_{zw}\|_\infty < \gamma$ is

$$K_\infty \equiv \left[\begin{array}{c|c} A + (B_1 + L_\infty D_{21})W_\infty + B_2F_\infty + Z_\infty L_\infty C_2 + Z_\infty L_\infty D_{22}F_\infty & -Z_\infty L_\infty \\ \hline F_\infty & 0 \end{array}\right], \tag{4.18}$$

where

$$F_\infty = -R_{uu}^{-1}\left(R_{xu}' + B_2'X_\infty\right), \qquad W_\infty = \frac{1}{\gamma^2}B_1'X_\infty, \tag{4.19}$$

$$L_\infty = -\left(Y_\infty C_2' + V_{xy}\right)V_{yy}^{-1}, \qquad Z_\infty = \left(I - \frac{1}{\gamma^2}Y_\infty X_\infty\right)^{-1}, \tag{4.20}$$

and X_∞ and Y_∞ are the solutions to the Riccati equations

$$0 = X_\infty A_r + A_r'X_\infty + R_{xx} - R_{xu}R_{uu}^{-1}R_{xu}' - X_\infty\left(B_2R_{uu}^{-1}B_2' - \frac{1}{\gamma^2}B_1B_1'\right)X_\infty, \tag{4.21}$$

$$0 = A_eY_\infty + Y_\infty A_e' + V_{xx} - V_{xy}V_{yy}^{-1}V_{xy}' - Y_\infty\left(C_2'V_{yy}^{-1}C_2 - \frac{1}{\gamma^2}C_1'C_1\right)Y_\infty, \tag{4.22}$$

that satisfy the following conditions.

(C.1) $X_\infty \geq 0$.

(C.2) The Hamiltonian matrix for (4.21),

$$\begin{bmatrix} A_r & -B_2 R_{uu}^{-1} B_2' + \frac{1}{\gamma^2} B_1 B_1' \\ -R_{xx} + R_{xu} R_{uu}^{-1} R_{xu}' & -A_r' \end{bmatrix}, \tag{4.23}$$

has no $j\omega$-axis eigenvalues, or equivalently, $A + B_1 W_\infty + B_2 F_\infty$ is stable.

(C.3) $Y_\infty \geq 0$.

(C.4) The Hamiltonian matrix for (4.22),

$$\begin{bmatrix} A_e' & -C_2' V_{yy}^{-1} C_2 + \frac{1}{\gamma^2} C_1' C_1 \\ -V_{xx} + V_{xy} V_{yy}^{-1} V_{xy}' & -A_e \end{bmatrix}, \tag{4.24}$$

has no $j\omega$-axis eigenvalues, or equivalently, $A + L_\infty C_2 + \frac{1}{\gamma^2} Y_\infty C_1' C_1$ is stable.

(C.5) $\rho[Y_\infty X_\infty] < \gamma^2$, where $\rho[\,\cdot\,]$ is the spectral radius.

The optimal $\mathcal{H}_\infty$ controller results from constructing K_∞ with γ equal to $\gamma_{\min}$, that is, to the infimum over all γ such that (C.1)–(C.5) hold. In practice, $\gamma_{\min}$ is only found to within some desired tolerance, using for instance, a bisection search over γ. Consequently, the resulting design is not truly $\mathcal{H}_\infty$ optimal.

4.3.4 Controller Characteristics

The $\mathcal{H}_2$ and $\mathcal{H}_\infty$ controllers are both model based compensators whose order equals that of the generalized plant P. Block diagrams of these controllers are shown in Figures 4-2 and 4-3 [5]. Both diagrams show that the controls u result from multiplying a control gain matrix (F_2 or F_∞) with controller generated plant state estimates. The term *model based* compensator arises because the plant states are estimated using the noisy measurements y together with feedback from a model of the plant.

In the $\mathcal{H}_2$ design, the control gain matrix F_2 is exactly the same as the gain matrix in the corresponding full state feedback Linear Quadratic Regulator (LQR) design. Similarly, the filter gain matrix L_2 exactly matches the Kalman filter gain from estimating the plant

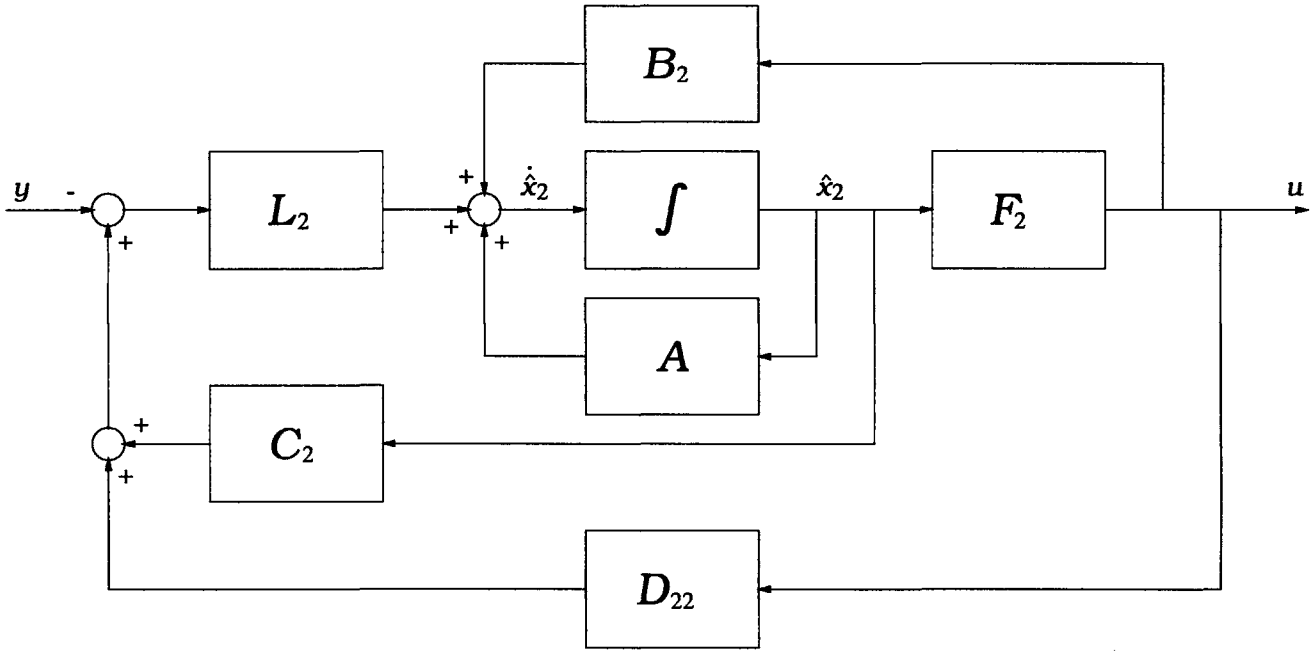

Figure 4-2: Block Diagram of K_2

states based on noisy measurements y. Consequently, the $\mathcal{H}_2$ controller exhibits a *separation property*, with the closed loop poles of $T_{zw}(s)$ equaling the union of the regulator poles, $\text{eig}[A - B_2F_2]$, and estimator poles, $\text{eig}[A - L_2C_2]$.

In contrast to the $\mathcal{H}_2$ controller, the $\mathcal{H}_\infty$ design produces a gain and filter gain matrix that are linked. This coupling of the gain matrix F_∞ and filter gain matrix $Z_\infty L_\infty$ is apparent in their respective expressions (4.19) and (4.20), as well as in condition (C.5). The coupling results because the solution for the $\mathcal{H}_\infty$ controller corresponds to finding a global minimum over all saddle points of the optimization problem

$$\inf_u \sup_w \int_0^\infty [z'(t)z(t) - \gamma^2 w'(t)w(t)]\mathrm{d}t \tag{4.25}$$

with $w(t) \in \mathcal{L}_2$. Thus, as is evident in Figure 4-3, the $\mathcal{H}_\infty$ controller must estimate the plant states in the presence of a worst case disturbance estimate $\hat{w}(t)$.

While solving for the $\mathcal{H}_\infty$ controller corresponds to finding a minimum γ for which (4.25) has a saddle point, larger values of γ also produce stabilizing controllers. In the limit as $\gamma \to \infty$, the $\mathcal{H}_\infty$ controller reduces to the $\mathcal{H}_2$ controller. Therefore, using intermediate values of γ allows one to achieve a trade off between $\mathcal{H}_2$ and $\mathcal{H}_\infty$ performance.

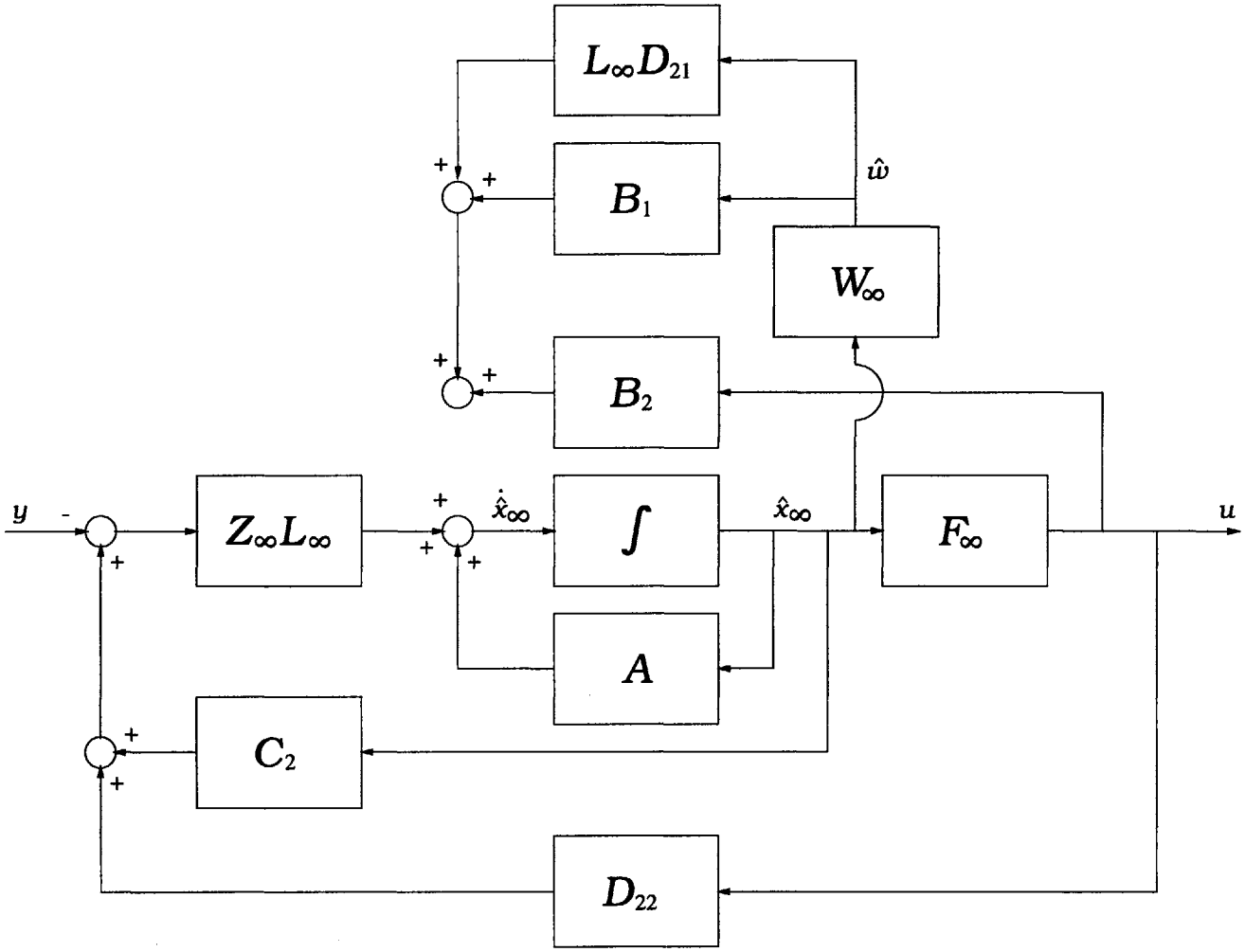

Figure 4-3: Block Diagram of K_∞

4.4 Design Weights

As mentioned previously, the TLHS will be incorporated into a generalized plant P which includes design weights on selected disturbance, control, and output variables. Using these design weights, output and control variables can be penalized differently at different frequencies, enabling a designer to take into account his knowledge of both the system's dynamics and anticipated external disturbances.

The physical plant can be augmented with design weights in any number of ways, provided the resulting generalized plant satisfies assumptions (A.1)–(A.5). Figure 4-4 [5] shows one possible augmentation, where the W_i are weighting matrices and can be functions of

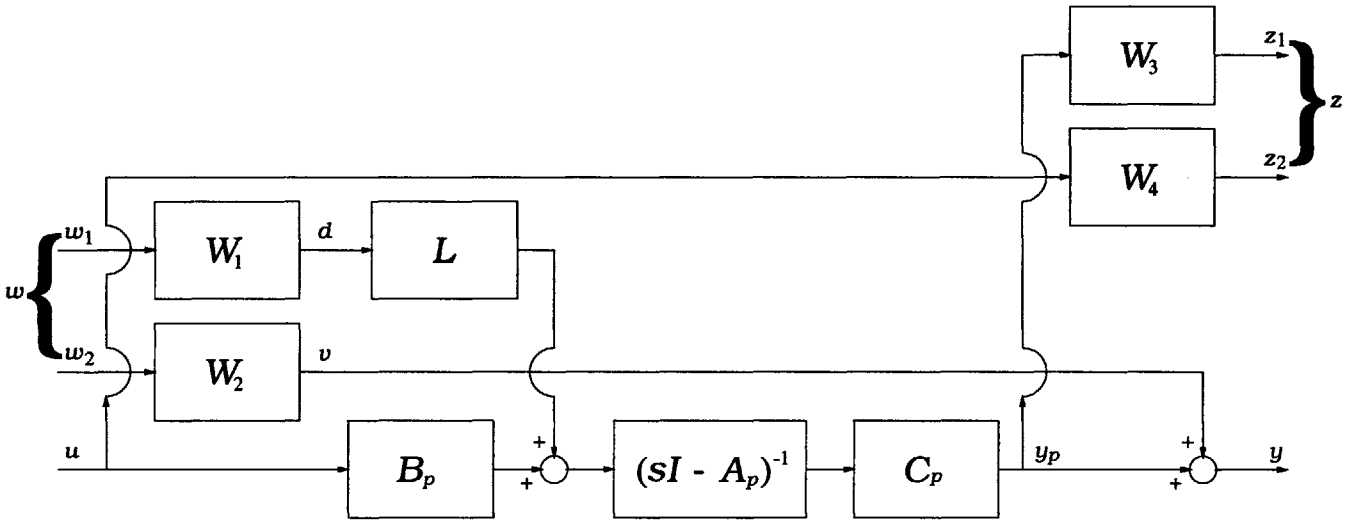

Figure 4-4: Design Weight Augmentation of Physical Plant

frequency. In this configuration, the external disturbances to the physical plant are assumed to consist of a process noise d and sensor noise v. The process noise passes through the plant's dynamics by way of the input matrix L, whereas the sensor noise is an additive disturbance at the plant output. The physical plant outputs y_p, defined by $y_p = C_p x_p$, are the quantities which are measured and fed into the controller. Weighted versions of these outputs constitute the performance variables z_1.

In selecting design weights for the augmented structure of Figure 4-4, care must be taken to ensure that the generalized plant satisfies assumptions (A.1)–(A.5). Typically when the weighting functions W_i depend on frequency, they are chosen to be of the form $W_i(s) = w_i(s)D_i$, where $w_i(s)$ is a scalar transfer function, and D_i a constant matrix, often equal to the identity. To ensure that assumptions (A.1)–(A.5) are satisfied, the transfer functions $w_i(s)$ should be chosen to be proper, stable, and minimum phase. In addition, to satisfy $V_{yy} > 0$ in (A.4), $W_2(\infty)$ must have full row rank. Similarly, $W_4(\infty)$ must have full column rank to satisfy $R_{uu} > 0$ in (A.5). These requirements on W_2 and W_4 ensure that each component of the controls u appears explicitly in z, and that each sensor noise v contains some direct feedthrough of the exogenous inputs w.

When selecting design weights, a couple of additional principles (beyond those for meeting the controller synthesis assumptions) should be kept in mind [5], [7]. First, frequency weights should conform to the nature of the physical plant's dynamics. That is to say, one

cannot manipulate frequency weights to meet unrealistic performance criteria. Control energy will have to be large over frequency ranges where the plant outputs are desired small. Similarly, one cannot expect small outputs over frequency ranges where small control energy is desired. A second principle for choosing weighting functions is to keep them as simple as possible. Using weights that are either too detailed or redundant is undesirable because the order of the $\mathcal{H}_2$ or $\mathcal{H}_\infty$ compensator equals that of the generalized plant.

4.4.1 Weights in $\mathcal{H}_2$ Design

Design weights for $\mathcal{H}_2$ synthesis should be chosen assuming that w is a zero mean, unit intensity white noise input. The $\mathcal{H}_2$ controller will then minimize the sum of the variances of the performance variables z. With this assumption on w, the weightings W_1 and W_2 should shape w_1 and w_2 so that the spectral content of d and v reflects the expected spectral content of the actual process and sensor noises affecting the physical plant [5]. W_3 and W_4 are then chosen according to the frequency ranges over which the plant outputs and controls are desired to be small. For example, at frequencies high enough for unmodeled plant dynamics to become significant, the control energy should be penalized heavily at the expense of output performance. By contrast, at lower frequencies where the spectral content of the process noise is greatest, the plant outputs should be more heavily penalized with the penalty on the controls decreased. Recall that when choosing each W_i based upon the above considerations, any redundant frequency weightings should be eliminated.

4.4.2 Weights in $\mathcal{H}_\infty$ Design

4.4.2.1 Loop Shaping

While considerations similar to those in $\mathcal{H}_2$ design can be used to select the design weights in $\mathcal{H}_\infty$ design, the properties of the $\mathcal{H}_\infty$ norm allow a designer to use design weights for direct loop shaping. With the augmentation shown in Figure 4-4, and denoting the controller $K(s)$, the closed loop transfer function from w to z is given by

$$T_{zw}(s) = \begin{bmatrix} W_3 S(s) G_1(s) W_1 & -W_3 C(s) W_2 \\ W_4 \left(I - K(s)G_2(s)\right)^{-1} K(s) G_1(s) W_1 & W_4 \left(I - K(s)G_2(s)\right)^{-1} K(s) W_2 \end{bmatrix}, \quad (4.26)$$

where

$$S(s) = (I - G_2(s)K(s))^{-1}, \qquad C(s) = -(I - G_2(s)K(s))^{-1} G_2(s)K(s), \tag{4.27}$$

$$G_1(s) = C_p (sI - A_p)^{-1} L, \qquad G_2(s) = C_p (sI - A_p)^{-1} B_p. \tag{4.28}$$

The sensitivity function $S(s)$ multiplied by $G_1(s)$ is the transfer function from d to y_p, whereas the complementary sensitivity function $C(s)$ is the transfer function from $-v$ to y_p. Assume that a designer desires these transfer functions to satisfy the requirements

$$\sigma_{\max}[S(\jmath\omega)G_1(\jmath\omega)] < \frac{1}{p_n(\omega)} \; \forall \; \omega, \tag{4.29}$$

$$\sigma_{\max}[C(\jmath\omega)] < \frac{1}{e_m(\omega)} \; \forall \; \omega, \tag{4.30}$$

where $p_n(\omega)$ and $e_m(\omega)$ are positive scalar functions of frequency. In $\mathcal{H}_\infty$ design, these requirements can be met by selecting $W_1 = w_1(s)I$, $W_2 = w_2(s)I$, and $W_3 = I$, with $|w_1(\jmath\omega)| \geq p_n(\omega)$ and $|w_2(\jmath\omega)| \geq e_m(\omega)$. With this selection, if $\|T_{zw}\|_\infty < \gamma$, Property 4.1 implies that

$$\sigma_{\max}[S(\jmath\omega)G_1(\jmath\omega)] < \frac{\gamma}{|w_1(\jmath\omega)|} \; \forall \; \omega, \tag{4.31}$$

$$\sigma_{\max}[C(\jmath\omega)] < \frac{\gamma}{|w_2(\jmath\omega)|} \; \forall \; \omega. \tag{4.32}$$

Specifications (4.29) and (4.30) are then met by adjusting W_4 until $\gamma \leq 1$. In some cases, it might also be necessary to relax $p_n(\omega)$ and $e_m(\omega)$ for a satisfactory compensator with $\gamma \leq 1$ to exist.

4.4.2.2 The Small Gain Theorem

The ability to directly shape $\sigma_{\max}[C(\jmath\omega)]$ using design weights has importance beyond that of enabling improving sensor noise rejection. Specifically, the shape of $\sigma_{\max}[C(\jmath\omega)]$ is intimately connected with a design's stability robustness. This connection is established by the Small Gain Theorem.

Multiplicative Representation of Uncertainty

Figure 4-5 shows how uncertainty may be modeled as a multiplicative perturbation

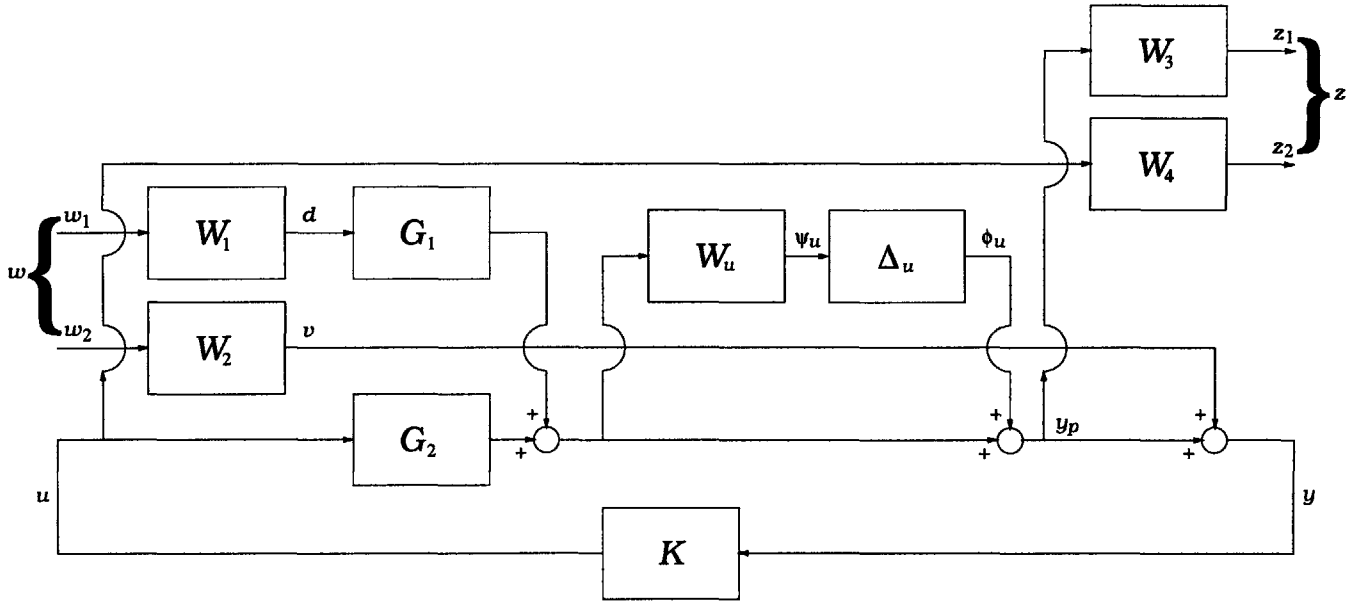

Figure 4-5: Uncertainty Represented as Multiplicative Perturbation at the Plant Output

at the plant output. In this representation, $\Delta_u(s)$ is an arbitrary, real-rational, proper, stable transfer function matrix satisfying $\|\Delta_u\|_\infty < 1$, and $W_u(s)$ is a real-rational, proper, stable transfer function matrix used to represent the assumed accuracy of the nominal plant model as a function of frequency [6]. $K(s)$ is a model based compensator, either $\mathcal{H}_2$ or $\mathcal{H}_\infty$, designed for the generalized plant in Figure 4-4. The compensator is therefore guaranteed to stabilize the nominal plant $G_2(s)$.

The multiplicative representation of uncertainty shown in Figure 4-5 defines a set of transfer function matrices, $\mathcal{G}_2$, to which the actual plant, $G_{2a}(s)$, is assumed to belong [8]. The definition of this set is

$$\mathcal{G}_2 \equiv \left\{ \tilde{G}_2(s) \mid \tilde{G}_2(s) = (I + \Delta_u(s) W_u(s))\, G_2(s),\ \|\Delta_u\|_\infty < 1 \right\}. \tag{4.33}$$

Note that although $\Delta_u(s)$ is bounded in norm, its phase and direction are arbitrary. Consequently, this representation of uncertainty is called *unstructured.* Such unstructured uncertainty can be used to account for (often high frequency) unmodeled dynamics in the nominal plant. In using the model of (4.33), the selection of an appropriate transfer function matrix $W_u(s)$ is the primary design step, as it is this matrix which determines the magnitude bound on the set $\mathcal{G}_2$.

Small Gain Theorem

Once a suitable transfer function matrix $W_u(s)$ has been selected, the schematic in

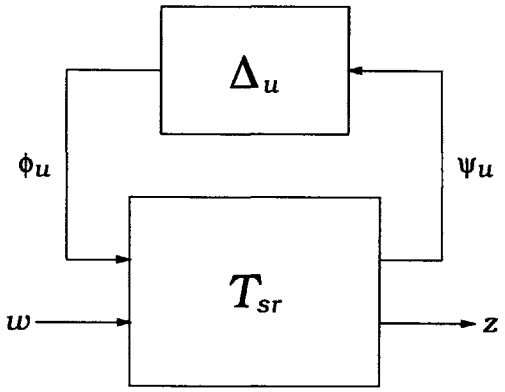

Figure 4-6: Uncertainty Model for Application of Small Gain Theorem

Figure 4-5 may be remapped into the configuration shown in Figure 4-6. In this figure,

$$T_{sr}(s) \equiv \begin{bmatrix} M(s) & T_{\psi_u w}(s) \\ T_{z\phi_u}(s) & T_{zw}(s) \end{bmatrix}. \tag{4.34}$$

$M(s)$, the transfer function from ϕ_u to ψ_u, equals $-W_u(s)C(s)$, and is stable by assumption. The perturbed transfer function from w to z is a linear fractional transformation on $T_{sr}(s)$ by $\Delta_u(s)$, denoted $F_u[T_{sr}(s), \Delta_u(s)]$ [9]. The subscript "u" on F_u indicates that the *upper* loop of $T_{sr}(s)$ is closed by $\Delta_u(s)$. For stability robustness, $F_u[T_{sr}(s), \Delta_u(s)]$ must be stable for all allowable $\Delta_u(s)$. A necessary and sufficient condition for this stability robustness is given by the Small Gain Theorem.

Theorem 4.2 (Small Gain Theorem) *Given the set of real-rational, proper, stable transfer function matrices* $\mathbf{\Delta_u} \equiv \{\Delta_u(s) \mid \|\Delta_u\|_\infty < 1\}$, $F_u[T_{sr}(s), \Delta_u(s)] = T_{zw}(s) + T_{z\phi_u}(s)\Delta_u(s)\left(I - M(s)\Delta_u(s)\right)^{-1} T_{\psi_u w}(s)$ *is stable for each* $\Delta_u(s)$ *in* $\mathbf{\Delta_u}$ *if and only if* $\|M\|_\infty \leq 1$.

Hence for stability robustness with the perturbation set $\mathbf{\Delta_u}$, $\|W_u C\|_\infty$ must be less than or equal to 1. To achieve this using direct loop shaping, one simply chooses $e_m(\omega)$ in equation (4.30) to be greater than or equal to $\sigma_{\max}[W_u(j\omega)]$ for all ω.

4.5 Summary

This chapter explains the theory of $\mathcal{H}_2$ and $\mathcal{H}_\infty$ design. The generalized plant framework is introduced, within which the goal of $\mathcal{H}_2$ and $\mathcal{H}_\infty$ control is to minimize the "size" of the plant with feedback from the controller. The norms which measure this plant's size, and which differentiate the two methodologies, are defined and interpreted. After stating the necessary assumptions on the generalized plant, synthesis methods for the two types of controllers are presented, and characteristics of each discussed. The chapter concludes with a discussion of how design weights incorporated into the generalized plant can be used to target specific performance and stability robustness requirements for the closed loop system. Within $\mathcal{H}_\infty$ design, in particular, the ability of design weights to directly shape the singular values of various transfer functions is illustrated.

Chapter 5

$\mathcal{H}_2$ and $\mathcal{H}_\infty$ Design Descriptions

5.1 Introduction

As discussed in chapter 4, the $\mathcal{H}_2$ and $\mathcal{H}_\infty$ design methodologies require that the TLHS be incorporated into the generalized plant shown in Figure 4-1. Throughout the thesis, this generalized plant is assumed to have the structure shown in Figure 4-4. This model includes design weights reflecting desired performance requirements which incorporate knowledge of anticipated external disturbances. By penalizing the control energy over frequencies where unmodeled plant dynamics are expected significant, these weights can also be used to achieve stability robustness. In $\mathcal{H}_\infty$ design, such stability robustness to unmodeled plant dynamics can be achieved in an efficient manner using direct loop shaping.

The above considerations for the generalized plant require answering a number of questions before its design can begin. In particular, (1) how shall the anticipated external disturbances on the TLHS be modeled? (2) which variables of the TLHS should be regulated, and with what specific performance requirements? and (3) what is the nature of the unmodeled dynamics in the nominal plant? The answers to these questions define the TLHS controller specifications. With these specifications established, appropriate design weights are chosen which satisfy assumptions (A.1)–(A.5), and then the corresponding $\mathcal{H}_2$ and $\mathcal{H}_\infty$ controllers are generated via the methods described in chapter 4. For each controller generated, an assessment of its performance versus the design specifications must be made. If some specifications are not met, the design weights are adjusted and a new controller generated. Thus, designing a satisfactory controller is very much an iterative procedure. In addition, the specifications themselves are subject to modification during

this process, as repeated iterations can reveal that no choice of design weights is able to meet the specifications initially put forward.

5.2 Design Specifications

The design specifications consist of constraints on TLHS variables and controls in the presence of specified external disturbances, as well as of a stability robustness requirement to unmodeled dynamics. As mentioned above, establishing the stringency of the specifications is a part of an iterative design procedure.

5.2.1 External Disturbances

The external disturbances to the TLHS are assumed to consist of a process noise $d_p(t)$ and sensor noise $d_s(t)$. Consistent with the generalized plant structure in Figure 4-4, the process noise passes through the TLHS dynamics by way of an input matrix L_d, whereas the sensor noise is an additive disturbance at the TLHS output. Each of these disturbances is modeled as the output of a shaping filter driven by zero mean, unit intensity white Gaussian noise.

The process noise $d_p(t)$ is assumed to consist of two independent horizontal wind disturbances, $d_{pm}(t)$ and $d_{ps}(t)$, with $d_{pm}(t)$ directly affecting the master helicopter and $d_{ps}(t)$ the slave helicopter [10]. Each disturbance $d_{pm}(t)$ and $d_{ps}(t)$ is the output of a first order system driven by the zero mean, unit intensity white Gaussian noise $\xi_m(t)$ or $\xi_s(t)$ respectively. Defining $d_p(t)$ and $\xi(t)$ by

$$d_p(t) \equiv \begin{bmatrix} d_{pm}(t) \\ d_{ps}(t) \end{bmatrix}, \tag{5.1}$$

$$\xi(t) \equiv \begin{bmatrix} \xi_m(t) \\ \xi_s(t) \end{bmatrix}, \tag{5.2}$$

the system generating the wind disturbances may then be written as

$$\dot{d}_p(t) = \begin{bmatrix} -0.3 & 0 \\ 0 & -0.3 \end{bmatrix} d_p(t) + 11\xi(t). \tag{5.3}$$

The wind disturbances affect the TLHS through the state equations for the helicopters'

pitch rates and horizontal velocities [4]. In particular, if the state equations are written for the variables $\dot{x}_m(t)$, $\dot{x}_s(t)$, $\dot{\theta}_m(t)$, and $\dot{\theta}_s(t)$, the coefficients multiplying $\xi_m(t)$ are the same as those multiplying $\dot{x}_m(t)$, and analogously, the coefficients multiplying $\xi_s(t)$ are the same as those multiplying $\dot{x}_s(t)$. Because the TLHS state space model derived in chapter 2 is in terms of average and difference state variables, some manipulation is required to compute the correct L_d. The resulting numerical matrix is given by

$$L_d = \begin{bmatrix} 0 & 0 \\ 0 & 0 \\ 0 & 0 \\ -0.0600 & 0.0600 \\ 2.3491 & -2.3491 \\ 0 & 0 \\ 0 & 0 \\ 0 & 0 \\ -0.0300 & 0.0300 \\ 1.1746 & 1.1746 \\ 0 & 0 \\ 0 & 0 \end{bmatrix}. \tag{5.4}$$

The sensor noise $d_s(t)$ consists of independent measurement noises at the TLHS output. The power spectral density (PSD) of each measurement noise is assumed to peak at around 27 rad/s, the first harmonic frequency of the helicopters' main rotors [2]. In addition, each noise has a pure white component, the intensity of which is proportional to the variance of the respective measured output (assuming perfect sensors). Hence, denoting the RMS of each output $y_{pi}(t)$ by r_i, the corresponding measurement noise $d_{si}(t)$ is modeled as the output of the second order shaping filter $r_i N(s)/100$, where

$$N(s) = \frac{27^2}{s^2 + 2.7s + 27^2} + 1. \tag{5.5}$$

In other words, $d_{si}(t)$ is the output of the system $r_i N(s)/100$ driven by zero mean, unit intensity white Gaussian noise.

Figure 5-1 shows the squared magnitude of $N(j\omega)$ versus frequency. The fact that each

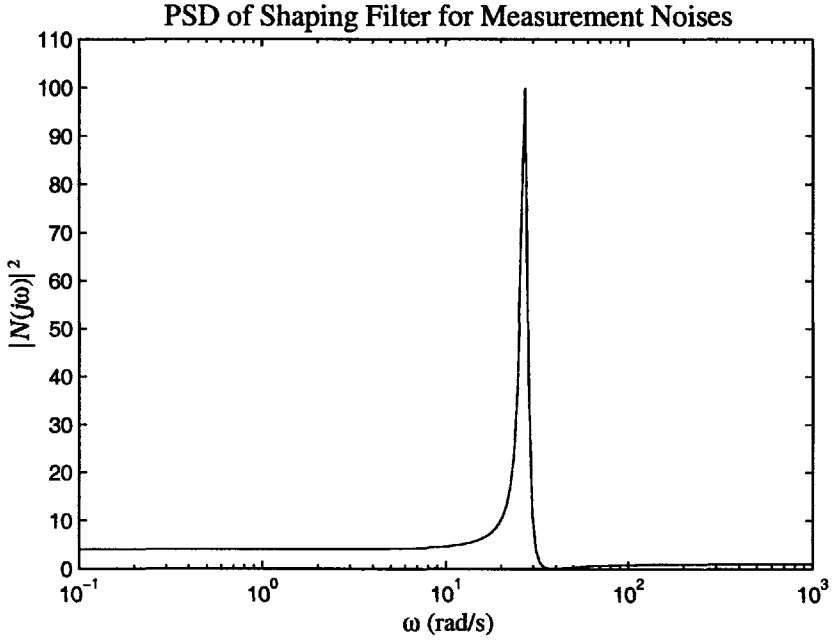

Figure 5-1: Unscaled PSD of Measurement Noises

noise $d_{si}(t)$ retains a pure white component is reflected in the fact that $|N(j\omega)|^2 \to 1$ (rather than zero) as $\omega \to \infty$. By design, the square root of the intensity of each pure white component equals 1% of the respective measured output's RMS.

5.2.2 Regulation of TLHS Variables

In establishing controller performance criteria, six variables of the TLHS are considered essential to regulate. These are

(1) Δx : horizontal separation between helicopters,

(2) $x_L - \Sigma x$: load deviation from center,

(3) θ_m : pitch angle of master helicopter,

(4) θ_s : pitch angle of slave helicopter,

(5) Δz : vertical separation between helicopters,

(6) $\Sigma \dot{x}$: average horizontal velocity of helicopters.

Regulating Δx is necessary to ensure that the helicopters remain a safe distance apart, whereas regulating $x_L - \Sigma x$ allows for control of the load motion. Both of these variables are usually commanded to zero [2]. Maintaining small pitch angles θ_m and θ_s as well as a small vertical separation Δz is necessary to ensure that the linearization of the TLHS model

put forth in chapter 2 remains valid. In other words, the TLHS is still operating within a linear region about hovering equilibrium. Lastly, regulation of the average horizontal velocity $\Sigma\dot{x}$ allows for position guidance of the TLHS.

With this set of regulated variables specified, a means is needed to test each controller's performance with respect to these variables. Such tests include evaluations in the time as well as the frequency domain. In the time domain, the response of the closed loop TLHS and controller system is examined within both a deterministic and stochastic setting.

5.2.2.1 Time Domain

Deterministic time domain simulations are used to assess the system's transient response to an initial offset (from zero) of some of the regulated variables. The following two initial conditions are chosen:

$$\text{(IC.1)}\ \ \Delta x = 1\,\text{ft},\ \ \Delta\theta = -1.359°,$$

$$\text{(IC.2)}\ \ x_L - \Sigma x = 1\,\text{ft},\ \ \Delta z = 2\,\text{ft}.$$

All of the other variables not listed explicitly in (IC.1) and (IC.2) are set equal to zero. Note that (IC.1) results from applying a steady state differential cyclic of $-0.2194°$, whereas (IC.2) results from applying a steady state differential collective of $0.1345°$ together with a steady state average cyclic of $0°$ [2]. Hence, these two initial conditions test the closed loop response of the SM and ASM plant respectively. Because the $\mathcal{H}_2$ and $\mathcal{H}_\infty$ controllers are designed assuming a process noise of horizontal wind disturbances, which do not affect the AVM plant ($L = L_d$ in Figure 4-4), the response of the AVM plant will be unaffected by control. Thus the transient response of $\Sigma\dot{z}$ remains an exponential decay with the time constant $\tau = 4.25$ s, as shown in Figure 3-4.

The stochastic simulations involve applying process and sensor noise to the zero state closed loop system and then observing the response of the TLHS variables. The process noise is generated via (5.3) and the sensor noise via the appropriately scaled filter in (5.5). The scaling factors r_i used to generate the measurement noises are determined from an initial simulation in which sensor noise is omitted.

In both the deterministic and stochastic simulations, the following magnitude constraints on the TLHS variables are considered desirable:

$$\text{(S.1)}\ \ |\Delta x| \leq 6\,\text{ft},$$

(S.2) $|x_L - \Sigma x| \leq 6$ ft,

(S.3) $|\theta_m|,\ |\theta_s| \leq 10°$,

(S.4) $|\Delta z| \leq 10$ ft,

(S.5) $|\Sigma \dot{x}| \leq 15$ ft/s.

Of these specifications, (S.1)–(S.3) are considered mandatory for all acceptable designs, whereas trade offs are allowed between satisfying (S.4) and (S.5). The speed with which the TLHS variables are driven to zero in the transient simulations will also be compared and contrasted among the different controllers, with quicker responses being more desirable.

5.2.2.2 Frequency Domain

The frequency domain specifications reflect the desire to minimize the effect of the process and sensor noise on the regulated variables. Recall from equation (5.3), that the process noise $d_p(t)$ is modeled as the output of a low pass filter driven by white noise. Denoting the transfer function from $d_p(t)$ to $y(t)$ by $T_{y,d_p}(s)$, and converting all magnitudes to decibels, the frequency domain specifications for process noise rejection are

(S.6) $\sigma_{\max}[T_{\Delta x,d_p}(j\omega)] \leq -20$ dB for $\omega \leq 0.3$ rad/s,

(S.7) $\sigma_{\max}[T_{x_L-\Sigma x,d_p}(j\omega)] \leq -20$ dB for $\omega \leq 0.3$ rad/s,

(S.8) $\sigma_{\max}[T_{\theta_m,d_p}(j\omega)],\ \sigma_{\max}[T_{\theta_s,d_p}(j\omega)] \leq -10$ dB for $\omega \leq 0.3$ rad/s,

(S.9) $\sigma_{\max}[T_{\Delta z,d_p}(j\omega)] \leq -10$ dB for $\omega \leq 0.3$ rad/s,

(S.10) $\sigma_{\max}[T_{\Sigma \dot{x},d_p}(j\omega)] \leq -5$ dB for $\omega \leq 0.3$ rad/s.

Similar to the time domain specifications, (S.6)–(S.8) are considered mandatory for all acceptable designs, whereas (S.9) and (S.10) are only desirable and hence trade offs between the two are permitted.

From the earlier discussion in section 5.2.1, and also from Figure 5-1, the PSD of the sensor noise $d_s(t)$ is assumed to peak at around 27 rad/s, the first harmonic frequency of the helicopters' main rotors. Hence for sensor noise rejection, the frequency domain specification is

(S.11) $\sigma_{\max}[C(j\omega)] \leq -20$ dB for $\omega \approx 27$ rad/s,

where the complementary sensitivity function $C(s)$, defined in (4.27)–(4.28), is the closed loop transfer function from $-d_s(t)$ to the TLHS outputs $y_p(t)$. Specification (S.11) is considered mandatory for all acceptable designs.

5.2.3 Regulation of TLHS Controls

Recall that the longitudinal motion of the TLHS is governed by the four independent helicopter controls

(1) Θ_{cm} : master collective control,

(2) Θ_{cs} : slave collective control,

(3) B_{lcm} : master cyclic control,

(4) B_{lcs} : slave cyclic control.

All of the control variables must be regulated to ensure that the TLHS model linearization of chapter 2 remains valid. Control variable responses are evaluated in the time as well as the frequency domain, closely following those tests used for the TLHS regulated variables. Time domain simulations are performed in both a deterministic and stochastic setting.

5.2.3.1 Time Domain

The deterministic time domain simulations examine the control variables' transient responses to those same initial conditions, (IC.1) and (IC.2), used in evaluating the TLHS regulated variables. Again, these two initial conditions test the closed loop response of the SM and ASM plant respectively. As described earlier, the AVM plant will remain unaffected by control. As a consequence, the response of the average collective control ($\Sigma\Theta_c$) will always be identically equal to zero, or in other words, Θ_{cm} will always exactly equal $-\Theta_{cs}$. The stochastic simulations used to evaluate control variable responses are also identical to those used in testing the TLHS regulated variables. In both the deterministic and stochastic simulations, the control variables must satisfy the magnitude restraints

(S.12) $|\Theta_{cm}|,\ |\Theta_{cs}| < 10°,$

(S.13) $|B_{lcm}|,\ |B_{lcs}| < 15°.$

Specifications (S.12) and (S.13) are considered mandatory for all acceptable designs. Each of these specifications is also consistent with assumption (2.5) made during the TLHS model linearization.

5.2.3.2 Frequency Domain

The frequency domain specifications reflect the desire to minimize the effect of the process noise on the control variables. Hence following the same reasoning used in establishing specifications for the TLHS variables, the frequency domain specifications for the control variables are

$$\text{(S.14)}\quad \sigma_{\max}[T_{\Theta_{cm},d_p}(j\omega)],\ \sigma_{\max}[T_{\Theta_{cs},d_p}(j\omega)] \leq -10\,\text{dB for } \omega \leq 0.3\,\text{rad/s},$$

$$\text{(S.15)}\quad \sigma_{\max}[T_{B_{lcm},d_p}(j\omega)],\ \sigma_{\max}[T_{B_{lcs},d_p}(j\omega)] \leq -6\,\text{dB for } \omega \leq 0.3\,\text{rad/s}.$$

Specifications (S.14) and (S.15) are considered mandatory for all acceptable designs.

5.2.4 Unmodeled Dynamics

The unmodeled dynamics of the TLHS are assumed to consist of a time delay of up to 0.05 s. Hence, the actual TLHS plant is assumed to belong to the set $\mathcal{G}_2$, which is defined as

$$\mathcal{G}_2 \equiv \left\{\tilde{G}_2(s) \mid \tilde{G}_2(s) = G_2(s)e^{-\tau s},\ 0 \leq \tau \leq 0.05\right\}, \tag{5.6}$$

where $G_2(s)$ is the nominal TLHS transfer function matrix defined in (4.28). To apply the Small Gain Theorem, the unmodeled time delay is represented as a multiplicative perturbation at the nominal plant output. Hence, $\mathcal{G}_2$ is rewritten in the form

$$\mathcal{G}_2 \equiv \left\{\tilde{G}_2(s) \mid \tilde{G}_2(s) = (I + \Delta_u(s)W_u(s))\,G_2(s),\ \|\Delta_u\|_\infty < 1\right\}, \tag{5.7}$$

for some real-rational, proper, stable transfer function matrix $W_u(s)$ still to be determined. In order for the set in (5.7) to include that defined in (5.6), it must be true that for all τ, $0 \leq \tau \leq 0.05$, there exists a proper, stable transfer function matrix $\Delta_u(s)$, $\|\Delta_u\|_\infty < 1$, such that

$$G_2(s)e^{-\tau s} = (I + \Delta_u(s)W_u(s))\,G_2(s). \tag{5.8}$$

Assuming that $G_2(s)$ is non-singular along the $j\omega$-axis and allowing $W_u(s)$ to assume the form $w_u(s)I$, with $w_u(s)$ a scalar transfer function, (5.8) then implies that

$$|e^{-j\omega\tau} - 1| \leq |w_u(j\omega)|\ \forall\ \omega,\ 0 \leq \tau \leq 0.05 \qquad \Longrightarrow \tag{5.9}$$

$$\max_{0 \leq \tau \leq 0.05} |e^{-j\omega\tau} - 1| \leq |w_u(j\omega)| \; \forall \; \omega. \tag{5.10}$$

A simple, proper, stable transfer function $w_u(s)$ satisfying (5.10) is given by [5]

$$w_u(s) = \frac{0.21s}{0.05s + 4}. \tag{5.11}$$

Figure 5-2 shows $|w_u(j\omega)|$ and $|e^{-j\omega\tau} - 1|$ plotted together (in decibels) for $\tau = 0.05$, which

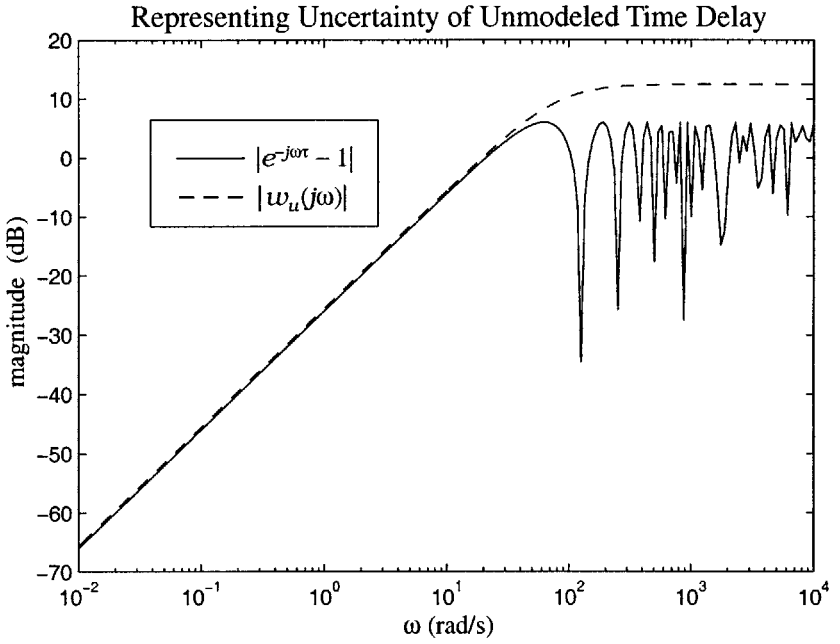

Figure 5-2: Magnitude of $w_u(j\omega)$ and Time Delay Uncertainty

is the worst case value.

The scalar transfer function $w_u(s)$ defined in (5.11), when multiplied by the identity matrix, defines via (5.7) the uncertainty set to which the actual TLHS plant belongs, and over which every controller must achieve stability. The necessary and sufficient condition for this stability robustness is given by the Small Gain Theorem. From this theorem, the stability of the closed loop system over the entire set $\mathcal{G}_2$ is guaranteed if and only if $\|M\|_\infty \leq 1$, where $M(s) = -W_u(s)C(s)$. For the transfer function matrix $W_u(s) = w_u(s)I$, this is equivalent to the condition

$$|w_u(j\omega)|\sigma_{\max}[C(j\omega)] \leq 1 \; \forall \; \omega. \tag{5.12}$$

Hence, the final design specification, intended to achieve stability robustness to a time delay

of up to 0.05 s, requires that the complementary sensitivity transfer function matrix $C(s)$ satisfy

$$\text{(S.16)}\quad \sigma_{\max}[C(j\omega)] \leq \frac{1}{|w_u(j\omega)|} \;\forall\, \omega,$$

where $w_u(s)$ is as defined in (5.11). Specification (S.16) is considered mandatory for all acceptable designs.

5.3 Design Descriptions

A controller design is completely specified by how the generalized plant in (4.11) and (4.12) is defined. This is done by specifying the matrices C_p and L, together with the weighting matrices W_i, for the generalized plant structure in Figure 4-4. In both the $\mathcal{H}_2$ and $\mathcal{H}_\infty$ case, two designs are ultimately arrived at which satisfy the previously put forward design specifications. In all of the designs, the matrix L in Figure 4-4 is set equal to the matrix L_d in (5.4). All final controllers result only after a long series of design iterations.

5.3.1 Output Matrix

The output matrix C_p determines which linear combinations of the TLHS states are penalized in the controller designs' cost functionals. It is weighted versions of these outputs that the controller tries to minimize. As discussed in chapter 3, while it may be desirable to penalize all of those TLHS variables in need of regulation, doing so necessitates performance trade offs amongst them. Additionally, increasing the number of outputs increases the order of the controller when the weighting matrices depend on frequency.

Among the six variables specified in section 5.2.2 as essential to regulate, various combinations of them are tested repeatedly as outputs to determine which groupings produce controllers best satisfying the design specifications. During these trials, it becomes apparent that all acceptable designs *must* include among their outputs the horizontal separation between the helicopters (Δx), the load deviation from center ($x_L - \Sigma x$), and some combination of the master and slave pitch angles (θ_m, θ_s). Denoting the final two $\mathcal{H}_2$ designs as $\mathcal{A}_2$ and $\mathcal{B}_2$, and the final two $\mathcal{H}_\infty$ designs as $\mathcal{C}_\infty$ and $\mathcal{D}_\infty$, the outputs chosen are listed in

Designs	Outputs
$\mathcal{A}_2$, $\mathcal{C}_\infty$	Δx, $x_L - \Sigma x$, $\Sigma\theta$
$\mathcal{B}_2$, $\mathcal{D}_\infty$	Δx, $x_L - \Sigma x$, $\Sigma\theta$,$\Sigma\dot{x}$

Table 5.1: TLHS Outputs for Controller Designs

Table 5.1. For designs $\mathcal{A}_2$ and $\mathcal{C}_\infty$, this gives the output matrix C_p as

$$C_p = \begin{bmatrix} 0 & 1 & 0 & 0 & 0 & 0 & 0 & 0 & 0 & 0 & 0 & 0 \\ 0 & 0 & 0 & 0 & 0 & 0.2941 & 0.5 & 1 & 0 & 0 & 0 & 0 \\ 0 & 0 & 0 & 0 & 0 & 1 & 0 & 0 & 0 & 0 & 0 & 0 \end{bmatrix}. \tag{5.13}$$

For designs $\mathcal{B}_2$ and $\mathcal{D}_\infty$, the output matrix C_p simply contains one additional row to incorporate $\Sigma\dot{x}$. Hence for these designs,

$$C_p = \begin{bmatrix} 0 & 1 & 0 & 0 & 0 & 0 & 0 & 0 & 0 & 0 & 0 & 0 \\ 0 & 0 & 0 & 0 & 0 & 0.2941 & 0.5 & 1 & 0 & 0 & 0 & 0 \\ 0 & 0 & 0 & 0 & 0 & 1 & 0 & 0 & 0 & 0 & 0 & 0 \\ 0 & 0 & 0 & 0 & 0 & 0 & 0 & 0 & 1 & 0 & 0 & 0 \end{bmatrix}. \tag{5.14}$$

5.3.2 Weighting Matrices

The weighting matrices W_i of the augmented plant structure are chosen taking into account the anticipated external disturbances to the plant along with the design specifications for both performance and stability robustness. Some of these matrices are functions of frequency, but for simplicity, redundant weighting functions are avoided. The weighting functions are also chosen to ensure that assumptions (A.1)–(A.5) from section 4.3.1 are met.

5.3.2.1 $\mathcal{H}_2$ Designs

Recall that for $\mathcal{H}_2$ synthesis, the weightings W_1 and W_2 reflect the expected spectral content of the process noise d and sensor noise v in Figure 4-4. The expected external disturbances $d_p(t)$ and $d_s(t)$ to the TLHS are each described in section 5.2.1. Specifically, from equation (5.3), the process noise $d_p(t)$ is the output of the shaping filter $L(s)I$, where

$$L(s) = \frac{11}{s + 0.3}. \tag{5.15}$$

Similarly, each sensor noise $d_{si}(t)$ is the output of a scaled version of the shaping filter $N(s)$, as defined in (5.5). Hence in the initial design stages, W_1 is set equal to $w_1(s)I$ and W_2 to $w_2(s)I$, with $w_1(s) = L(s)$ and $w_2(s) = N(s)$. The final frequency weightings then evolve during a series of design iterations aimed at meeting the design specifications. The weighting functions ultimately chosen are listed in Table 5.2.

Design	$w_1(s)$	$w_2(s)$
$\mathcal{A}_2$	$\frac{132}{s+0.9}$	$\frac{3(s^2+7s+2\cdot 27^2)}{s^2+7s+27^2}$
$\mathcal{B}_2$	$\frac{132}{s+0.9}$	$\frac{3(s^2+10s+2\cdot 27^2)}{s^2+10s+27^2}$

Table 5.2: Weighting Functions $w_1(s)$ and $w_2(s)$ for $\mathcal{H}_2$ Controller Designs

The weighting matrices W_3 and W_4 are selected according to the frequency ranges over which the plant outputs and controls are desired to be small. However, the frequency dependent nature of the specifications for process noise rejection below 0.3 rad/s and sensor noise rejection around 27 rad/s has already been incorporated into the weightings W_1 and W_2. Hence, the matrices W_3 and W_4 are chosen to meet the specifications' magnitude requirements, as well as to satisfy requirement (S.16) for stability robustness.

The weighting matrix W_3 is selected as a square diagonal matrix, independent of frequency, with each diagonal element W_{3i} corresponding to the penalty placed on the i-th TLHS output. During the design iterations, the elements of W_3 are adjusted in order to meet the design specifications. The weighting matrix W_4 is designed to achieve stability robustness to the time delay of up to 0.05 s. Hence this matrix is frequency dependent, with $\sigma_{\max}[W_4(\jmath\omega)]$ largest over frequencies where the time delay dynamics are most significant. Choosing W_4 to have the form $w_4(s)D_4$, with $w_4(s)$ a scalar transfer function and D_4 a constant square matrix, the weighting function $w_4(s)$ should resemble the function $w_u(s)$, defined in (5.11), used to capture the unmodeled dynamics of the time delay. In fact, the function $w_4(s)$ ultimately selected for each $\mathcal{H}_2$ design is nearly identical to $w_u(s)$, with only the slight modification of a low frequency zero added to $w_4(s)$ to make this function minimum phase. The matrix D_4 is then chosen by first writing it as the product of two more meaningful matrices, S and R. The matrix R is used to transform the set of average and difference control variables back into the set of individual helicopter controls. Defining R

as

$$R = \begin{bmatrix} 1 & 0 & \frac{1}{2} & 0 \\ 1 & 0 & -\frac{1}{2} & 0 \\ 0 & \frac{1}{2} & 0 & 1 \\ 0 & -\frac{1}{2} & 0 & 1 \end{bmatrix} \tag{5.16}$$

gives the result

$$Ru = R \begin{bmatrix} \Sigma\Theta_c \\ \Delta B_{lc} \\ \Delta\Theta_c \\ \Sigma B_{lc} \end{bmatrix} = \begin{bmatrix} \Theta_{cm} \\ \Theta_{cs} \\ B_{lcm} \\ B_{lcs} \end{bmatrix}. \tag{5.17}$$

S is then chosen to be a constant diagonal matrix, enabling each diagonal element to independently penalize a single master or slave helicopter control. Table 5.3 gives the

Design	$w_4(s)$	S	$D_4 = SR$
$\mathcal{A}_2$	$\frac{0.21(s+0.001)}{0.05s+4}$	$10^3 \cdot \begin{bmatrix} 2.1646 & 0 & 0 & 0 \\ 0 & 2.1646 & 0 & 0 \\ 0 & 0 & 1.3321 & 0 \\ 0 & 0 & 0 & 1.3321 \end{bmatrix}$	$10^3 \cdot \begin{bmatrix} 2.1646 & 0 & 1.0823 & 0 \\ 2.1646 & 0 & -1.0823 & 0 \\ 0 & 0.6660 & 0 & 1.3321 \\ 0 & -0.6660 & 0 & 1.3321 \end{bmatrix}$
$\mathcal{B}_2$	$\frac{0.21(s+0.1)}{0.05s+4}$	$10^3 \cdot \begin{bmatrix} 2.1646 & 0 & 0 & 0 \\ 0 & 2.1646 & 0 & 0 \\ 0 & 0 & 1.1545 & 0 \\ 0 & 0 & 0 & 1.1545 \end{bmatrix}$	$10^3 \cdot \begin{bmatrix} 2.1646 & 0 & 1.0823 & 0 \\ 2.1646 & 0 & -1.0823 & 0 \\ 0 & 0.5772 & 0 & 1.1545 \\ 0 & -0.5772 & 0 & 1.1545 \end{bmatrix}$

Table 5.3: Components of Weighting Function W_4 for $\mathcal{H}_2$ Controller Designs

weighting function $w_4(s)$ and the matrices S and D_4 for each of the final $\mathcal{H}_2$ designs. The resulting weighting function W_4, together with the weighting matrix W_3, are then listed in Table 5.4.

5.3.2.2 $\mathcal{H}_\infty$ Designs

For $\mathcal{H}_\infty$ synthesis, the weighting matrices are designed to meet some of the frequency domain design specifications using direct loop shaping. Loop shaping, however, rarely produces the desired controller on the first try. First, the direct shaping of transfer functions requires producing an $\mathcal{H}_\infty$ controller with the parameter γ less than or equal to 1. However, if the specifications to be met by loop shaping are too stringent or do not comply with

Design	W_3	$W_4 = w_4(s)D_4$
$\mathcal{A}_2$	$10^5 \cdot \begin{bmatrix} 1 & 0 & 0 \\ 0 & 0.25 & 0 \\ 0 & 0 & 3.3333 \end{bmatrix}$	$\frac{0.21(s+0.001)}{0.05s+4} \cdot 10^3 \cdot \begin{bmatrix} 2.1646 & 0 & 1.0823 & 0 \\ 2.1646 & 0 & -1.0823 & 0 \\ 0 & 0.6660 & 0 & 1.3321 \\ 0 & -0.6660 & 0 & 1.3321 \end{bmatrix}$
$\mathcal{B}_2$	$10^4 \cdot \begin{bmatrix} 6.6667 & 0 & 0 & 0 \\ 0 & 4 & 0 & 0 \\ 0 & 0 & 2.5 & 0 \\ 0 & 0 & 0 & 2 \end{bmatrix}$	$\frac{0.21(s+0.1)}{0.05s+4} \cdot 10^3 \cdot \begin{bmatrix} 2.1646 & 0 & 1.0823 & 0 \\ 2.1646 & 0 & -1.0823 & 0 \\ 0 & 0.5772 & 0 & 1.1545 \\ 0 & -0.5772 & 0 & 1.1545 \end{bmatrix}$

Table 5.4: Weighting Functions W_3 and W_4 for $\mathcal{H}_2$ Controller Designs

the plant's dynamics, this parameter will be too large. Second, even if the requirement $\gamma \leq 1$ is achieved, those specifications not explicitly targeted with the loop shaping may not be satisfied. Hence, selecting a satisfactory set of weighting matrices involves numerous design iterations in which both the weighting functions and the performance criteria are subject to change. Furthermore, while the sections below describe the selection of each weighting matrix separately, these selections are actually highly interdependent and occur simultaneously throughout the design process.

The matrix W_1 is used to meet frequency domain specifications on those TLHS variables which are included among the TLHS outputs. The transfer function from the process noise to these outputs equals $S(s)G_1(s)$, where the matrices in this product are as defined in section 4.4.2.1 on loop shaping. The weighting function W_1 is selected to have the form $w_1(s)I$, while W_3 is chosen as a constant diagonal matrix with diagonal elements W_{3i}. To then shape the transfer function $S(s)G_1(s)$ to meet specifications (S.6), (S.7), and (S.10), one first rewrites these specifications in the form

$$\sigma_{\max}[T_{x_i,d_p}(\jmath\omega)] \leq \frac{1}{W_{3i}\, p_n(\omega)} \;\forall\; \omega, \tag{5.18}$$

where x_i is the i-th TLHS output, and $p_n(\omega)$ is defined by

$$p_n(\omega) = \frac{7}{|\jmath\omega + 0.6|}. \tag{5.19}$$

Figure 5-3 shows the function $1/p_n(\omega)$ versus frequency. The plot reveals that if W_{31} and W_{32} are each greater than or equal to 1, then both (S.6) and (S.7) are guaranteed to be

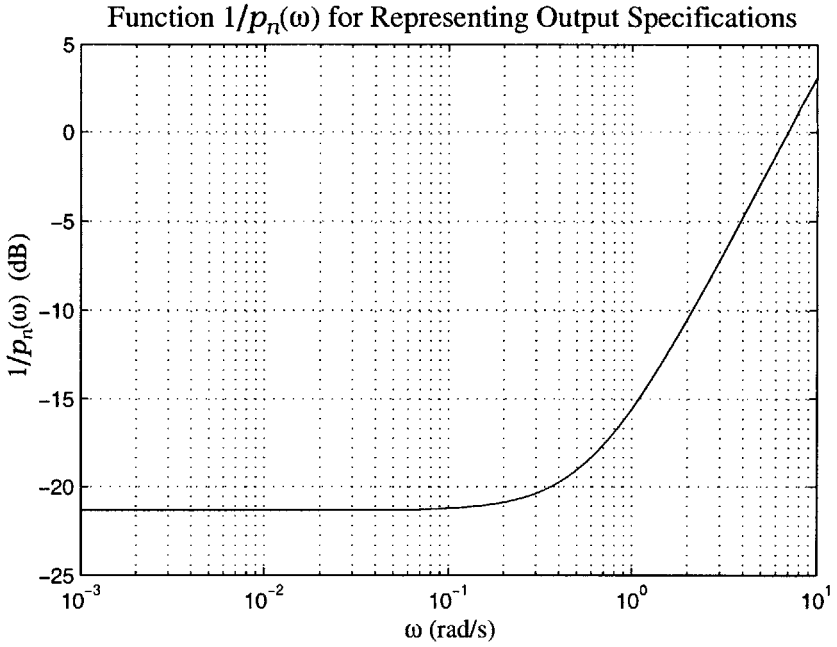

Figure 5-3: Function Used to Represent Frequency Domain Output Specifications

satisfied by choosing $|w_1(j\omega)| \geq p_n(\omega)$. Similarly, for design $\mathcal{D}_\infty$, where $\Sigma\dot{x}$ is the fourth TLHS output, specification (S.10) is guaranteed to be satisfied by choosing $|w_1(j\omega)| \geq p_n(\omega)$, as long as $W_{34} \geq 0.1778$. Hence for both $\mathcal{H}_\infty$ designs, subject to the above conditions on W_3, $w_1(s)$ is selected as the function $7/(s+0.6)$, such that $|w_1(j\omega)|$ exactly equals $p_n(\omega)$ for all frequencies.

The weighting matrix W_2 is used to meet the frequency domain specifications for sensor noise rejection, (S.11), and for stability robustness to the time delay of up to 0.05 s, (S.16). Both of these specifications are on the complementary sensitivity function $C(s)$, as defined in section 4.4.2.1. Similar to the weighting matrix W_1, the matrix W_2 is chosen to have the form $w_2(s)I$, with $w_2(s)$ a scalar transfer function. The matrix W_3, however, is assumed to equal the identity. To then shape $C(s)$, specifications (S.11) and (S.16) are first each rewritten in the form

$$\sigma_{\max}[C(j\omega)] \leq \frac{1}{e_{mi}(\omega)} \; \forall \; \omega, \tag{5.20}$$

with $i = 1$ for (S.11) and $i = 2$ for (S.16). Specification (S.16) is easily written in the form of (5.20) simply by letting $e_{m2}(\omega) = |w_u(j\omega)|$, where $w_u(s)$, defined in (5.11), is the transfer function used to capture the unmodeled dynamics of the time delay. Then (5.20) exactly matches the original statement of (S.16). Specification (S.11) is written in the form

of (5.20) by defining $e_{m1}(\omega)$ as

$$e_{m1}(\omega) = \frac{|(\jmath\omega)^2 + 2.7\jmath\omega + 2{\cdot}27^2|}{|(\jmath\omega)^2 + 2.7\jmath\omega + 27^2|}. \tag{5.21}$$

This function precisely equals $|N(\jmath\omega)|$, where $N(s)$ is the sensor noise shaping filter defined in (5.5).

Ultimately, it is desirable to combine the two specifications (S.11) and (S.16) into a single specification with the form

$$\sigma_{\max}[C(\jmath\omega)] \leq \frac{1}{e_m(\omega)} \ \forall\ \omega. \tag{5.22}$$

A natural starting point is to let $e_m(\omega) = e_{m1}(\omega)e_{m2}(\omega)$, where the functions in this product are as defined above. With $e_m(\omega)$ so specified, Figure 5-4 illustrates how the specifi-

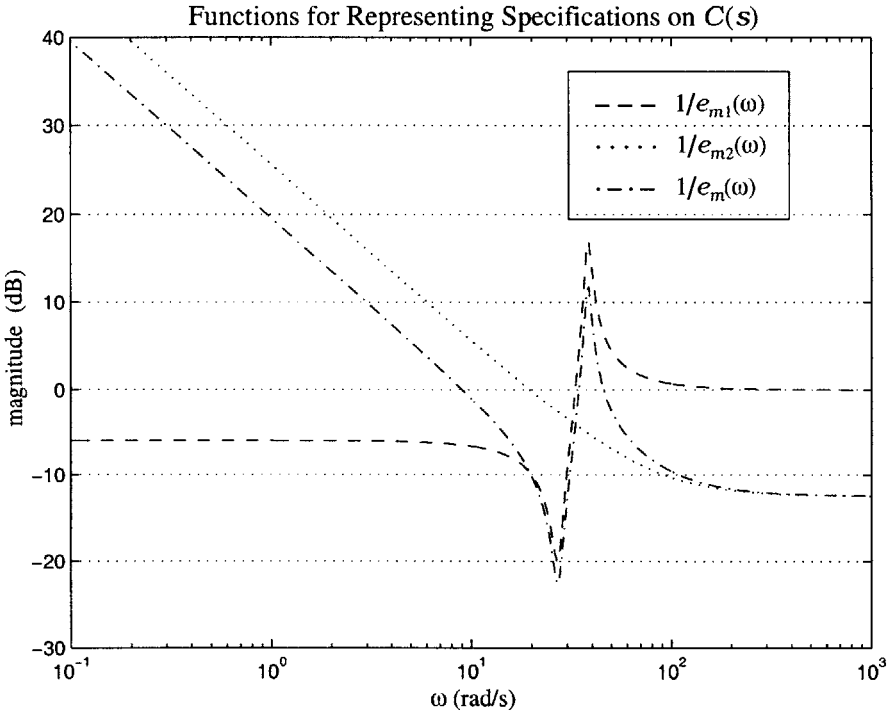

Figure 5-4: Functions Used to Represent Frequency Domain Specifications on $C(s)$

cation (5.22) attempts to combine into one the two separate specifications for sensor noise rejection and stability robustness. The plot reveals that by choosing $|w_2(\jmath\omega)| \geq e_m(\omega)$, (S.16) is guaranteed to be satisfied, and (S.11) is guaranteed to be satisfied for all frequencies except those in the approximate range from 30 to 100 rad/s. Hence in the initial design

stages, $w_2(s)$ is set equal to the product $w_{21}(s)w_{22}(s)$, where

$$w_{21}(s) = \frac{s^2 + 2.7s + 2{\cdot}27^2}{s^2 + 2.7s + 27^2} \tag{5.23}$$

and

$$w_{22}(s) = \frac{0.21(s + 0.1)}{0.05s + 4}. \tag{5.24}$$

In other words, $w_{21}(s) = N(s)$, and $w_{22}(s)$ is nearly identical to $w_u(s)$, with only the slight modification of a low frequency zero added to $w_{22}(s)$ to make this function minimum phase. Since this selection gives $|w_{21}(\jmath\omega)| = e_{m1}(\omega)$ and $|w_{22}(\jmath\omega)| \geq e_{m2}(\omega)$ for all frequencies, it follows that

$$|w_2(\jmath\omega)| \geq e_{m1}(\omega)e_{m2}(\omega) = e_m(\omega) \ \forall \ \omega. \tag{5.25}$$

The final frequency weighting function $w_2(s)$ evolves during a series of design iterations aimed at meeting both (S.11) and (S.16) over all frequencies. In each of the final designs, $w_{22}(s)$ remains unchanged from that in (5.24), whereas $w_{21}(s)$ is relaxed in an effort to reduce the overshoot at frequencies around 40 rad/s. In design $\mathcal{C}_\infty$, a scaling factor is also introduced. The weighting function $w_2(s)$ ultimately chosen for each design is listed in Table 5.5.

Design	$w_2(s)$
$\mathcal{C}_\infty$	$\frac{1.3(s^2+7s+2{\cdot}27^2)}{s^2+7s+27^2} \cdot \frac{0.21(s+0.1)}{0.05s+4}$
$\mathcal{D}_\infty$	$\frac{(s^2+7s+2{\cdot}27^2)}{s^2+7s+27^2} \cdot \frac{0.21(s+0.1)}{0.05s+4}$

Table 5.5: Weighting Function $w_2(s)$ for $\mathcal{H}_\infty$ Controller Designs

The weighting functions W_3 and W_4 are both selected as constant matrices and are used primarily for fine tuning the responses of individual TLHS variables and controls. As mentioned previously, W_3 is a constant diagonal matrix such that each diagonal element W_{3i} corresponds to the penalty placed on the i-th TLHS output. In order to conform with assumptions made when selecting $w_1(s)$ and $w_2(s)$ for loop shaping, the matrix W_3 is initially set equal to the identity. However, as the iterations involving all four weighting functions proceed, the elements W_{3i} are adjusted to focus control on those outputs in need of greater regulation, and in so doing achieve an appropriate penalty balance for the meeting

of all of the design specifications. In both $\mathcal{H}_\infty$ designs, the final values of W_{31} and W_{32} are equal to or just slightly greater than 1, hence agreeing closely with the assumptions made on W_3 during loop shaping. W_{33}, the penalty on $\Sigma\theta$, is chosen based upon empirical evaluations of controller performance, and the values chosen for each of the two designs differ significantly. In particular, $\Sigma\theta$ incurs a larger penalty in design $\mathcal{C}_\infty$, in which there are only three outputs, than in design $\mathcal{D}_\infty$, in which a fourth output $\Sigma\dot{x}$ is also penalized. In design $\mathcal{D}_\infty$, the fourth penalty W_{34} is chosen as 0.1667, very near the value of 0.1778 shown earlier to guarantee the meeting of specification (S.10). Analogous to the weighting function W_3, the matrix W_4 is used to appropriately balance individual control penalties in order to meet all of the design specifications. In addition, because no assumptions are made on W_4 during loop shaping, the varying of this matrix is instrumental in producing a controller such that the parameter γ is less than or equal to 1. Similar to the $\mathcal{H}_2$ design procedure, the matrix W_4 in the $\mathcal{H}_\infty$ case is chosen by first writing it as the product of two more meaningful matrices, S and R. The matrix R, defined in (5.16), transforms the set of average and difference control variables back into the set of individual helicopter controls, whereas S, a constant diagonal matrix, is used to independently penalize each of these individual controls. The matrices W_3, S, and W_4 ultimately chosen for each $\mathcal{H}_\infty$ design are listed in Table 5.6.

5.4 Summary

This chapter describes the generalized plant designs for $\mathcal{H}_2$ and $\mathcal{H}_\infty$ controller synthesis. To motivate these designs, performance and stability robustness specifications are established. The performance specifications are based upon assumed process and sensor noises for which the spectral contents and means of entering the TLHS dynamics are known. The stability robustness specification assumes the presence of an unmodeled time delay of up to 0.05 s. Based upon the established specifications, four generalized plants, two for $\mathcal{H}_2$ and two for $\mathcal{H}_\infty$ synthesis, are designed. The selection of design parameters and weighting functions for these plants is explained with respect to achieving the performance and stability robustness objectives, with the strategy for choosing the weighting functions also depending on the intended method of synthesis.

Design	W_3	S	$W_4 = SR$
$\mathcal{C}_\infty$	$\begin{bmatrix} 1 & 0 & 0 \\ 0 & 1.0526 & 0 \\ 0 & 0 & 1.25 \end{bmatrix}$	$10^{-2}\cdot\begin{bmatrix} 4.8412 & 0 & 0 & 0 \\ 0 & 4.8412 & 0 & 0 \\ 0 & 0 & 3.2275 & 0 \\ 0 & 0 & 0 & 3.2275 \end{bmatrix}$	$10^{-2}\cdot\begin{bmatrix} 4.8412 & 0 & 2.4206 & 0 \\ 4.8412 & 0 & -2.4206 & 0 \\ 0 & 1.6137 & 0 & 3.2275 \\ 0 & -1.6137 & 0 & 3.2275 \end{bmatrix}$
$\mathcal{D}_\infty$	$\begin{bmatrix} 1 & 0 & 0 & 0 \\ 0 & 1 & 0 & 0 \\ 0 & 0 & 0.3333 & 0 \\ 0 & 0 & 0 & 0.1667 \end{bmatrix}$	$10^{-2}\cdot\begin{bmatrix} 2.2361 & 0 & 0 & 0 \\ 0 & 2.2361 & 0 & 0 \\ 0 & 0 & 0.6389 & 0 \\ 0 & 0 & 0 & 0.6389 \end{bmatrix}$	$10^{-2}\cdot\begin{bmatrix} 2.2361 & 0 & 1.1180 & 0 \\ 2.2361 & 0 & -1.1180 & 0 \\ 0 & 0.3194 & 0 & 0.6389 \\ 0 & -0.3194 & 0 & 0.6389 \end{bmatrix}$

Table 5.6: Weighting Matrices W_3, S, and W_4 for $\mathcal{H}_\infty$ Controller Designs

Chapter 6

$\mathcal{H}_2$ and $\mathcal{H}_\infty$ Design Results

6.1 Introduction

For the generalized plant designs in chapter 5, $\mathcal{H}_2$ and $\mathcal{H}_\infty$ controllers are synthesized via the methods described in sections 4.3.2 and 4.3.3. In particular, $\mathcal{H}_2$ controllers are produced for designs $\mathcal{A}_2$ and $\mathcal{B}_2$, and $\mathcal{H}_\infty$ controllers for designs $\mathcal{C}_\infty$ and $\mathcal{D}_\infty$. For the sake of comparison, $\mathcal{H}_\infty$ synthesis is also applied to designs $\mathcal{A}_2$ and $\mathcal{B}_2$, and $\mathcal{H}_2$ synthesis to designs $\mathcal{C}_\infty$ and $\mathcal{D}_\infty$. These latter controllers, whose method of synthesis does not match that intended during the design phase, are denoted as $\mathcal{A}_\infty$, $\mathcal{B}_\infty$, $\mathcal{C}_2$, and $\mathcal{D}_2$.

For each controller synthesized, the resulting closed loop twin lift helicopter system is evaluated and analyzed, with its performance measured against the specifications put forward in chapter 5. Results for the designs $\mathcal{A}_2$, $\mathcal{B}_2$, $\mathcal{A}_\infty$, and $\mathcal{B}_\infty$ are presented first, with those for designs $\mathcal{C}_\infty$, $\mathcal{D}_\infty$, $\mathcal{C}_2$, and $\mathcal{D}_2$ presented subsequently and in an analogous fashion. These results include controller complexity, time domain simulations, and frequency domain plots of transfer function singular values. As described in sections 5.2.2.1 and 5.2.3.1, the time domain simulations show both the zero input response to initial conditions (IC.1) and (IC.2), and the zero state response to stochastic inputs $d_p(t)$ and $d_s(t)$. Singular values are plotted for the wind-to-variable transfer functions $T_{y,d_p}(s)$, as well as for the complementary sensitivity function $C(s)$. Following the results presented for each set of designs, the controllers within each set are compared and contrasted. Differences and performance trade offs are interpreted in terms of variations in the output matrix, weighting functions, and synthesis method used. In the chapter's conclusion, the $\mathcal{H}_2$ and $\mathcal{H}_\infty$ design methodologies are each evaluated on their respective efficiency in achieving desired performance objectives.

6.2 $\mathcal{H}_2$ Designs

Recall that for designs $\mathcal{A}_2$ and $\mathcal{B}_2$, the selected outputs are Δx, $x_L - \Sigma x$, and $\Sigma\theta$, with design $\mathcal{B}_2$ including the additional output $\Sigma\dot{x}$. The weighting functions for these designs are listed in Tables 5.2 and 5.4. The order and size (matrix dimension) of these weighting functions determine the order of the generalized plant, and hence of the corresponding $\mathcal{H}_2$ or $\mathcal{H}_\infty$ compensator. Thus for designs $\mathcal{A}_2$ and $\mathcal{A}_\infty$, the controllers are of order 24, whereas for designs $\mathcal{B}_2$ and $\mathcal{B}_\infty$, the compensator order is 26.

6.2.1 Time Domain

6.2.1.1 Transient Response

Figures 6-1 to 6-9 show the transient response of the TLHS regulated variables and controls to the two initial conditions (IC.1) and (IC.2) given in section 5.2.2.1. Recall that (IC.1) affects only the SM plant, and hence only Δx, $\Delta\theta$, and ΔB_{lc} show non-zero responses. Similarly, (IC.2) affects only the ASM plant, inducing responses in the variables $x_L - \Sigma x$, $\Sigma\theta$, Δz, $\Sigma\dot{x}$, ΣB_{lc}, and $\Delta\Theta_c$.

(IC.1)

Figures 6-1 to 6-3 show the TLHS response to (IC.1). For the variable Δx, the responses among the four designs do not differ greatly. In each, Δx settles into equilibrium in around 4 seconds. The response in design $\mathcal{A}_2$ achieves only a slight improvement in magnitude over that in design $\mathcal{B}_2$. Each $\mathcal{H}_\infty$ design produces a slightly quicker response in Δx than the corresponding $\mathcal{H}_2$ design, but at the cost of a larger initial undershoot. In all of the designs, the response of Δx easily meets specification (S.1).

In all of the designs, the pitch angle response to (IC.1) shows several oscillations before settling into equilibrium in around 3 seconds. In designs $\mathcal{A}_2$ and $\mathcal{B}_2$, the responses of θ_m ($-\theta_s$) are similar in magnitude, with the response in $\mathcal{A}_2$ being slightly faster. In both of these $\mathcal{H}_2$ designs, θ_m ($-\theta_s$) achieves a peak magnitude of about 8.5°. The $\mathcal{H}_\infty$ designs produce pitch angle responses that are larger in magnitude than their corresponding $\mathcal{H}_2$ designs, with design $\mathcal{B}_\infty$ also showing a decrease in response frequency. In all of the designs, the pitch angle response meets specification (S.3). In design $\mathcal{A}_\infty$, however, the pitch angle peak magnitude equals the upper limit of this specification.

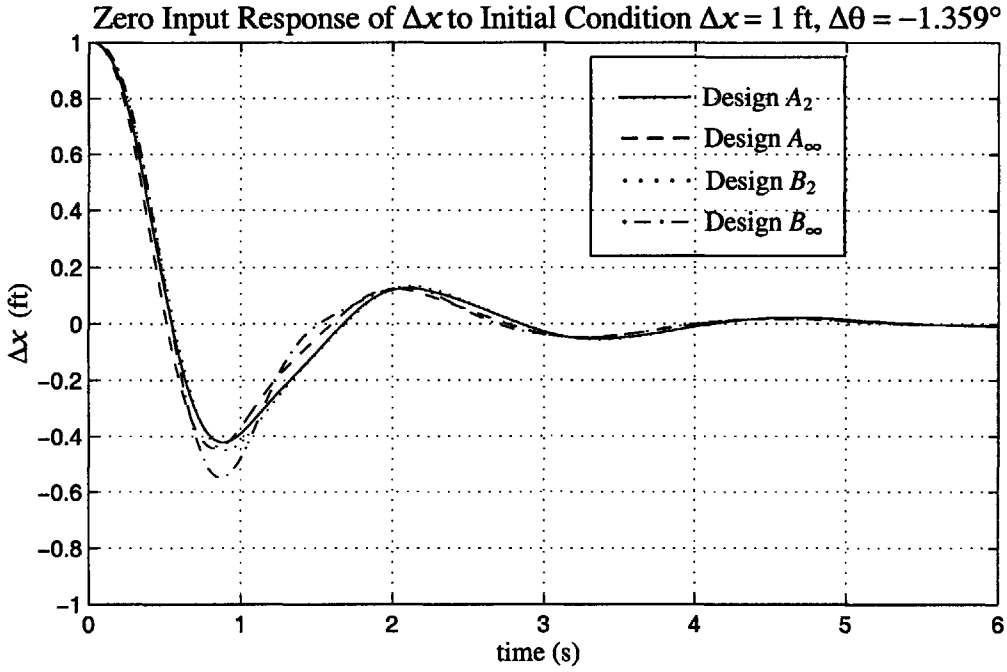

Figure 6-1: Transient Response of Δx to Initial Condition $\Delta x = 1$ ft, $\Delta\theta = -1.359°$

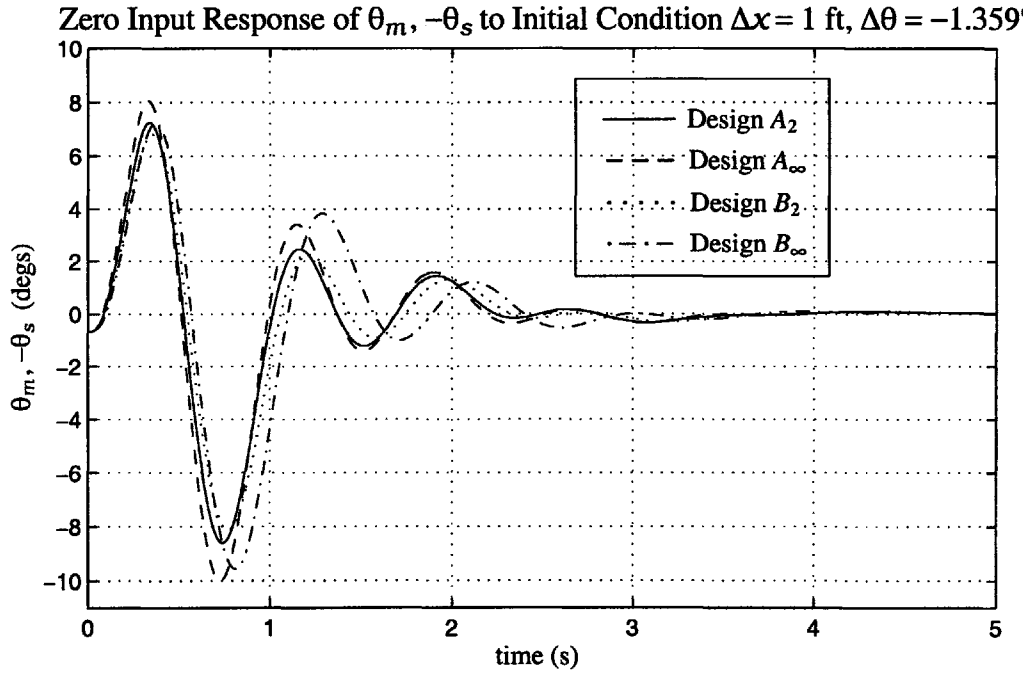

Figure 6-2: Transient Response of $\theta_m, -\theta_s$ to Initial Condition $\Delta x = 1$ ft, $\Delta\theta = -1.359°$

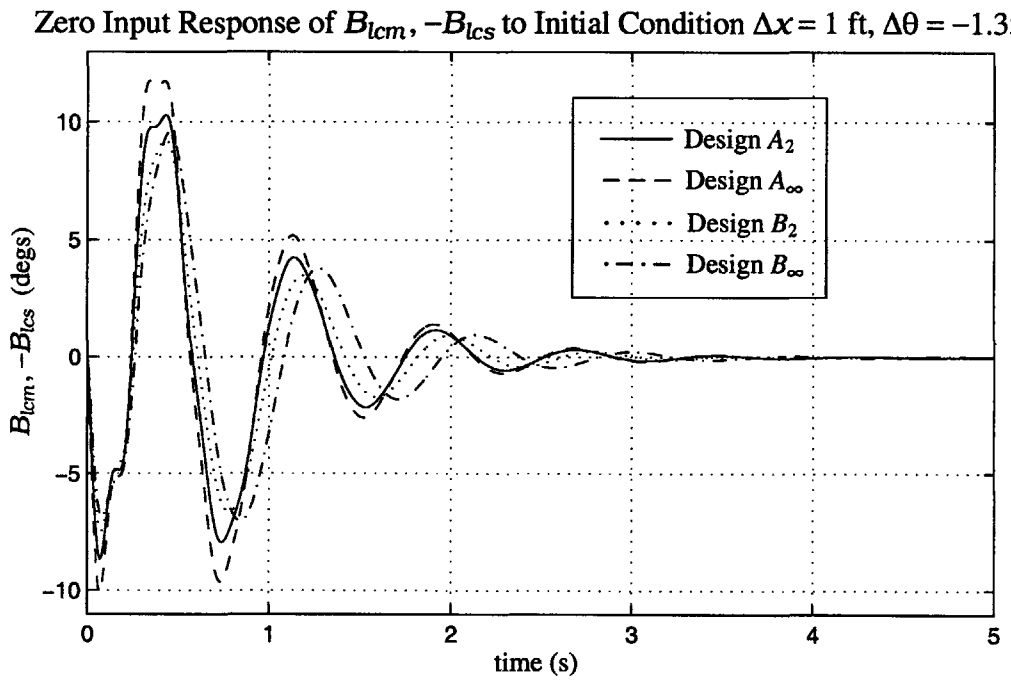

Figure 6-3: Transient Response of $B_{lcm}, -B_{lcs}$ to Initial Condition $\Delta x = 1\text{ft},\ \Delta\theta = -1.359°$

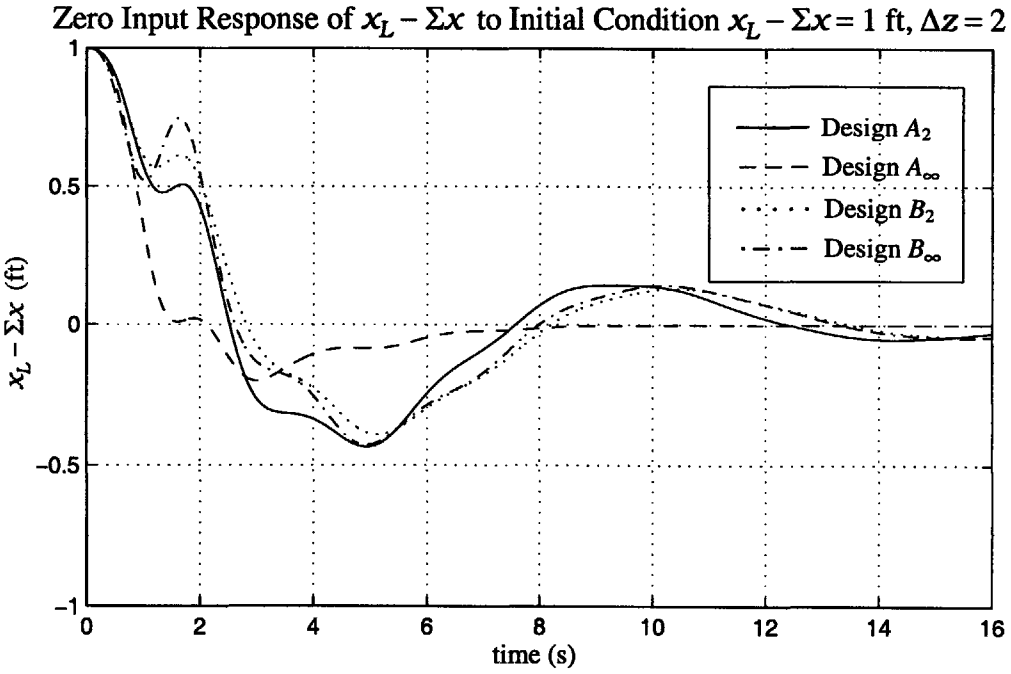

Figure 6-4: Transient Response of $x_L - \Sigma x$ to Initial Condition $x_L - \Sigma x = 1\text{ ft},\ \Delta z = 2\text{ ft}$

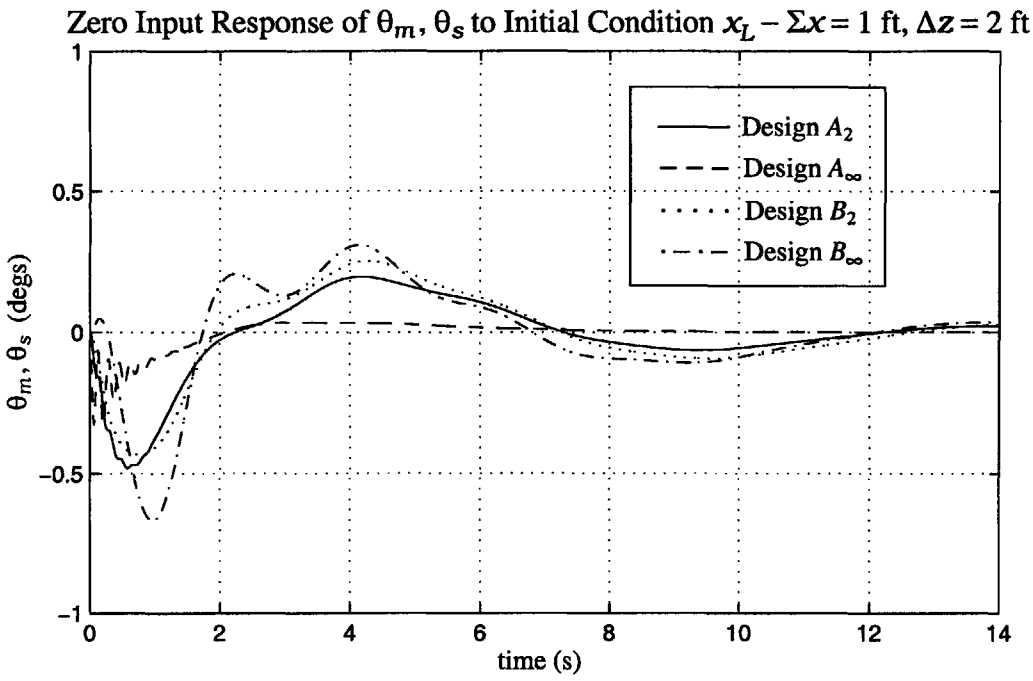

Figure 6-5: Transient Response of θ_m, θ_s to Initial Condition $x_L - \Sigma x = 1$ ft, $\Delta z = 2$ ft

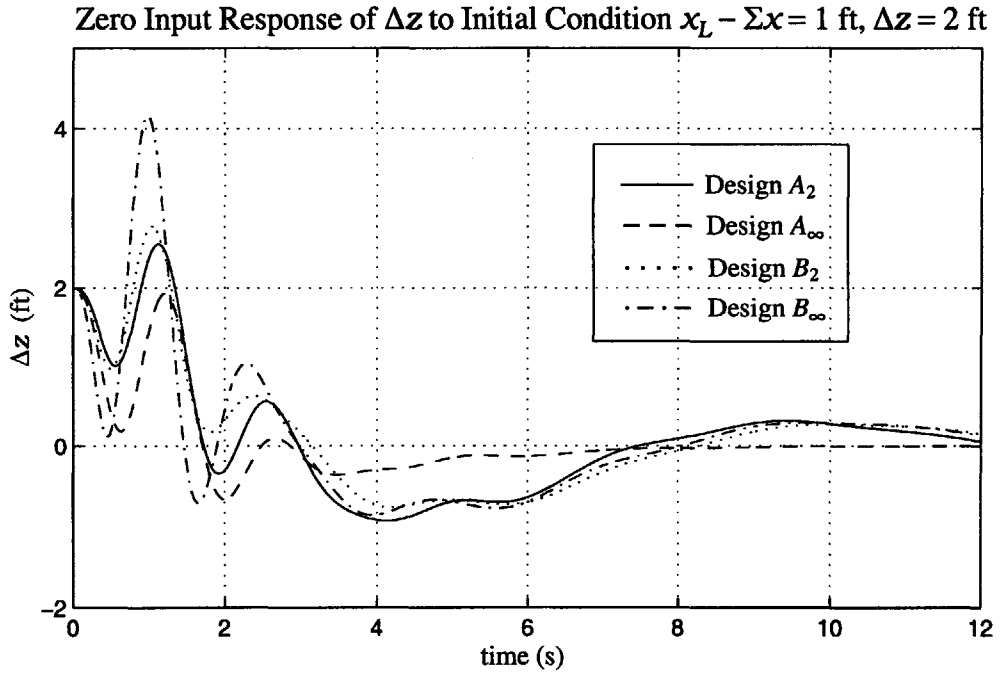

Figure 6-6: Transient Response of Δz to Initial Condition $x_L - \Sigma x = 1$ ft, $\Delta z = 2$ ft

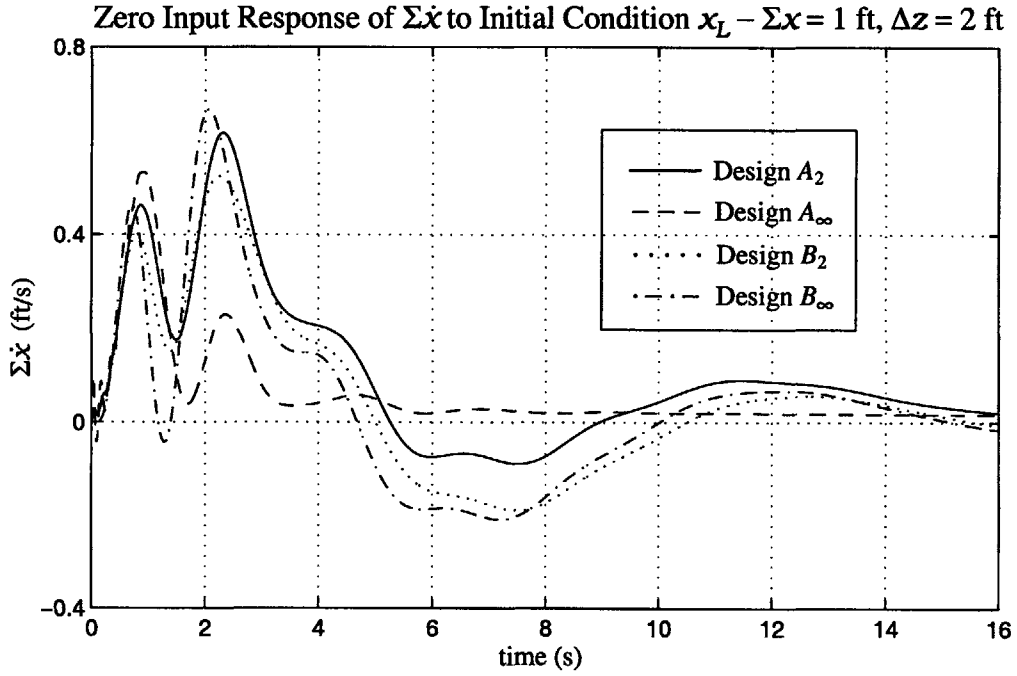

Figure 6-7: Transient Response of $\Sigma\dot{x}$ to Initial Condition $x_L - \Sigma x = 1\,\text{ft},\ \Delta z = 2\,\text{ft}$

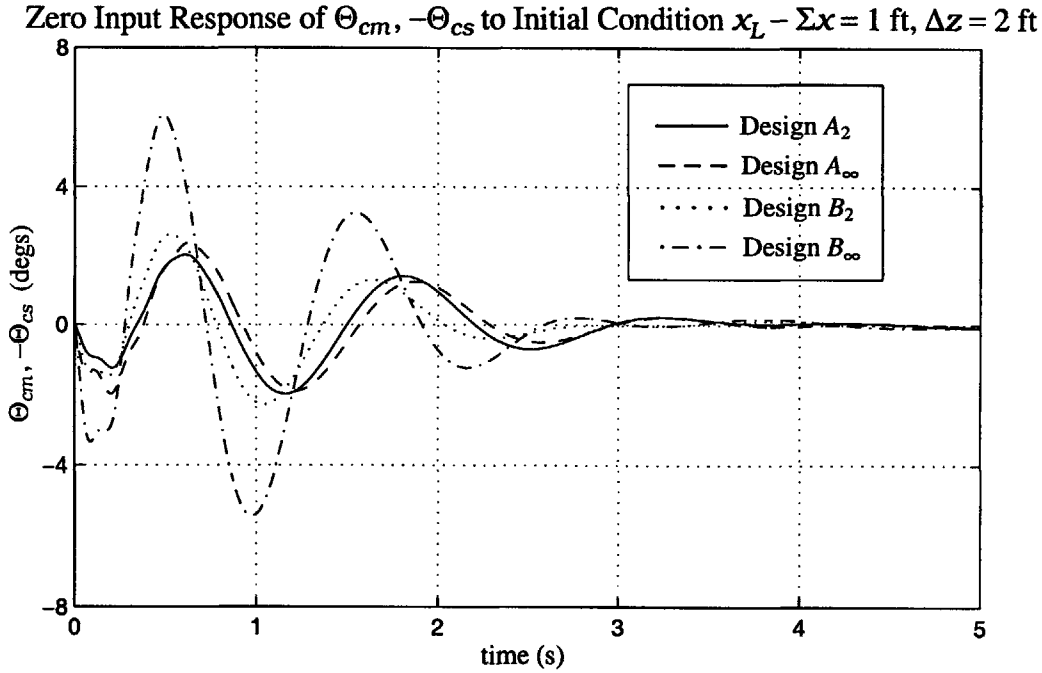

Figure 6-8: Transient Response of $\Theta_{cm}, -\Theta_{cs}$ to Initial Condition $x_L - \Sigma x = 1\,\text{ft},\ \Delta z = 2\,\text{ft}$

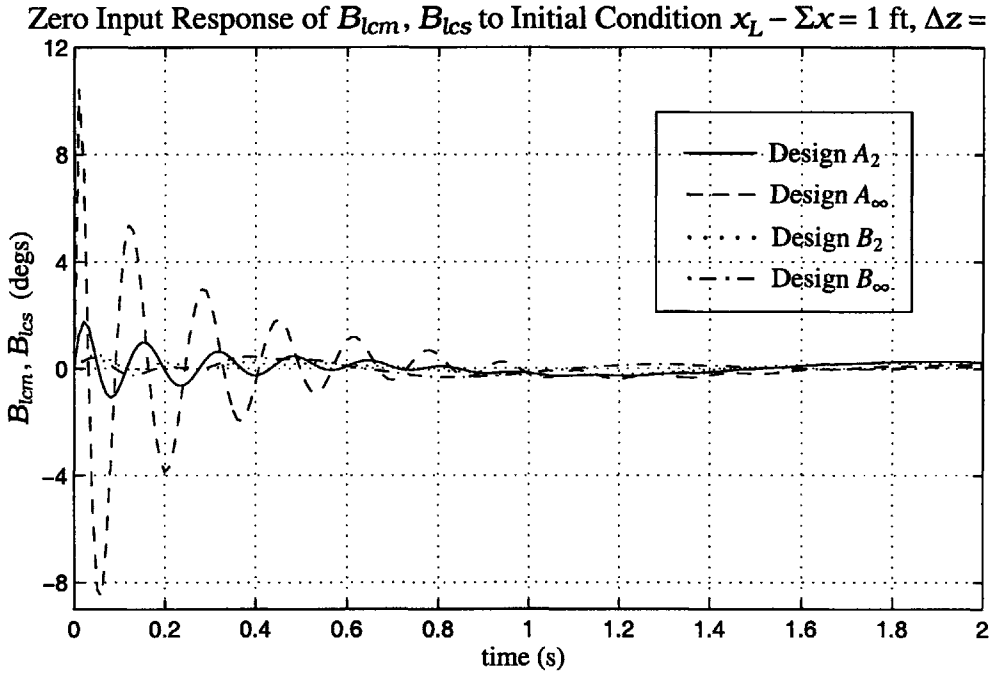

Figure 6-9: Transient Response of B_{lcm}, B_{lcs} to Initial Condition $x_L - \Sigma x = 1\,\text{ft},\ \Delta z = 2\,\text{ft}$

The nature of the cyclic control response to (IC.1) closely resembles that of the pitch angle response, with two significant differences. First, design $\mathcal{A}_2$ produces a noticeably larger cyclic response than design $\mathcal{B}_2$, in contrast to the pitch angles which exhibit equal magnitude responses in the two designs. Second, the cyclic response in design $\mathcal{B}_\infty$ is only slightly greater in magnitude than that in design $\mathcal{B}_2$. By contrast, the pitch angles in these two designs exhibit a more prominent magnitude difference. All other features of the cyclic response are similar to those of the pitch angles. In all of the designs, the response of B_{lcm} ($-B_{lcs}$) meets specification (S.13).

(IC.2)

Figures 6-4 to 6-9 show the TLHS response to (IC.2). The response of the load deviation from center in designs $\mathcal{A}_2$ and $\mathcal{B}_2$ is very similar. In each, $x_L - \Sigma x$ settles into equilibrium in about 16 seconds after exhibiting some low frequency oscillation. The response of $x_L - \Sigma x$ in design $\mathcal{B}_\infty$ closely follows that in $\mathcal{B}_2$, but with a slightly larger oscillation amplitude in the first few seconds. Design $\mathcal{A}_\infty$ achieves the best response of $x_L - \Sigma x$. In this design, $x_L - \Sigma x$ shows a very small initial undershoot before settling into equilibrium in about 8

seconds. In all of the designs, the response of $x_L - \Sigma x$ meets specification (S.2).

The pitch angle response to (IC.2) is similar in nature to that of the load deviation from center. The responses in designs $\mathcal{A}_2$ and $\mathcal{B}_2$ closely resemble each other, with that in design $\mathcal{A}_2$ usually being slightly smaller in magnitude. In each of these $\mathcal{H}_2$ designs, the pitch angle settles into equilibrium in around 14 seconds. The pitch angle response in design $\mathcal{B}_\infty$ resembles that in $\mathcal{B}_2$, but with a larger oscillation amplitude. As with the response of $x_L - \Sigma x$, the best response of θ_m (θ_s) is produced by design $\mathcal{A}_\infty$. In this design, θ_m (θ_s) shows some initial high frequency but low magnitude oscillations before settling into equilibrium in around 8 seconds. In all of the designs, the pitch angle response never exceeds a magnitude of 0.7°, and hence specification (S.3) is easily satisfied.

In all of the designs, the response of Δz to (IC.2) shows several large amplitude oscillations before settling into equilibrium. The responses in the two $\mathcal{H}_2$ designs have a similar shape, with that in design $\mathcal{B}_2$ exhibiting a slightly larger oscillation frequency and magnitude. In design $\mathcal{B}_\infty$, the response of Δz follows those in the $\mathcal{H}_2$ designs, but with a larger oscillation amplitude and a slightly increased oscillation frequency. In all three of the designs $\mathcal{A}_2$, $\mathcal{B}_2$, and $\mathcal{B}_\infty$, Δz settles into equilibrium in about 12 seconds. In design $\mathcal{A}_\infty$, Δz oscillates with a decreased amplitude and frequency relative to the other designs, settling into equilibrium in about 8 seconds. In all of the designs, the response of Δz meets specification (S.4).

As with Δz, the response of $\Sigma \dot{x}$ shows several oscillations before reaching equilibrium. The responses in designs $\mathcal{A}_2$ and $\mathcal{B}_2$ have a similar shape, with that in design $\mathcal{A}_2$ showing a larger overshoot and that in design $\mathcal{B}_2$ a larger undershoot of equilibrium. In each of these $\mathcal{H}_2$ designs, the response of $\Sigma \dot{x}$ reaches equilibrium in around 16 seconds. Design $\mathcal{B}_\infty$ produces a response similar to that in design $\mathcal{B}_2$, but with a slightly larger oscillation amplitude and frequency. As with the other regulated variables, $\Sigma \dot{x}$ settles fastest in design $\mathcal{A}_\infty$, attaining equilibrium in about 10 seconds. In all of the designs, the magnitude of $\Sigma \dot{x}$ never exceeds 0.7 ft/s, and hence specification (S.5) is easily satisfied.

The collective control response to (IC.2) is characterized by several smooth oscillations of gradually decreasing amplitude. In designs $\mathcal{A}_2$ and $\mathcal{B}_2$, the oscillations of Θ_{cm} ($-\Theta_{cs}$) are of approximately the same size, with those in design $\mathcal{B}_2$ exhibiting a slightly higher frequency. The response of Θ_{cm} ($-\Theta_{cs}$) in design $\mathcal{A}_\infty$ is very close to that in design $\mathcal{A}_2$, whereas the collective response in design $\mathcal{B}_\infty$ is close in frequency to that in design $\mathcal{B}_2$, but

much larger in amplitude. In all of the designs, the collective control settles into equilibrium in around 3 to 4 seconds, and never exceeds the bounds of specification (S.12).

Like the collective control, the cyclic control responds to (IC.2) with a series of oscillations that gradually decrease in amplitude. These oscillations, however, differ markedly from those of the collective control. In particular, in designs $\mathcal{A}_2$ and $\mathcal{A}_\infty$, the cyclic oscillations exhibit a very high frequency together with a rapid decay in magnitude, attaining equilibrium within about 2 seconds. The responses of B_{lcm} (B_{lcs}) in designs $\mathcal{B}_2$ and $\mathcal{B}_\infty$ are both of about the same frequency as those of the respective collective controls, but are of a much smaller magnitude, never exceeding 1°. By far the largest cyclic response, with a peak magnitude exceeding 10°, is produced by design $\mathcal{A}_\infty$. In this design and the others, however, B_{lcm} (B_{lcs}) remains within the bounds of specification (S.13).

6.2.1.2 Stochastic Response

For each of the controller designs, the closed loop response is observed to the stochastic inputs $d_p(t)$ and $d_s(t)$, generated as described in section 5.2.1 of chapter 5. The process noise $d_p(t)$ is kept the same for all of the simulations, and is shown in Figure 6-10. The sensor noise $d_s(t)$ is scaled based upon an initial simulation in which only $d_p(t)$ is included as an input. Before scaling, however, each sensor noise input $d_{si}(t)$, for equal i, is the same in all of the simulations. Figure 6-11 shows these sensor noises as generated for design $\mathcal{B}_2$.

In addition to stochastic plots of the TLHS variables and controls, steady state RMS values are generated for these outputs. These values are calculated from the state covariance matrix, computed as described in section 4.2.2 of chapter 4. Table 6.1 lists the RMS values

Variables/ Controls	**Design**			
	$\mathcal{A}_2$	$\mathcal{B}_2$	$\mathcal{A}_\infty$	$\mathcal{B}_\infty$
Δx	1.2157	1.2731	1.0880	0.9670
$x_L - \Sigma x$	1.6136	1.5678	1.6751	0.9422
θ_m, θ_s	1.1982	2.9063	0.9292	3.6756
Δz	2.2271	2.9759	2.2151	5.9278
$\Sigma \dot{x}$	18.555	2.5491	19.849	0.8445
Θ_{cm}, Θ_{cs}	1.8840	1.9934	0.7650	4.4397
B_{lcm}, B_{lcs}	1.9339	1.5178	1.9582	1.5261
$\Sigma \theta$	0.6836	2.7159	0.2628	3.5875

Table 6.1: RMS Values of Variables and Controls with Input $d_p(t)$

Variables/ Controls	Design			
	$\mathcal{A}_2$	$\mathcal{B}_2$	$\mathcal{A}_\infty$	$\mathcal{B}_\infty$
Δx	1.2166	1.2741	1.0889	0.9679
$x_L - \Sigma x$	1.6138	1.5687	1.6753	0.9479
θ_m, θ_s	1.5478	3.0598	1.3802	3.8247
Δz	2.2350	3.0083	2.2220	6.0669
$\Sigma \dot{x}$	18.555	2.5503	19.849	0.8626
Θ_{cm}, Θ_{cs}	1.9300	2.3953	0.8701	6.2551
B_{lcm}, B_{lcs}	2.6266	2.2317	3.9978	2.4430
$\Sigma \theta$	0.6844	2.7169	0.2664	3.5901

Table 6.2: RMS Values of Variables and Controls with Inputs $d_p(t)$ and $d_s(t)$

when only the process noise $d_p(t)$ is included as an input. It is from this table that the scaling factors r_i for each sensor noise $d_{si}(t)$ are taken. Table 6.2 then lists the RMS values when the input includes both process and sensor noise.

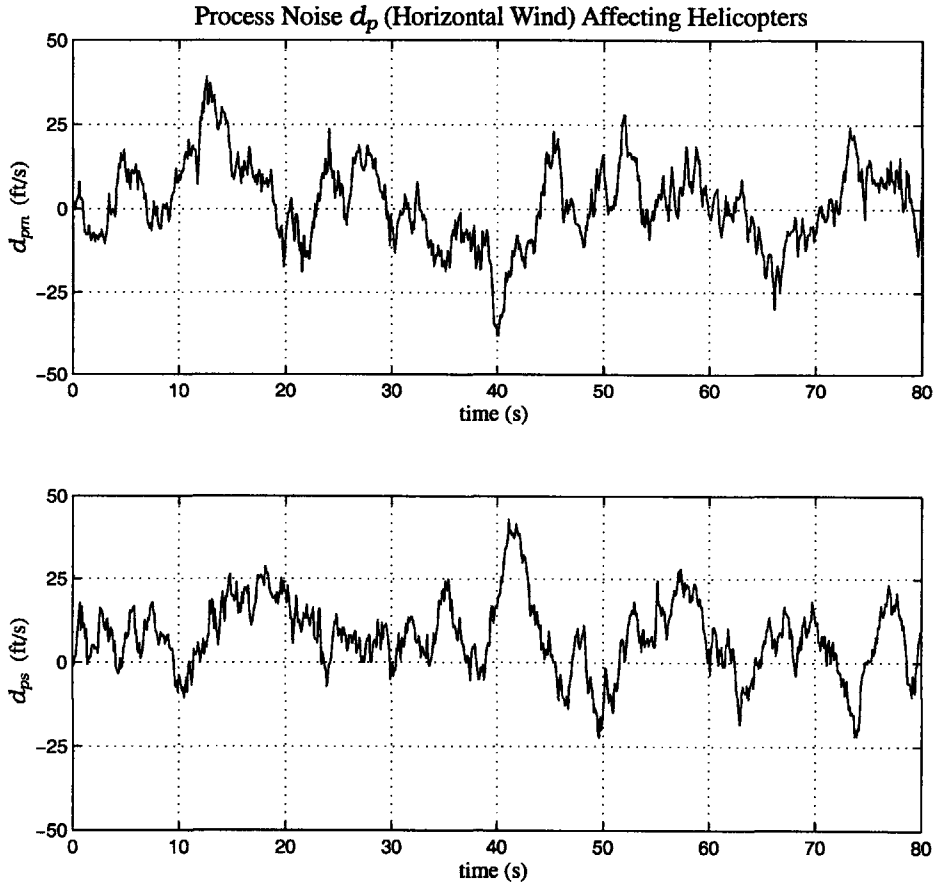

Figure 6-10: Process Noise d_p for Stochastic Simulations

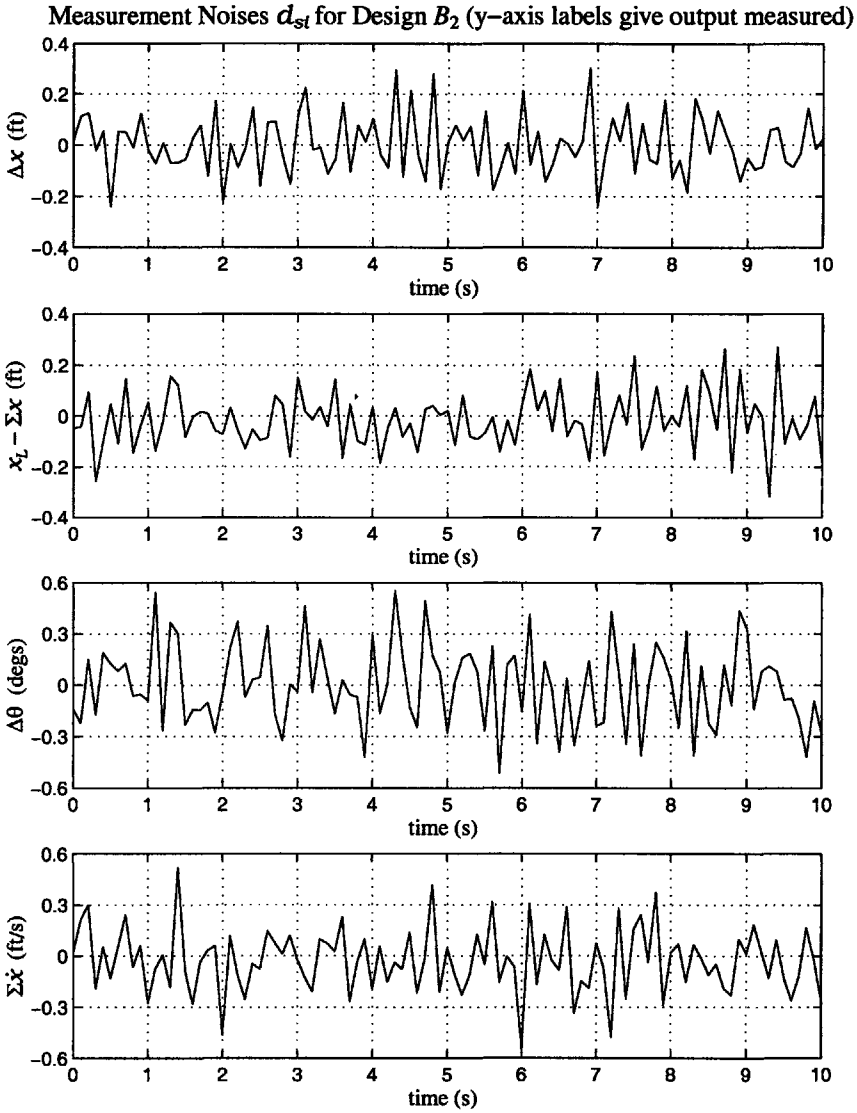

Figure 6-11: Sensor Noise d_s for Design $\mathcal{B}_2$

Figures 6-12 to 6-20 show the stochastic response of the TLHS to the inputs $d_p(t)$ and $d_s(t)$. For the variable Δx, the responses in all of the designs are similarly in shape, differing noticeably only in magnitude. In this respect, Δx appears slightly smaller in design $\mathcal{A}_2$ than in design $\mathcal{B}_2$. This magnitude reduction is consistent with the RMS values calculated for these two designs, of 1.22 and 1.27 respectively. The magnitude of Δx in each $\mathcal{H}_\infty$ design is smaller than in the $\mathcal{H}_2$ designs, with the greatest magnitude reduction occurring in design $\mathcal{B}_\infty$. This result is again consistent with the RMS values calculated for designs $\mathcal{A}_\infty$ and $\mathcal{B}_\infty$, of 1.09 and 0.97 respectively. In all of the designs, the stochastic response does not exceed the magnitude of 6 ft, and hence specification (S.1) is satisfied.

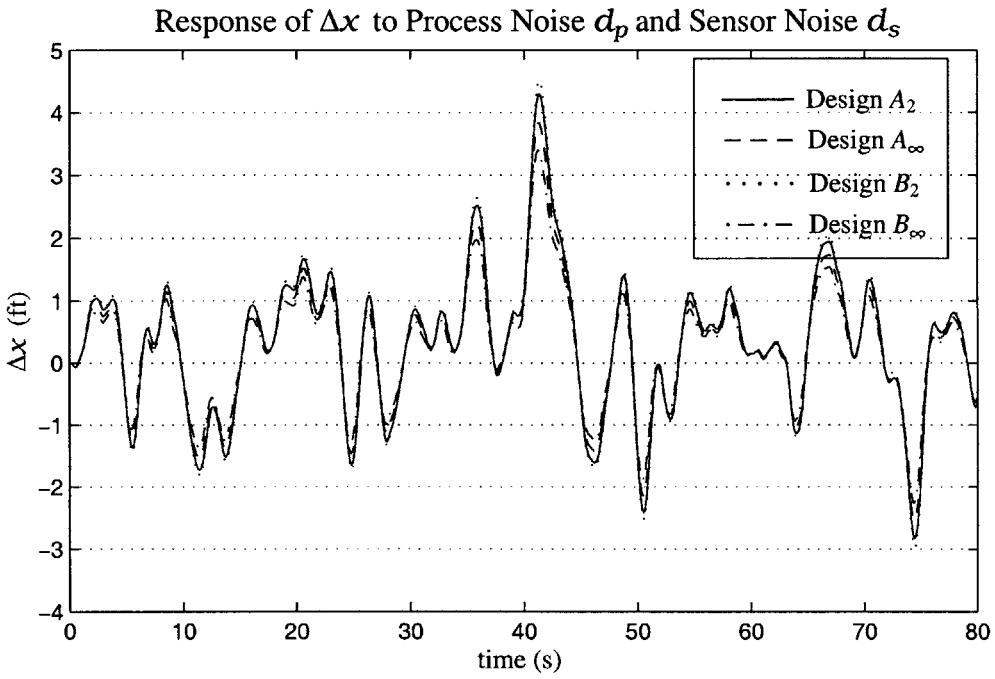

Figure 6-12: Stochastic Response of Δx to Process Noise d_p and Sensor Noise d_s

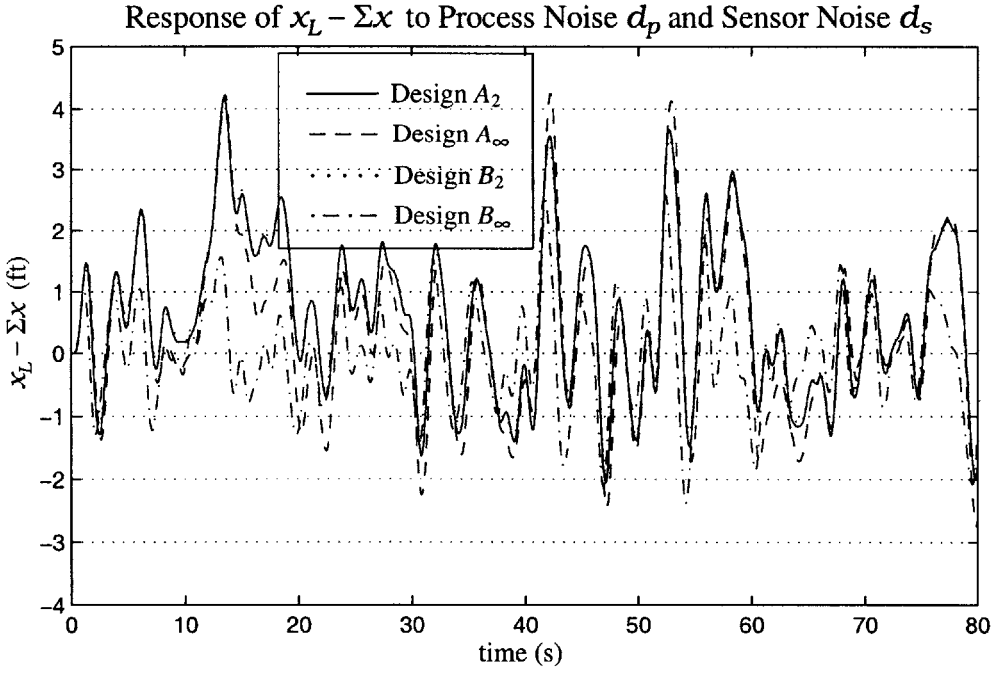

Figure 6-13: Stochastic Response of $x_L - \Sigma x$ to Process Noise d_p and Sensor Noise d_s

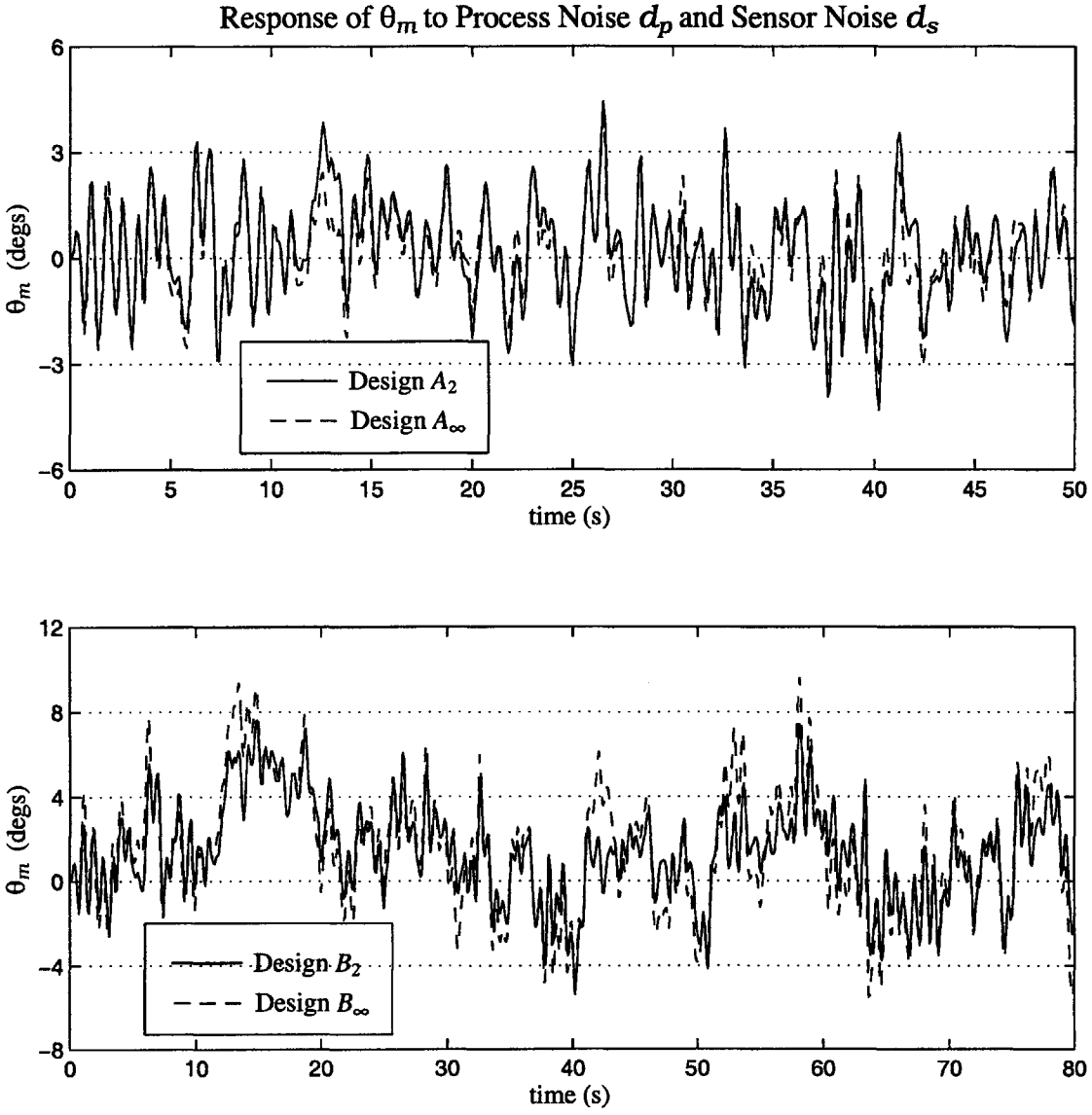

Figure 6-14: Stochastic Response of θ_m to Process Noise d_p and Sensor Noise d_s

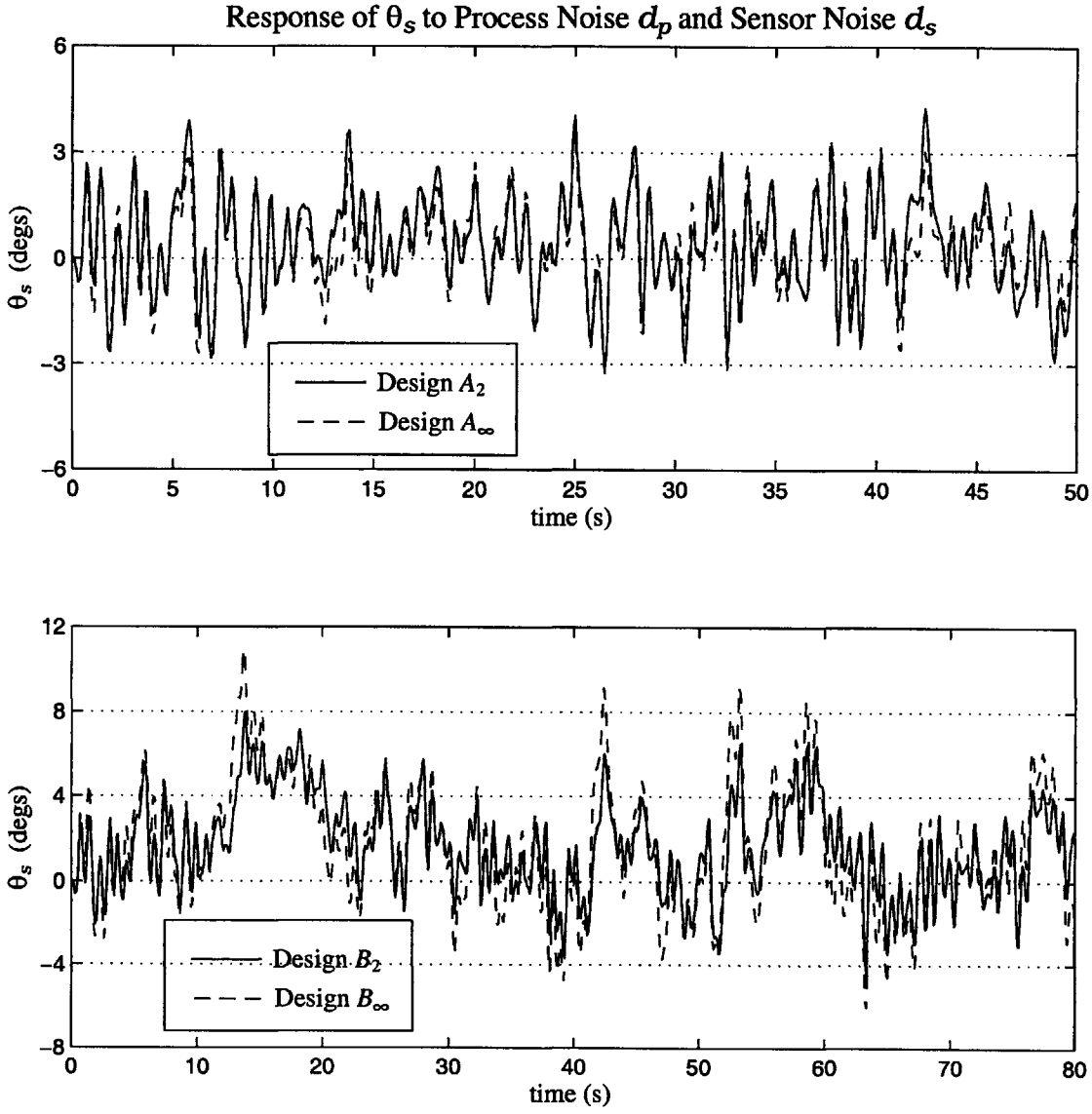

Figure 6-15: Stochastic Response of θ_s to Process Noise d_p and Sensor Noise d_s

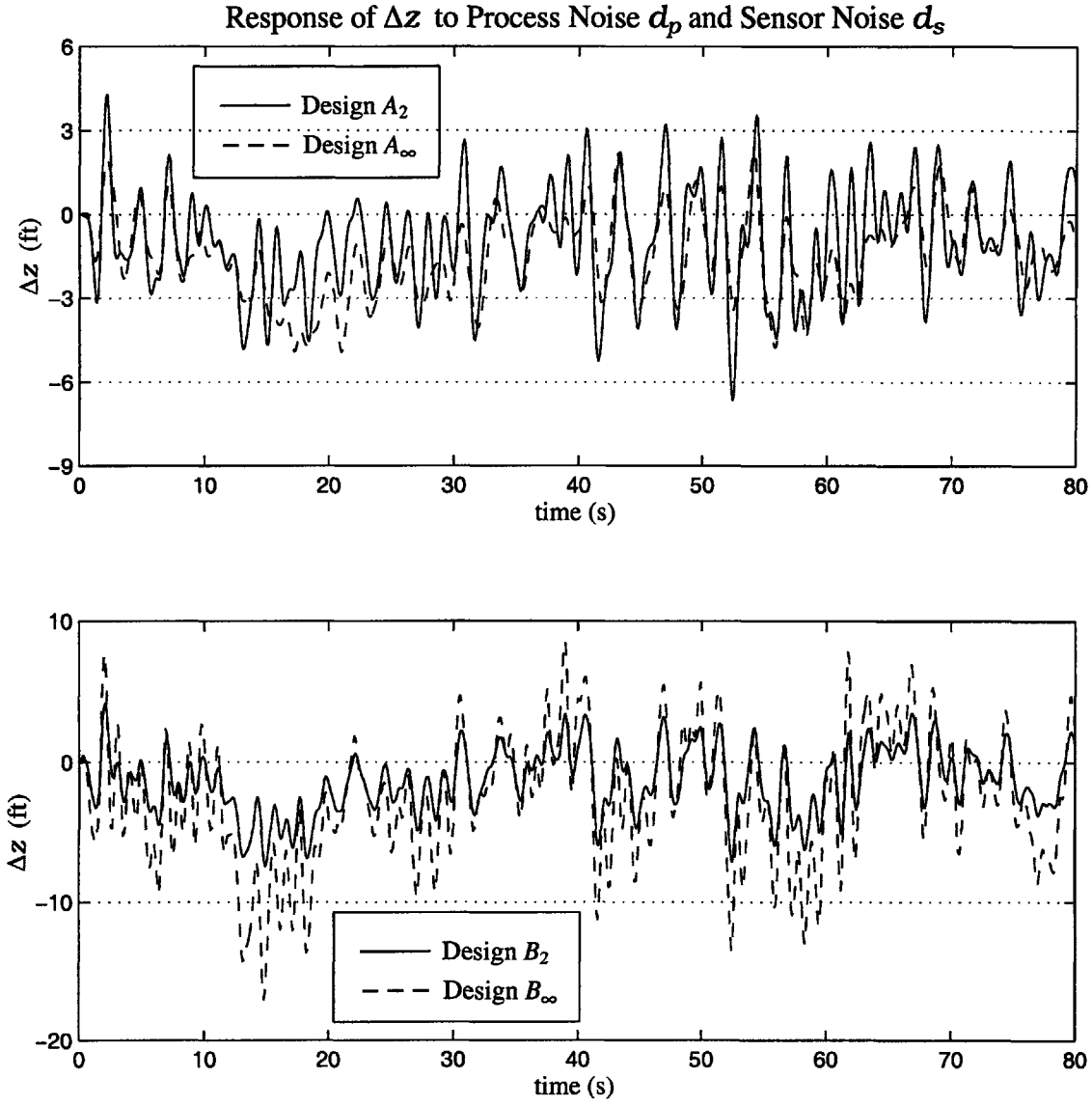

Figure 6-16: Stochastic Response of Δz to Process Noise d_p and Sensor Noise d_s

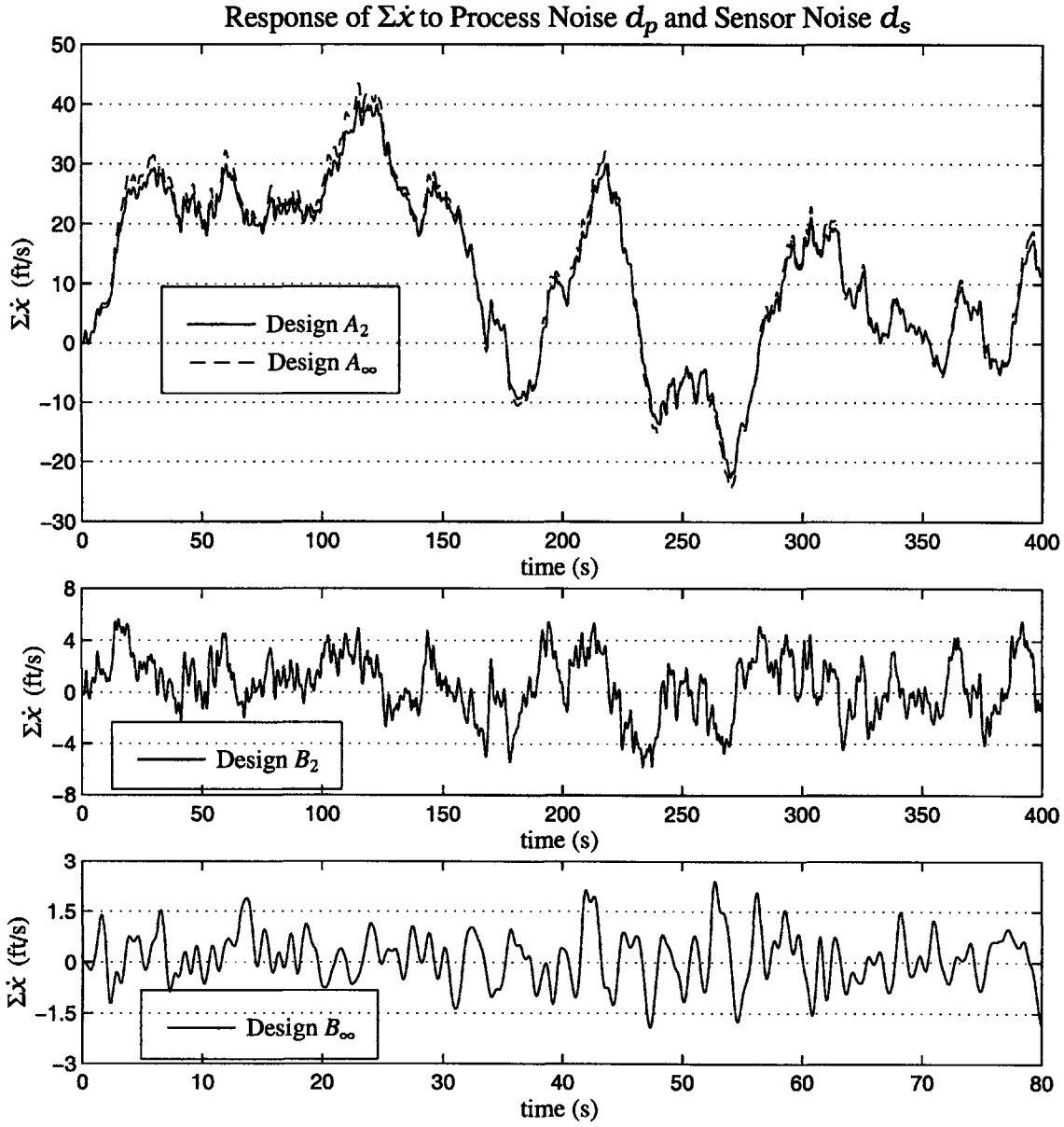

Figure 6-17: Stochastic Response of $\Sigma\dot{x}$ to Process Noise d_p and Sensor Noise d_s

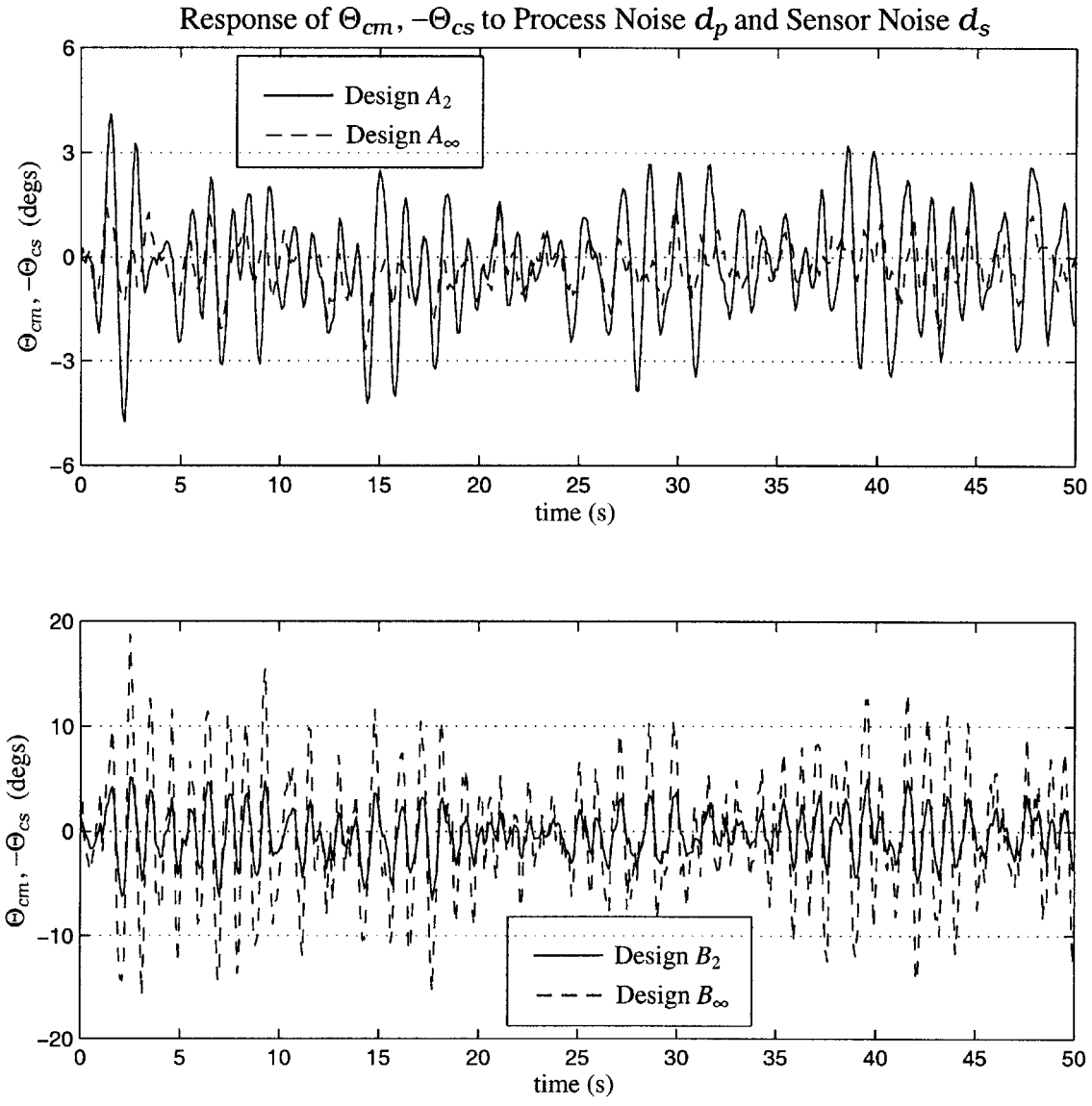

Figure 6-18: Stochastic Response of $\Theta_{cm}, -\Theta_{cs}$ to Process Noise d_p and Sensor Noise d_s

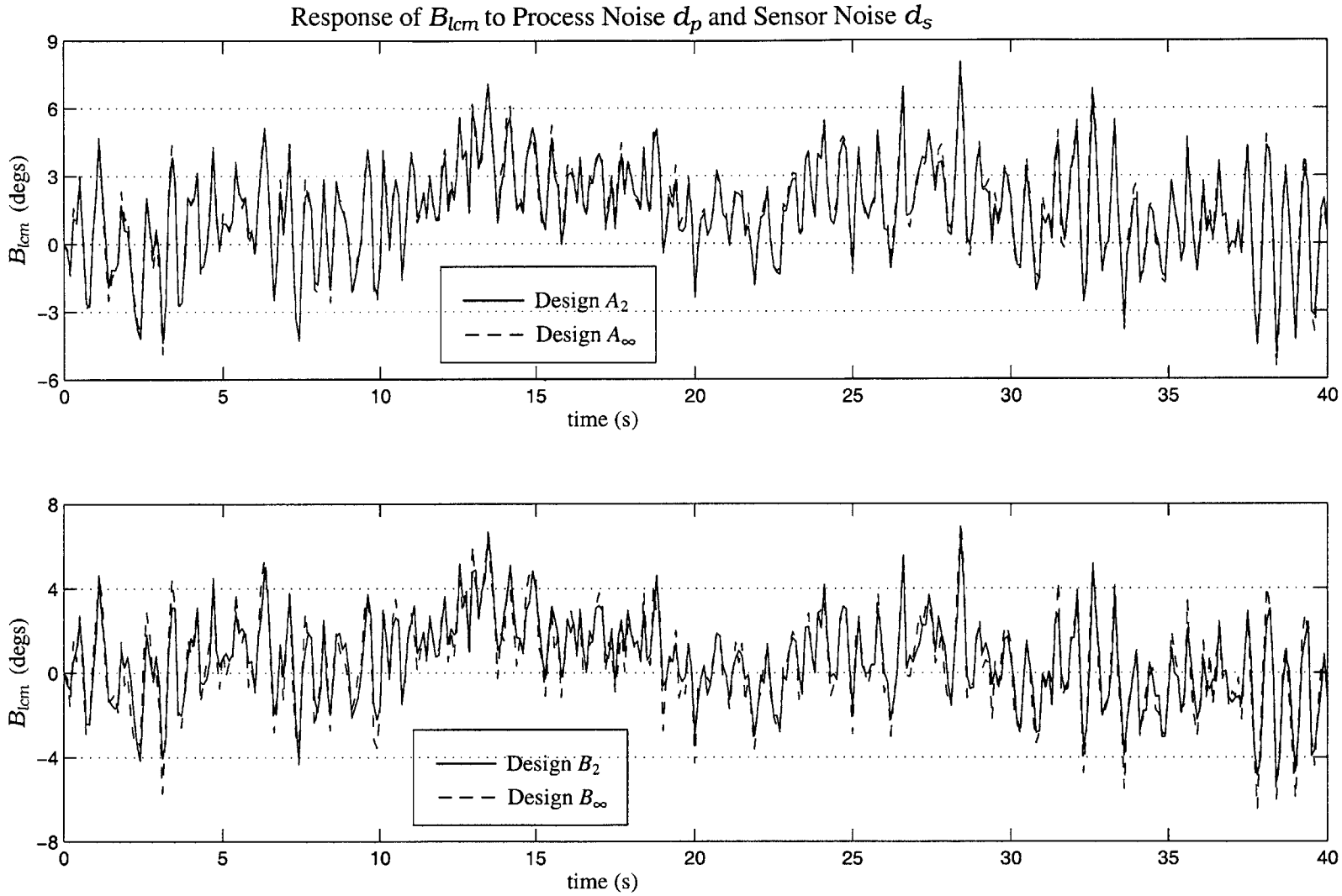

Figure 6-19: Stochastic Response of B_{lcm} to Process Noise d_p and Sensor Noise d_s

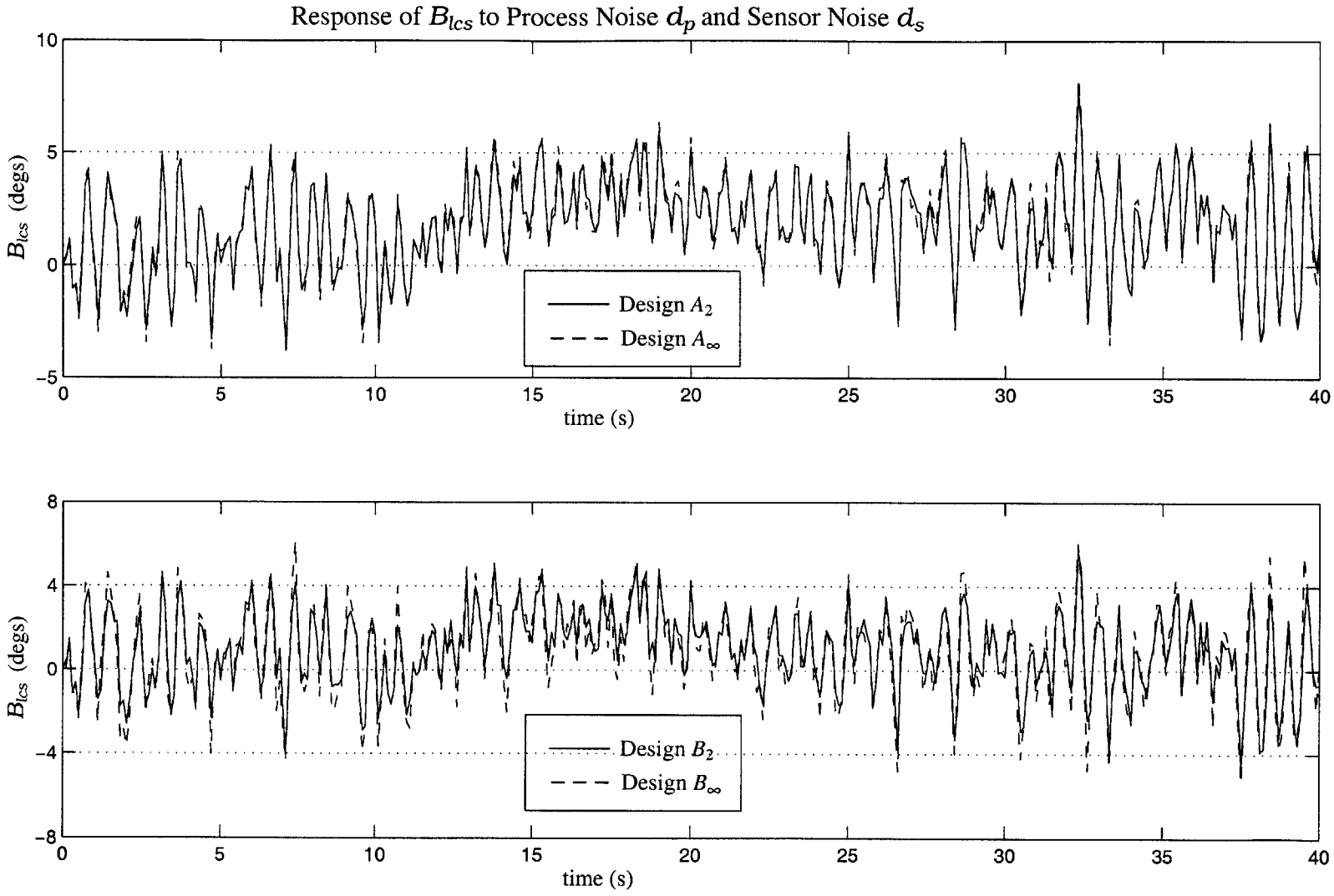

Figure 6-20: Stochastic Response of B_{lcs} to Process Noise d_p and Sensor Noise d_s

The load deviation from center exhibits nearly identical responses in designs $\mathcal{A}_2$ and $\mathcal{B}_2$, with that in design $\mathcal{B}_2$ showing a slightly greater magnitude reduction. The RMS values for designs $\mathcal{A}_2$ and $\mathcal{B}_2$ are also very close, at 1.61 and 1.57 respectively. Compared to Δx, the responses of $x_L - \Sigma x$ in the $\mathcal{H}_\infty$ designs differ significantly from those in the $\mathcal{H}_2$ designs. In design $\mathcal{A}_\infty$, this difference is primarily one of magnitude. While $x_L - \Sigma x$ in design $\mathcal{A}_\infty$ follows an oscillatory shape similar to that in design $\mathcal{A}_2$, the two responses often oscillate at different amplitudes, with design $\mathcal{A}_\infty$ usually, but not always, producing the larger response. The RMS value for design $\mathcal{A}_\infty$, at 1.67, is only slightly larger than that for design $\mathcal{A}_2$. Among the four designs, the most noticeably different response of $x_L - \Sigma x$ is produced by design $\mathcal{B}_\infty$. In this design, $x_L - \Sigma x$ generally exhibits the same pattern of oscillations seen in the other designs, but with less extreme deviations from equilibrium. These smaller deviations are reflected in the RMS value calculated for this design, of only 0.95. In addition, the waveform in design $\mathcal{B}_\infty$ intermittently exhibits small amplitude oscillations of a higher frequency than those present in the other responses. In all of the designs, the stochastic response of $x_L - \Sigma x$ never exceeds the bounds of specification (S.2).

The responses of the pitch angles in designs $\mathcal{A}_2$ and $\mathcal{B}_2$ show large differences both in shape and in magnitude. With respect to magnitude, the pitch angles in design $\mathcal{A}_2$ remain within a range of $\pm 5°$, whereas in design $\mathcal{B}_2$, θ_m and θ_s reach a magnitude as large as $8°$. Consistent with these observed magnitude differences, the pitch angle RMS values for these two designs are 1.55 and 3.06 respectively. In terms of overall shape, the responses in design $\mathcal{A}_2$ consist of uniformly high frequency oscillations, whereas in design $\mathcal{B}_2$, these same high frequency oscillations are present, but are superimposed with an additional lower frequency, smaller amplitude waveform. To capture this lower frequency component of the response, the simulations for design $\mathcal{B}_2$ are shown over a longer time interval than in design $\mathcal{A}_2$. The pitch angle responses in designs $\mathcal{A}_\infty$ and $\mathcal{B}_\infty$ closely resemble those in the corresponding $\mathcal{H}_2$ designs, with design $\mathcal{A}_\infty$ producing slightly more, and design $\mathcal{B}_\infty$ modestly less, magnitude reduction. The RMS values for these $\mathcal{H}_\infty$ designs are 1.38 and 3.82 respectively. In designs $\mathcal{A}_2$, $\mathcal{A}_\infty$, and $\mathcal{B}_2$, the pitch angle responses meet specification (S.3). In design $\mathcal{B}_\infty$, however, θ_m and θ_s both exceed the magnitude of $10°$, and hence specification (S.3) is violated.

For the variable Δz, all of the designs produce responses which are similar in shape but differ in magnitude. The responses in designs $\mathcal{A}_2$ and $\mathcal{B}_2$ show a modest magnitude difference, with the peaks in design $\mathcal{B}_2$ generally exceeding those in design $\mathcal{A}_2$. The RMS

values for designs $\mathcal{A}_2$ and $\mathcal{B}_2$ are 2.24 and 3.01 respectively. The response of Δz in design $\mathcal{A}_\infty$ closely follows that in design $\mathcal{A}_2$, but with a slightly smaller magnitude and corresponding RMS. The response of Δz in design $\mathcal{B}_\infty$ shows high frequency oscillations similar to those in the other designs, but greater in amplitude, and superimposed with an additional lower frequency waveform. Consequently, the RMS value for Δz in this design, at 6.07, is the largest among all of the values calculated. In designs $\mathcal{A}_2$, $\mathcal{A}_\infty$, and $\mathcal{B}_2$, the response of Δz never exceeds a magnitude of 8 ft, and hence specification (S.4) is satisfied. In design $\mathcal{B}_\infty$, however, the magnitude of Δz, which peaks at 17 ft, repeatedly exceeds the 10 ft magnitude constraint of this specification.

The stochastic response of $\Sigma\dot{x}$ in designs $\mathcal{A}_2$ and $\mathcal{B}_2$ is characterized by small amplitude high frequency oscillations superimposed with larger amplitude lower frequency oscillations. In design $\mathcal{B}_2$, a superposition of two different frequency waveforms is evident. While these same waveforms can be seen in design $\mathcal{A}_2$, their appearance is greatly diminished by their superposition with a much larger amplitude and lower frequency oscillation. As a result of this larger amplitude contribution to the response, the magnitude of $\Sigma\dot{x}$ in design $\mathcal{A}_2$ greatly exceeds that in design $\mathcal{B}_2$. In fact, while $\Sigma\dot{x}$ in design $\mathcal{B}_2$ stays within ± 6 ft/s, this variable in design $\mathcal{A}_2$ peaks at over 40 ft/s. This magnitude contrast is reflected as well in the RMS values for these two designs, of 18.6 and 2.55 respectively. The response of $\Sigma\dot{x}$ in design $\mathcal{A}_\infty$ is nearly identical to that in design $\mathcal{A}_2$, but with a slightly larger magnitude and corresponding RMS. In design $\mathcal{B}_\infty$, the response of $\Sigma\dot{x}$ consists of uniformly high frequency oscillations of very small amplitude. The RMS for this design, of only 0.86, is by far the smallest of all the values calculated. In designs $\mathcal{B}_2$ and $\mathcal{B}_\infty$, the response of $\Sigma\dot{x}$ easily meets specification (S.5). In designs $\mathcal{A}_2$ and $\mathcal{A}_\infty$, however, the 15 ft/s magnitude constraint of this specification is severely and repeatedly eclipsed.

The collective control responses in the four designs follow a similar shape but differ in magnitude. In each, Θ_{cm} $(-\Theta_{cs})$ exhibits high frequency oscillations that vary periodically in amplitude. The magnitude of the response in design $\mathcal{A}_2$ is smaller than that in design $\mathcal{B}_2$, with corresponding RMS values of 1.93 and 2.40 respectively. The collective response in design $\mathcal{A}_\infty$ is similar in shape to that in design $\mathcal{A}_2$, but shows a greatly reduced magnitude, with a corresponding RMS of only 0.87. The response in design $\mathcal{A}_\infty$ also exhibits some small oscillations of a higher frequency than those seen in the other designs. Design $\mathcal{B}_\infty$ produces by far the largest collective response, with a peak magnitude of 19°, and corresponding

RMS of 6.26. In designs $\mathcal{A}_2$, $\mathcal{A}_\infty$, and $\mathcal{B}_2$, the response of Θ_{cm} $(-\Theta_{cs})$ never exceeds a magnitude of 7°, and hence specification (S.12) is satisfied. In design $\mathcal{B}_\infty$, however, Θ_{cm} $(-\Theta_{cs})$ repeatedly violates the 10° magnitude constraint of this specification.

The cyclic control responses in the four designs are all very similar, both in shape and in magnitude. In each, B_{lcm} and B_{lcs} exhibit very high frequency oscillations superimposed with lower frequency, smaller amplitude oscillations. The responses in design $\mathcal{A}_2$ are slightly larger than those in design $\mathcal{B}_2$. These two $\mathcal{H}_2$ designs have RMS values of 2.63 and 2.23 respectively. The $\mathcal{H}_\infty$ designs produce cyclic responses slightly larger in magnitude than those in the corresponding $\mathcal{H}_2$ designs. The RMS values for designs $\mathcal{A}_\infty$ and $\mathcal{B}_\infty$ are 4.00 and 2.44 respectively. In all of the designs, the responses of B_{lcm} and B_{lcs} satisfy specification (S.13).

6.2.2 Frequency Domain

Figures 6-21 to 6-28 show the maximum singular value plots for each of the controller designs. The first set of plots are for the transfer functions from the wind disturbances, $d_p(t)$, to each of the TLHS regulated variables and controls. These plots also show the frequency domain specifications for process noise rejection put forward in sections 5.2.2.2 and 5.2.3.2 of chapter 5. The last plot, in Figure 6-28, is for the complementary sensitivity function $C(s)$. The two specifications relating to this transfer function are (S.11), for sensor noise rejection, and (S.16), for stability robustness to a time delay. Hence Figure 6-28 also includes markers of the coordinates relevant to specification (S.11), together with a plot of the bounding function in specification (S.16).

6.2.2.1 Wind Disturbance Transfer Functions

Figures 6-21 to 6-27 show the maximum singular values for the transfer functions from $d_p(t)$ to each of the regulated variables and controls. The maximum singular values for $T_{\Delta x,d_p}(j\omega)$ have the same shape in all of the designs, but differ in magnitude. At frequencies below 0.3 rad/s, where the process noise energy is greatest, the shape of $\sigma_{\max}[T_{\Delta x,d_p}(j\omega)]$ is relatively flat, with gains below the specification value of -20 dB. The responses then peak at around 2 rad/s before rolling off. At frequencies below this rolling off, design $\mathcal{B}_\infty$ shows the greatest magnitude reduction, followed in order by design $\mathcal{A}_\infty$, $\mathcal{A}_2$, and lastly $\mathcal{B}_2$. Note that this ordering matches exactly that produced by comparing the RMS values for

Δx among the four designs. $\sigma_{\max}[T_{\Delta x,d_p}(j\omega)]$ in all of the designs meets specification (S.6) for process noise rejection.

The responses of $\sigma_{\max}[T_{x_L-\Sigma x,d_p}(j\omega)]$ in designs $\mathcal{A}_2$ and $\mathcal{B}_2$ are nearly identical, with that in design $\mathcal{B}_2$ having a slightly larger gain over frequencies below 0.3 rad/s, and that in design $\mathcal{A}_2$ having a slightly larger gain for frequencies above 0.3 rad/s. The gains of these responses over the lower frequency range are approximately constant, and stay below the specification value of -20 dB. The responses then peak at between 2 and 3 rad/s before rolling off. The responses of $\sigma_{\max}[T_{x_L-\Sigma x,d_p}(j\omega)]$ in designs $\mathcal{A}_\infty$ and $\mathcal{B}_\infty$ have smaller gains over the lower frequency range than the $\mathcal{H}_2$ designs, with design $\mathcal{B}_\infty$ showing by far the greatest magnitude reduction. The two $\mathcal{H}_\infty$ responses then converge with the $\mathcal{H}_2$ responses as they peak and roll off. Consistent with the singular value plots, the RMS values for $x_L - \Sigma x$ in designs $\mathcal{A}_2$ and $\mathcal{B}_2$ are nearly identical, with design $\mathcal{B}_\infty$ producing by far the smallest RMS. Design $\mathcal{A}_\infty$, however, produces an RMS slightly larger than those in the $\mathcal{H}_2$ designs, likely because at frequencies between 0.3 and 2 rad/s, the gain in design $\mathcal{A}_\infty$ is actually significantly larger than the gains in the $\mathcal{H}_2$ designs. All of the designs meet specification (S.7) for process noise rejection.

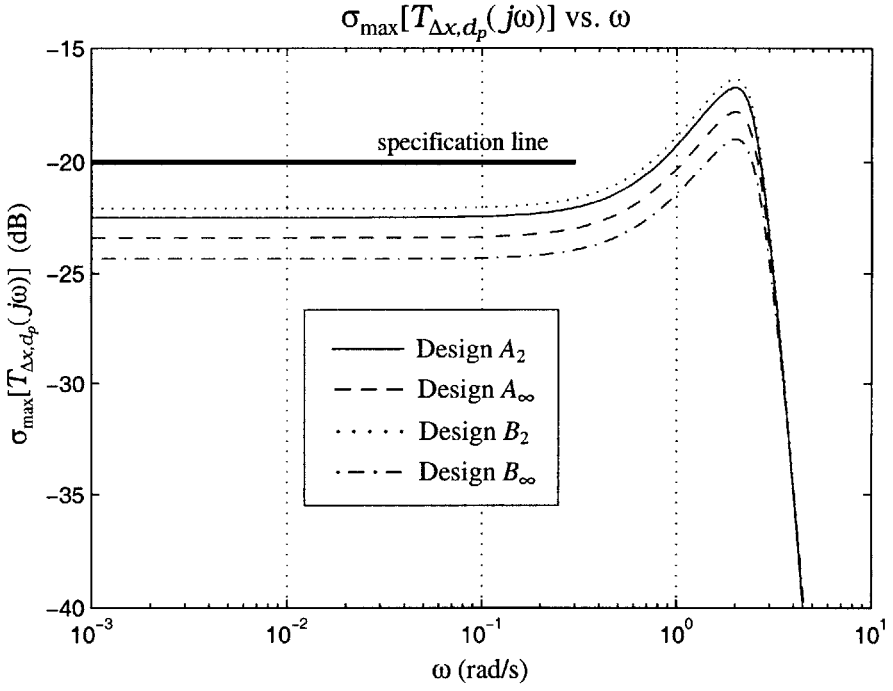

Figure 6-21: Maximum Singular Value of Transfer Function from d_p to Δx

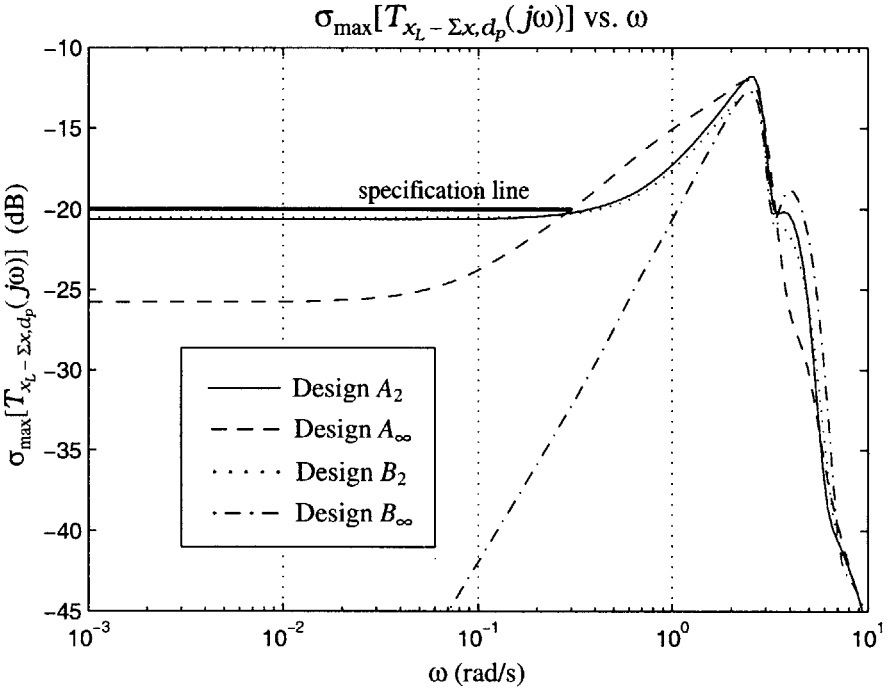

Figure 6-22: Maximum Singular Value of Transfer Function from d_p to $x_L - \Sigma x$

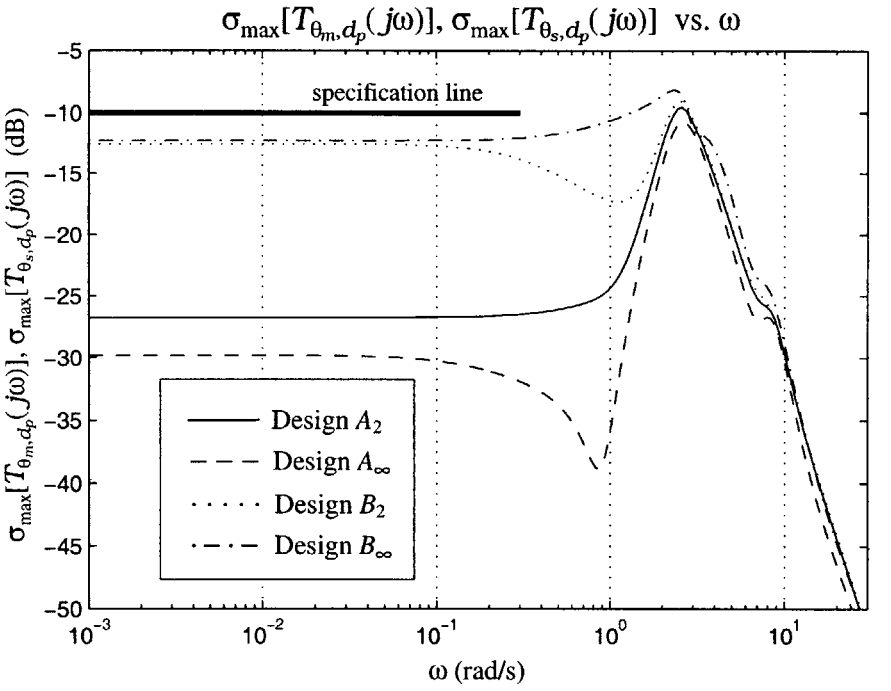

Figure 6-23: Maximum Singular Value of Transfer Function from d_p to θ_m, θ_s

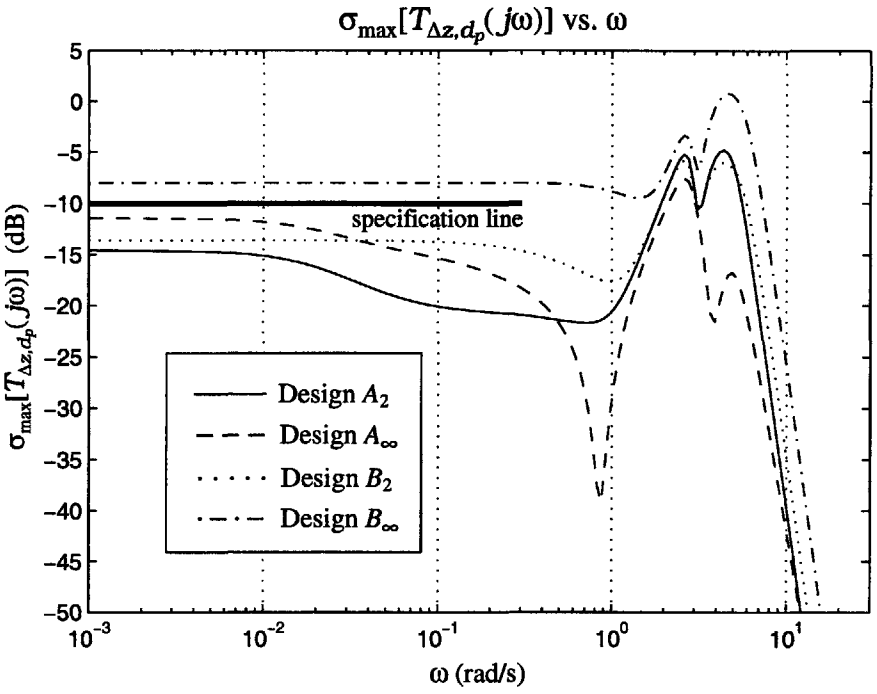

Figure 6-24: Maximum Singular Value of Transfer Function from d_p to Δz

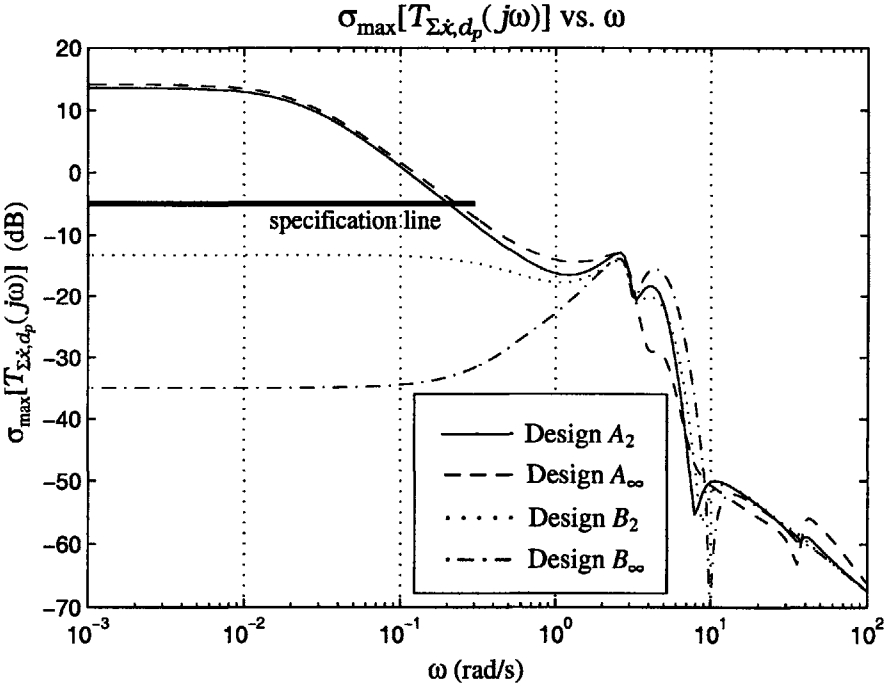

Figure 6-25: Maximum Singular Value of Transfer Function from d_p to $\Sigma\dot{x}$

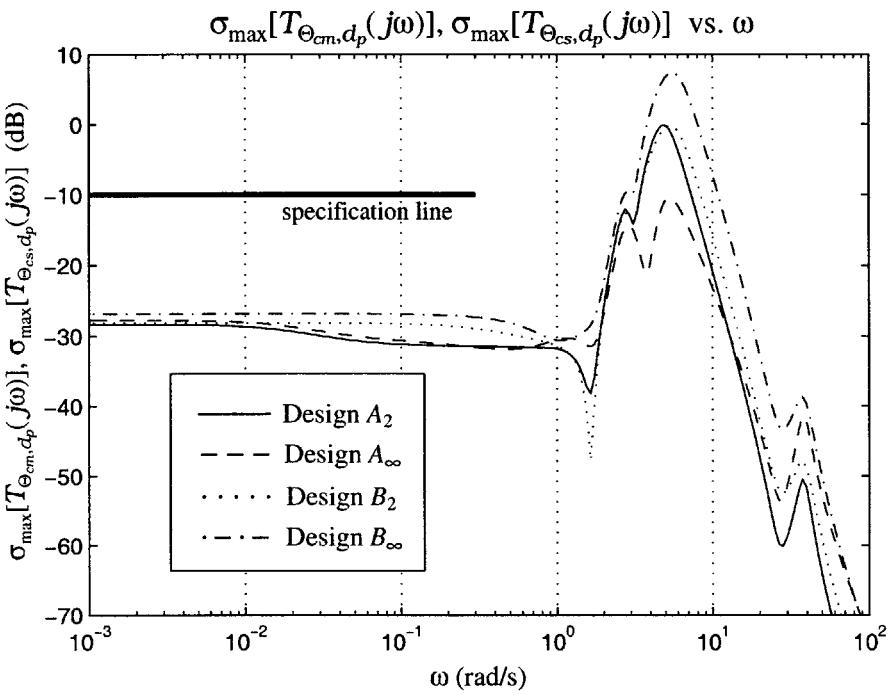

Figure 6-26: Maximum Singular Value of Transfer Function from d_p to Θ_{cm}, Θ_{cs}

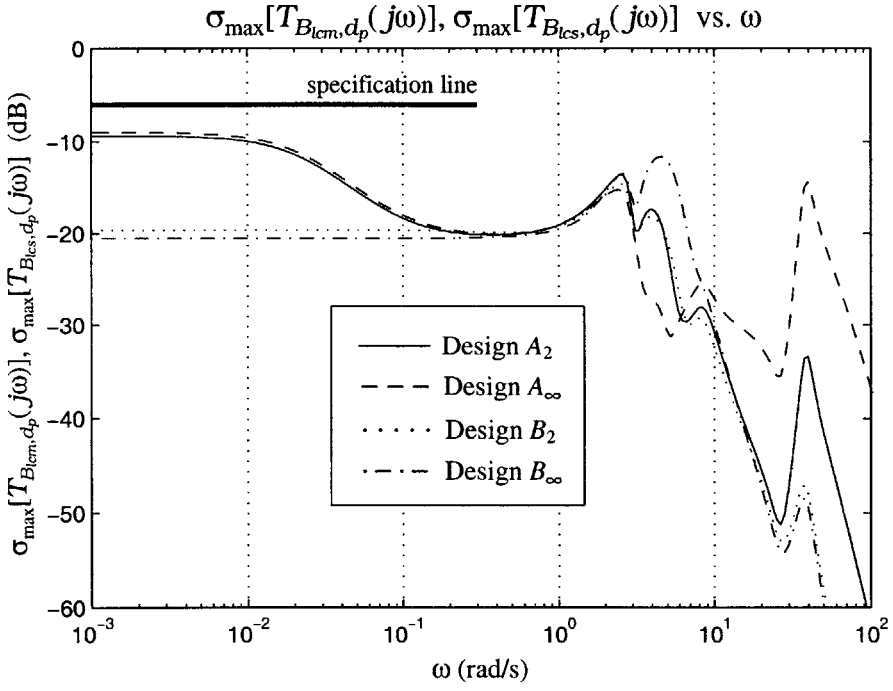

Figure 6-27: Maximum Singular Value of Transfer Function from d_p to B_{lcm}, B_{lcs}

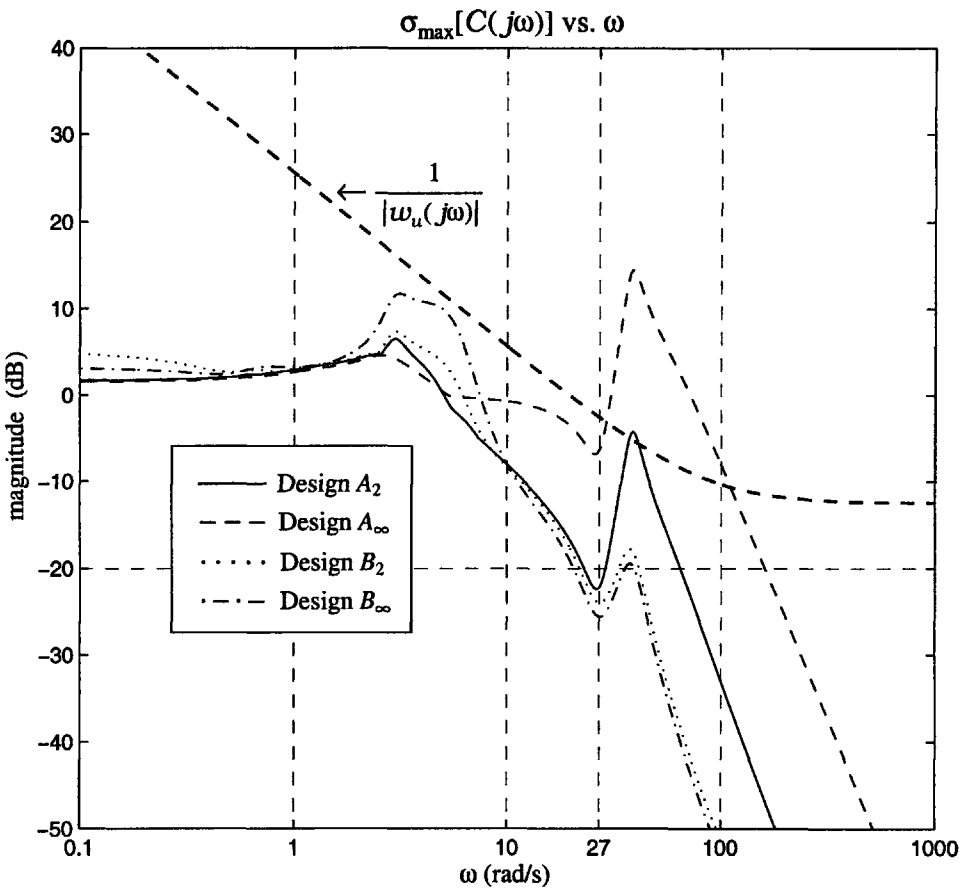

Figure 6-28: Maximum Singular Value of Complementary Sensitivity Function

The singular values for $T_{\theta_m,d_p}(j\omega)$ ($T_{\theta_s,d_p}(j\omega)$) in designs $\mathcal{A}_2$ and $\mathcal{B}_2$ show a large magnitude difference at frequencies below 0.3 rad/s, with relatively constant gains around -27 and -12.5 dB respectively. The responses then converge at around 2 rad/s before peaking at near 3 rad/s and rolling off. Designs $\mathcal{A}_\infty$ and $\mathcal{B}_\infty$ show the same large magnitude difference over the lower frequency range as the $\mathcal{H}_2$ designs. Below 0.3 rad/s, the gain in design $\mathcal{A}_\infty$ is nearly -30 dB, whereas that in design $\mathcal{B}_\infty$ is just slightly larger than that in design $\mathcal{B}_2$. The two $\mathcal{H}_\infty$ responses then converge with the $\mathcal{H}_2$ responses, as they peak at around 3 rad/s and roll off. As with Δx, ordering the designs according to the magnitude of $\sigma_{\max}[T_{\theta_m,d_p}(j\omega)]$ ($\sigma_{\max}[T_{\theta_s,d_p}(j\omega)]$) corresponds exactly to the ordering produced by comparing the pitch angle RMS values. In all of the designs, the response of $\sigma_{\max}[T_{\theta_m,d_p}(j\omega)]$ ($\sigma_{\max}[T_{\theta_s,d_p}(j\omega)]$) meets specification (S.8).

The responses of $\sigma_{\max}[T_{\Delta z,d_p}(j\omega)]$ in designs $\mathcal{A}_2$ and $\mathcal{B}_2$ remain relatively flat over frequencies below 0.2 and 0.01 rad/s respectively, at which points each begins slowly sloping

downwards until around 1 rad/s. In the flat regions of the responses, the gains in designs $\mathcal{A}_2$ and $\mathcal{B}_2$ are very close, at around -15 and -14 dB respectively. As the responses begin increasing at around 1 rad/s, they eventually converge, peaking once at between 2 and 3 rad/s, and again at around 4 rad/s, before rolling off. In design $\mathcal{A}_\infty$, $\sigma_{\max}[T_{\Delta z,d_p}(\jmath\omega)]$ remains relatively constant at around -11 dB until the frequency of 0.01 rad/s, at which point the response begins decreasing sharply, eventually reaching a negative gain of nearly -40 dB. At around 0.9 rad/s, this response then begins to increase, peaking twice at around the same frequencies of the $\mathcal{H}_2$ response peaks, but with a smaller magnitude. The response of $\sigma_{\max}[T_{\Delta z,d_p}(\jmath\omega)]$ in design $\mathcal{B}_\infty$ remains relatively flat around -8 dB until around 1 rad/s. This response then slopes slightly downward before peaking twice at around the same two frequencies as in the other designs, but with a larger gain. Consistent with the singular value magnitudes in Figure 6-24, the RMS value for Δz in design $\mathcal{A}_2$ is smaller than that in design $\mathcal{B}_2$, with design $\mathcal{B}_\infty$ producing by far the largest RMS. Design $\mathcal{A}_\infty$, however, produces the smallest RMS, just slightly smaller than that in design $\mathcal{A}_2$. This small RMS is likely due to the sharply negative gain in design $\mathcal{A}_\infty$ at frequencies around 0.9 rad/s. In designs $\mathcal{A}_2$, $\mathcal{A}_\infty$, and $\mathcal{B}_2$, the response of $\sigma_{\max}[T_{\Delta z,d_p}(\jmath\omega)]$ meets specification (S.9). In design $\mathcal{B}_\infty$, however, $\sigma_{\max}[T_{\Delta z,d_p}(\jmath\omega)]$ consistently shows a gain larger than the -10 dB constraint of this specification.

The singular values for $T_{\Sigma\dot{x},d_p}(\jmath\omega)$ show significant magnitude differences between the $\mathcal{A}$ and $\mathcal{B}$ designs over the lower frequencies. For frequencies below 0.3 rad/s, the response in design $\mathcal{B}_2$ has a relatively constant gain of around -13 dB. In design $\mathcal{A}_2$, however, the magnitude of $\sigma_{\max}[T_{\Sigma\dot{x},d_p}(\jmath\omega)]$ is as large as 14 dB up until 0.01 rad/s, and does not fall below the specification value of -5 dB until 0.2 rad/s. Design $\mathcal{B}_\infty$ shows by far the greatest magnitude reduction over the lower frequencies, with a negative gain of around -35 dB up until around 0.1 rad/s. The response of $\sigma_{\max}[T_{\Sigma\dot{x},d_p}(\jmath\omega)]$ in design $\mathcal{A}_\infty$ closely follows that in design $\mathcal{A}_2$ until around 3 rad/s, but with a slightly larger gain. All of the responses converge to peak at around 3 rad/s, before each peaks a second time and then rolls off. The relative gains in Figure 6-25 over the lower frequencies correspond exactly with the RMS values calculated for $\Sigma\dot{x}$. While designs $\mathcal{B}_2$ and $\mathcal{B}_\infty$ both meet specification (S.10) for process noise rejection, the large gains in designs $\mathcal{A}_2$ and $\mathcal{A}_\infty$ violate this specification.

In all of the designs, the singular values for $T_{\Theta_{cm},d_p}(\jmath\omega)$ ($T_{\Theta_{cs},d_p}(\jmath\omega)$) each show relatively constant gains of around -28 dB over frequencies below 1 rad/s. The largest magnitude

differences are seen as the singular values peak over the frequency range from 3 to 10 rad/s. It is these magnitude differences that best reflect the relative RMS values calculated for Θ_{cm} (Θ_{cs}). Note that in all of the designs, $\sigma_{\max}[T_{\Theta_{cm},d_p}(\jmath\omega)]$ ($\sigma_{\max}[T_{\Theta_{cs},d_p}(\jmath\omega)]$) shows a downward peak at around 27 rad/s, the frequency where sensor noise energy is greatest. $\sigma_{\max}[T_{\Theta_{cm},d_p}(\jmath\omega)]$ ($\sigma_{\max}[T_{\Theta_{cs},d_p}(\jmath\omega)]$) in all of the designs easily meets specification (S.14).

The responses of $\sigma_{\max}[T_{B_{lcm},d_p}(\jmath\omega)]$ ($\sigma_{\max}[T_{B_{lcs},d_p}(\jmath\omega)]$) in designs $\mathcal{A}_2$ and $\mathcal{B}_2$ differ significantly in magnitude at frequencies below 0.01 rad/s, with relatively constant gains of around -9 and -20 dB respectively. The response in design $\mathcal{A}_2$ then decreases to -20 dB, converging with that in design $\mathcal{B}_2$ at around 0.2 rad/s. After peaking at between 2 and 3 rad/s, the two responses then roll off, exhibiting several peaks and dips in the process. The response in design $\mathcal{A}_\infty$ has a similar shape to that in design $\mathcal{A}_2$, but shows a slightly larger gain over frequencies below 1 rad/s, a smaller gain over frequencies between 1 and 6 rad/s, and a much larger gain at frequencies above 6 rad/s. Similarly, the response of $\sigma_{\max}[T_{B_{lcm},d_p}(\jmath\omega)]$ ($\sigma_{\max}[T_{B_{lcs},d_p}(\jmath\omega)]$) in design $\mathcal{B}_\infty$ closely follows that in design $\mathcal{B}_2$, but shows a slightly smaller gain over all frequencies except those in the range from 2 to 11 rad/s. Consistent with the relative singular value gains over frequencies under 0.2 rad/s, the RMS values for B_{lcm} (B_{lcm}) in designs $\mathcal{B}_2$ and $\mathcal{B}_\infty$ are smaller than those in designs $\mathcal{A}_2$ and $\mathcal{A}_\infty$. While the RMS in design $\mathcal{B}_\infty$ is slightly larger than that in design $\mathcal{B}_2$, the RMS in design $\mathcal{A}_\infty$ is much larger than that in design $\mathcal{A}_2$. This large difference in RMS values between designs $\mathcal{A}_2$ and $\mathcal{A}_\infty$ disappears, however, when the sensor noise is omitted as an input. As with the collective control, $\sigma_{\max}[T_{B_{lcm},d_p}(\jmath\omega)]$ ($\sigma_{\max}[T_{B_{lcs},d_p}(\jmath\omega)]$) in all of the designs shows a downward peak at around 27 rad/s, with the peak in design $\mathcal{A}_\infty$ being substantially less pronounced than in the other designs. All of the designs meet specification (S.15) for process noise rejection.

6.2.2.2 Complementary Sensitivity Function

Figure 6-28 shows the maximum singular values of $C(\jmath\omega)$ for all four designs, together with the bounding function $1/|w_u(\jmath\omega)|$ in specification (S.16). The coordinates 27 rad/s and -20 dB are also marked for assessing the meeting of specification (S.11). In all of the designs, the response of $\sigma_{\max}[C(\jmath\omega)]$ shows a downward peak at 27 rad/s followed by an upward peak at around 40 rad/s. In designs $\mathcal{A}_2$, $\mathcal{B}_2$, and $\mathcal{B}_\infty$, the downward peaks fall beneath -20 dB, and hence specification (S.11) for sensor noise rejection is met. In design

$\mathcal{A}_\infty$, however, the magnitude of $\sigma_{\max}[C(j\omega)]$ at 27 rad/s dips no lower than -7 dB, and hence the sensor noise rejection requirement is not satisfied. Similar to the situation with specification (S.11), specification (S.16) for stability robustness is met by only the three designs $\mathcal{A}_2$, $\mathcal{B}_2$, and $\mathcal{B}_\infty$. Among these, the response in design $\mathcal{B}_\infty$ comes very close to the bounding function at frequencies between 2 and 7 rad/s, whereas that in design $\mathcal{A}_2$ actually peaks to touch the bounding function at around 40 rad/s. Design $\mathcal{A}_\infty$, which does not meet specification (S.16), shows a peak at 40 rad/s similar to that seen in design $\mathcal{A}_2$, but with a magnitude reaching over 14 dB. In this design, $\sigma_{\max}[C(j\omega)]$ violates the bounding function in specification (S.16) over frequencies from 30 to 100 rad/s.

6.2.3 Conclusions

Both of the $\mathcal{H}_2$ controller designs, $\mathcal{A}_2$ and $\mathcal{B}_2$, meet all of the specifications considered mandatory for acceptable design performance. The nature of the responses in each design, however, differ considerably. The two designs also vary in the extent to which they each meet (or do not meet) the specifications, both those mandatory and those desirable. These differences are often explainable in terms of variations in the output matrix and weighting functions used to construct the respective generalized plants.

In general, design $\mathcal{A}_2$ achieves superior performance in the regulated variables Δx, θ_m (θ_s), and Δz, while design $\mathcal{B}_2$ achieves superior performance in the regulated variable $\Sigma\dot{x}$. These performance differences are most pronounced in the stochastic simulations and wind-to-variable singular value plots. In design $\mathcal{A}_2$, $\Sigma\dot{x}$ violates specification (S.5) in the stochastic simulation, as well as specification (S.10) in the plot of $\sigma_{\max}[T_{\Sigma\dot{x},d_p}(j\omega)]$. This reduced performance of $\Sigma\dot{x}$ results from the omission of this variable as an output. Design $\mathcal{A}_2$ having only the three outputs Δx, $x_L - \Sigma x$, and $\Sigma\theta$, however, allows for more focused control on each of these variables' responses, hence explaining the improved performance seen in the variables Δx and θ_m (θ_s). While $x_L - \Sigma x$ is also among the outputs in design $\mathcal{A}_2$, the performance of this variable in this design is comparable to that in design $\mathcal{B}_2$. This result can be explained by comparing the penalties on $x_L - \Sigma x$ in the weighting matrices W_3. Table 5.4 shows that in design $\mathcal{A}_2$, the penalty on $x_L - \Sigma x$ is $2.5 \cdot 10^4$, whereas in design $\mathcal{B}_2$, this penalty is much larger at $4 \cdot 10^4$. The cyclic and collective controls in designs $\mathcal{A}_2$ and $\mathcal{B}_2$ show small to modest magnitude differences, with design $\mathcal{A}_2$ having a larger cyclic, and design $\mathcal{B}_2$ a larger collective. As seen in Figure 6-28, while both designs meet

specification (S.16) for stability robustness, $\sigma_{\max}[C(j\omega)]$ in design $\mathcal{A}_2$ peaks much higher than in design $\mathcal{B}_2$ at around 40 rad/s, actually touching the bounding function in this specification. The large peak in design $\mathcal{A}_2$ can be explained in part by the selection of the weighting functions $w_2(s)$. Table 5.2 shows that the linear term of this function in design $\mathcal{A}_2$ is smaller than that in design $\mathcal{B}_2$. Hence $1/|w_2(j\omega)|$ in the former design both dips lower (at 27 rad/s) and peaks higher (at around 40 rad/s) than that same function in the latter. The selection of a larger peaking function in design $\mathcal{A}_2$ was necessary to ensure that $\sigma_{\max}[C(j\omega)]$ achieve the sensor noise rejection requirement. Figure 6-28 shows that both designs do indeed meet specification (S.11) for sensor noise rejection. The success of meeting this specification is also seen by comparing the RMS values in Tables 6.1 and 6.2. In each design, the difference between output RMS values with the sensor noise input and without it, is negligible.

Each $\mathcal{H}_\infty$ design differs significantly from its corresponding $\mathcal{H}_2$ design, but these differences are difficult to predict, and do not exhibit consistent characteristics in the two cases. In design $\mathcal{A}_\infty$, the TLHS generally responds with a larger cyclic but smaller collective than in $\mathcal{A}_2$. In the deterministic time domain simulations to (IC.2), a much larger cyclic response in design $\mathcal{A}_\infty$ produces more magnitude reduction and significantly shorter settling times than those seen in the corresponding $\mathcal{H}_2$ design. In the stochastic simulations, in which the collective response in design $\mathcal{A}_\infty$ is significantly smaller than that in design $\mathcal{A}_2$, design $\mathcal{A}_\infty$ achieves greater magnitude reduction in the variables Δx, θ_m (θ_s), and Δz, but slightly less magnitude reduction in $x_L - \Sigma x$ and $\Sigma \dot{x}$. Hence, as with design $\mathcal{A}_2$, $\Sigma \dot{x}$ in design $\mathcal{A}_\infty$ violates the time domain specification (S.5) as well as the frequency domain specification (S.10). As seen in Figure 6-28, design $\mathcal{A}_\infty$ also fails to meet specifications (S.11) for sensor noise rejection and (S.16) for stability robustness. In design $\mathcal{B}_\infty$, the TLHS uses a much larger collective and slightly larger cyclic control than in design $\mathcal{B}_2$. In the deterministic simulations, the larger controls in design $\mathcal{B}_\infty$ occasionally produce slightly faster responses in the regulated variables than in design $\mathcal{B}_2$, but in every case, these variables in the former design show larger magnitudes than in the latter. In the stochastic simulations, design $\mathcal{B}_\infty$ achieves much improved performance in the variables Δx, $x_L - \Sigma x$, and $\Sigma \dot{x}$, but worse performance in the variables θ_m (θ_s) and Δz, than design $\mathcal{B}_2$. As a result, this $\mathcal{H}_\infty$ design violates the time domain specification (S.3) on θ_m (θ_s), as well as both the time and frequency domain specifications (S.4) and (S.9) on Δz. In addition, the large collective

response in design $\mathcal{B}_\infty$ during the stochastic simulation far exceeds the 10° magnitude constraint of specification (S.12). As seen in Figure 6-28, $\sigma_{\max}[C(j\omega)]$ in design $\mathcal{B}_\infty$ meets both specification (S.11) for sensor noise rejection and (S.16) for stability robustness. This $\mathcal{A}_\infty$ design actually slightly betters design $\mathcal{B}_2$ in achieving sensor noise rejection, but achieves less in the way of stability robustness, as $\sigma_{\max}[C(j\omega)]$ comes very close to the bounding function $1/|w_u(j\omega)|$ over frequencies from 2 to 7 rad/s.

6.3 $\mathcal{H}_\infty$ Designs

For designs $\mathcal{C}_\infty$ and $\mathcal{D}_\infty$, the selected outputs are Δx, $x_L - \Sigma x$, and $\Sigma\theta$, with design $\mathcal{D}_\infty$ including the additional output $\Sigma\dot{x}$. The weighting functions for these designs are listed in Tables 5.5 and 5.6. The order and size of these weighting functions determine the order of the generalized plant, and hence of the corresponding $\mathcal{H}_\infty$ or $\mathcal{H}_2$ compensator. Thus for designs $\mathcal{C}_\infty$ and $\mathcal{C}_2$, the controllers are of order 23, whereas for designs $\mathcal{D}_\infty$ and $\mathcal{D}_2$, the compensator order is 26.

Recall from section 4.3.3, that $\mathcal{H}_\infty$ synthesis involves constructing the controller K_∞ in (4.18), with γ equal to the infimum over all γ such that conditions (C.1)–(C.5) hold. In practice, $\gamma_{\min}$ is found to within some prespecified tolerance, which in this thesis is chosen as 0.01. As discussed in section 4.4.2.1 on loop shaping, it is also desirable to construct each generalized plant in $\mathcal{H}_\infty$ design such that $\gamma \leq 1$. The values ultimately arrived at for γ in designs $\mathcal{C}_\infty$ and $\mathcal{D}_\infty$ are 0.98 and 0.95 respectively. Each corresponding $\mathcal{H}_2$ controller results from allowing γ in the corresponding $\mathcal{H}_\infty$ design to approach infinity. In practice, the controllers $\mathcal{C}_2$ and $\mathcal{D}_2$ are constructed by letting γ equal 10^4.

6.3.1 Time Domain

6.3.1.1 Transient Response

Figures 6-29 to 6-37 show the transient response of the TLHS regulated variables and controls to the two initial conditions (IC.1) and (IC.2) given in section 5.2.2.1. Recall that (IC.1) affects only the SM plant, and hence only Δx, $\Delta\theta$, and ΔB_{lc} show non-zero responses. Similarly, (IC.2) affects only the ASM plant, inducing responses in the variables $x_L - \Sigma x$, $\Sigma\theta$, Δz, $\Sigma\dot{x}$, ΣB_{lc}, and $\Delta\Theta_c$.

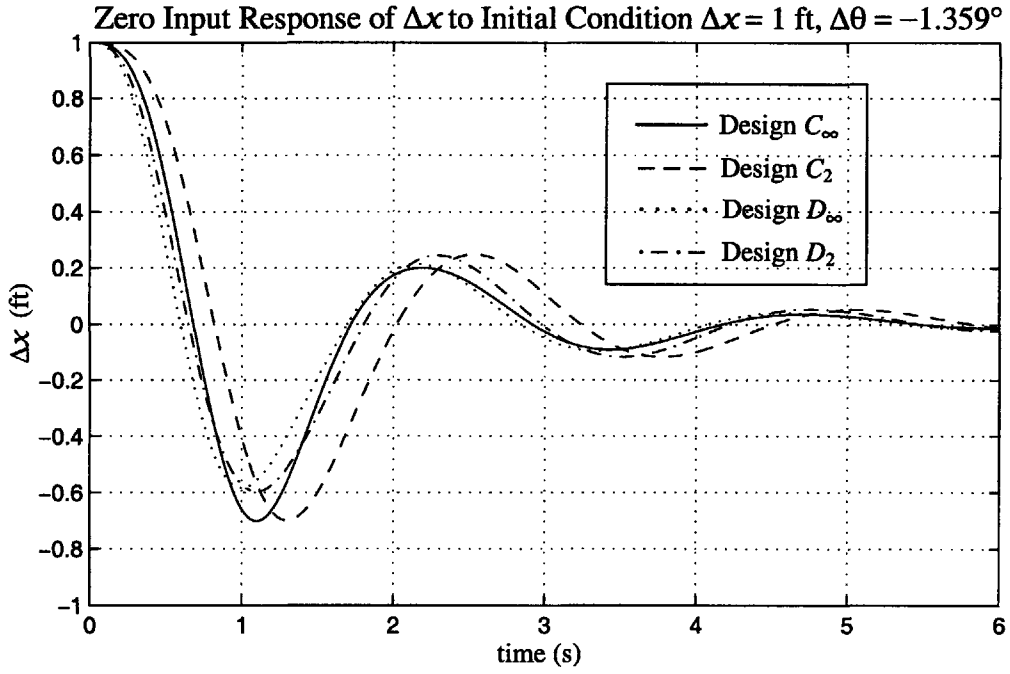

Figure 6-29: Transient Response of Δx to Initial Condition $\Delta x = 1$ ft, $\Delta\theta = -1.359°$

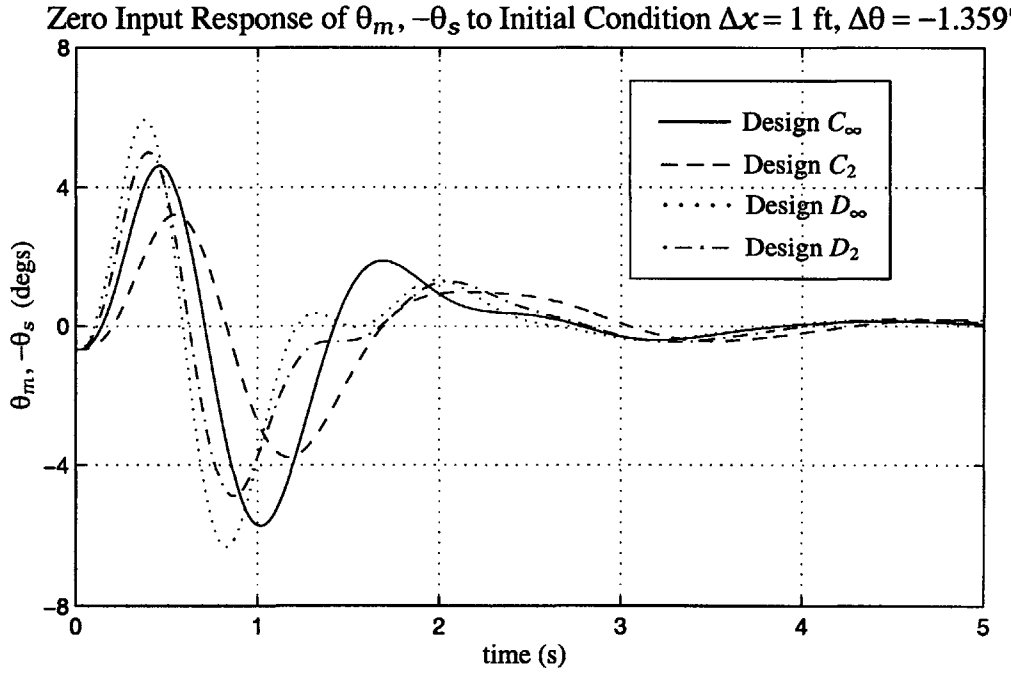

Figure 6-30: Transient Response of $\theta_m, -\theta_s$ to Initial Condition $\Delta x = 1$ ft, $\Delta\theta = -1.359°$

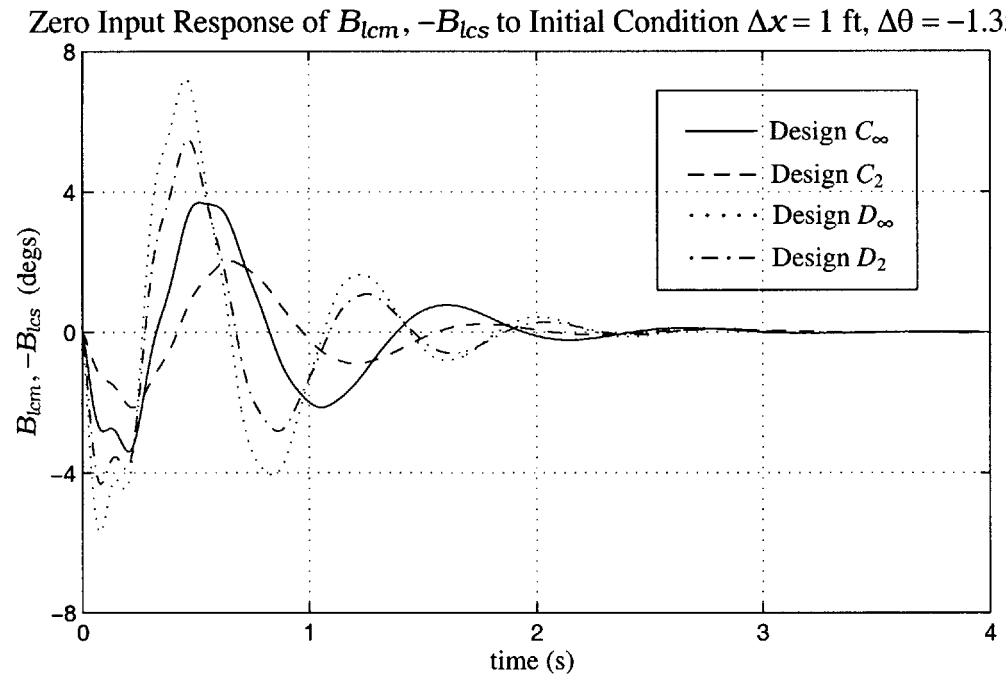

Figure 6-31: Transient Response of B_{lcm}, $-B_{lcs}$ to Initial Condition $\Delta x = 1$ft, $\Delta\theta = -1.359°$

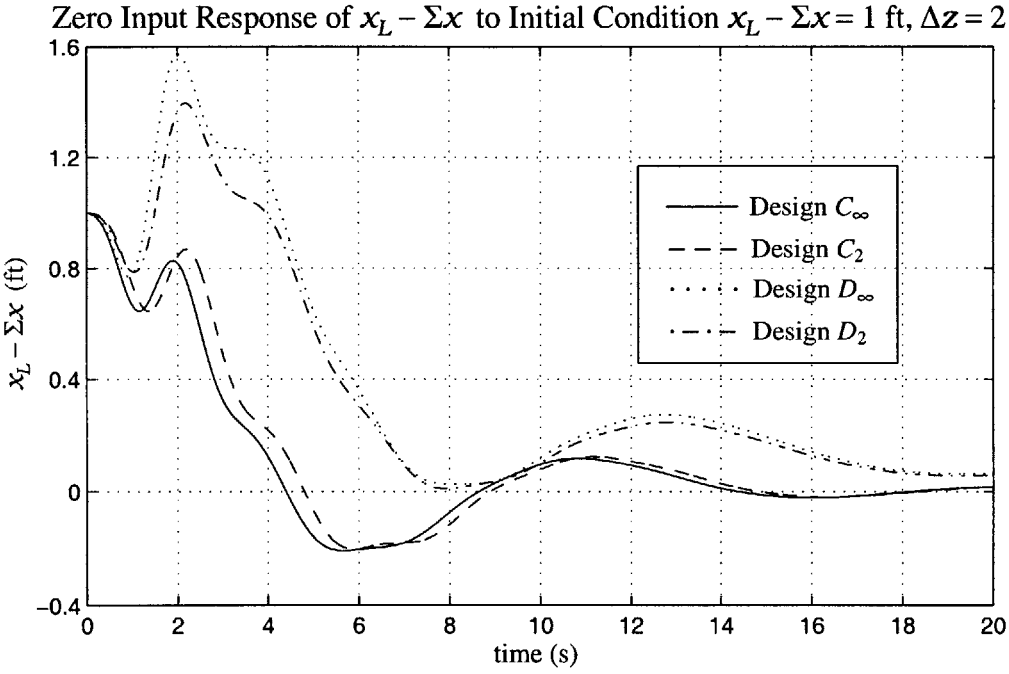

Figure 6-32: Transient Response of $x_L - \Sigma x$ to Initial Condition $x_L - \Sigma x = 1$ ft, $\Delta z = 2$ ft

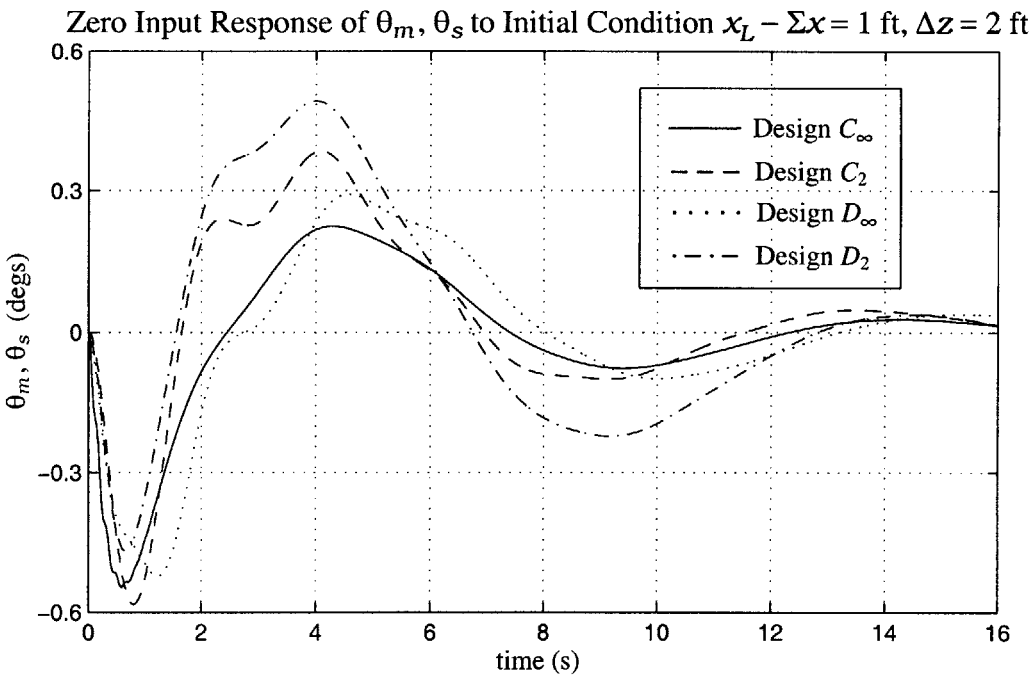

Figure 6-33: Transient Response of θ_m, θ_s to Initial Condition $x_L - \Sigma x = 1$ ft, $\Delta z = 2$ ft

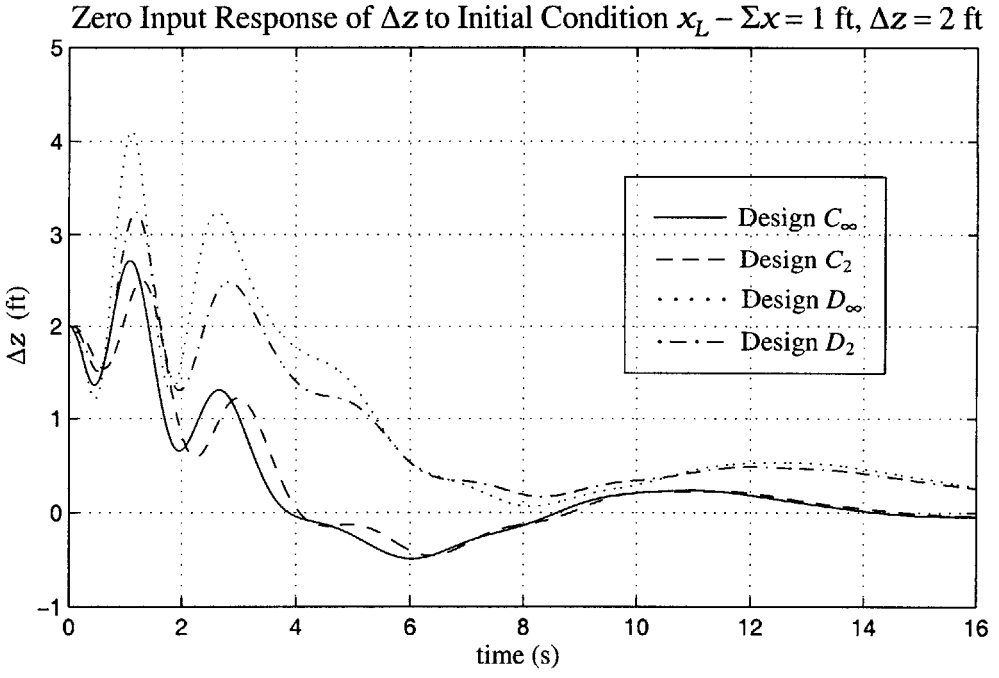

Figure 6-34: Transient Response of Δz to Initial Condition $x_L - \Sigma x = 1$ ft, $\Delta z = 2$ ft

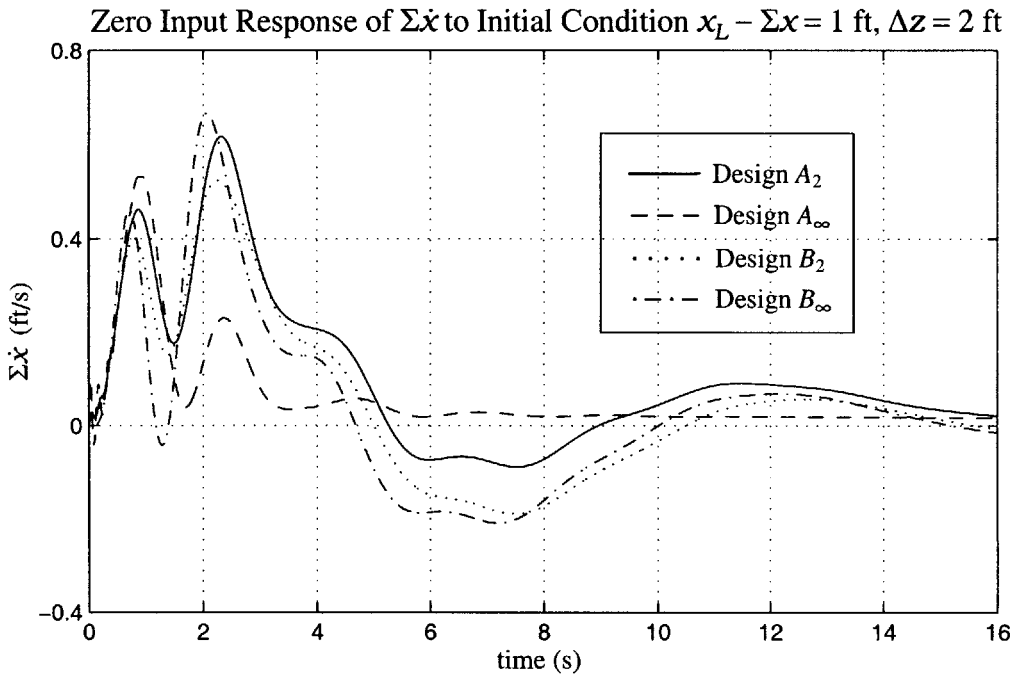

Figure 6-35: Transient Response of $\Sigma\dot{x}$ to Initial Condition $x_L - \Sigma x = 1$ ft, $\Delta z = 2$ ft

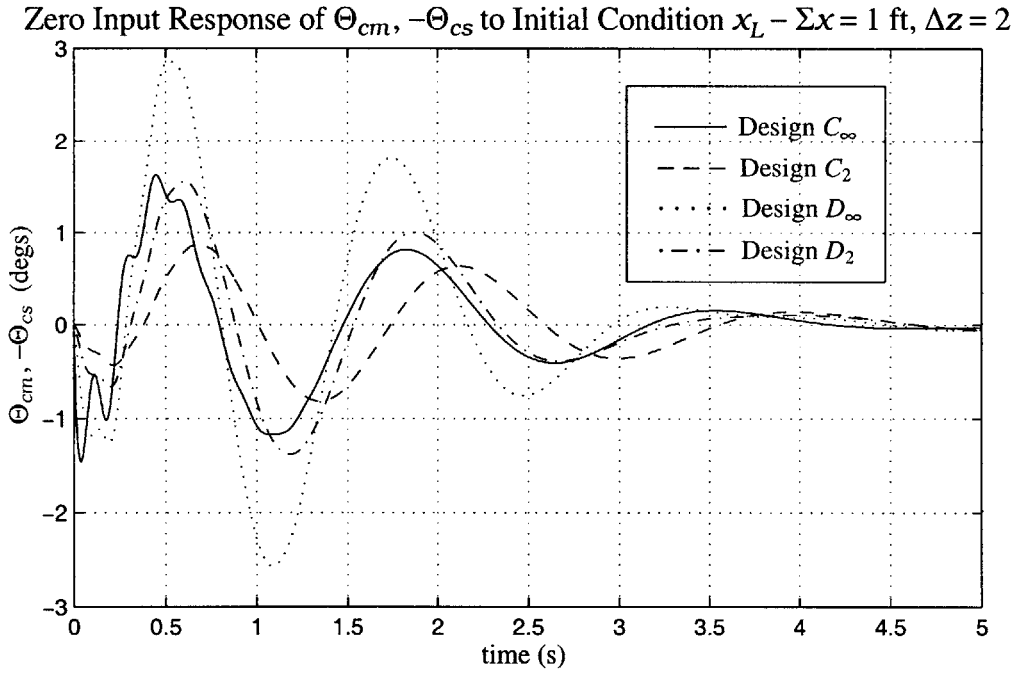

Figure 6-36: Transient Response of Θ_{cm}, $-\Theta_{cs}$ to Initial Condition $x_L - \Sigma x = 1$ ft, $\Delta z = 2$ ft

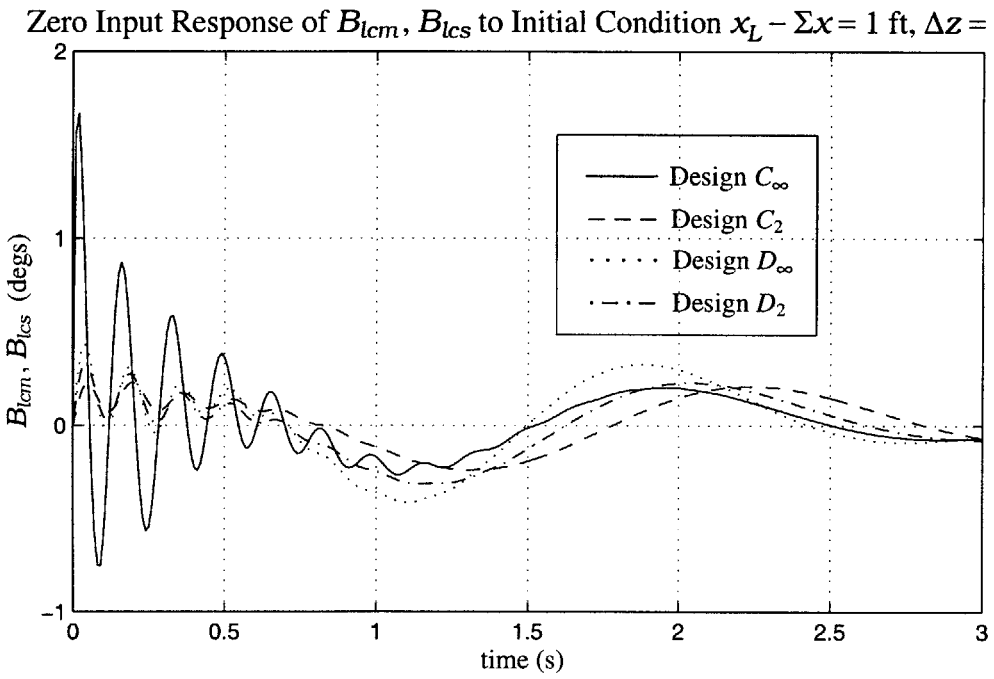

Figure 6-37: Transient Response of B_{lcm}, B_{lcs} to Initial Condition $x_L - \Sigma x = 1\,\text{ft}$, $\Delta z = 2\,\text{ft}$

(IC.1)

Figures 6-29 to 6-31 show the TLHS response to (IC.1). In all of the designs, the response of Δx oscillates several times before settling into equilibrium in around 6 seconds. The response in design $\mathcal{D}_\infty$ is initially faster than that in design $\mathcal{C}_\infty$, with a smaller undershoot of equilibrium. After around 2 seconds, however, the two $\mathcal{H}_\infty$ responses are nearly identical. The $\mathcal{H}_2$ designs produce responses in Δx that closely resemble those in the corresponding $\mathcal{H}_\infty$ designs, but with a lower oscillation frequency and slightly larger amplitude. The frequency difference is most pronounced between designs $\mathcal{C}_\infty$ and $\mathcal{C}_2$. In all of the designs, specification (S.1) is easily satisfied.

The pitch angle response to (IC.1) shows some high frequency oscillation before settling into equilibrium in around 5 seconds. The response in design $\mathcal{D}_\infty$ is of a higher frequency than that in design $\mathcal{C}_\infty$, and initially oscillates with a larger amplitude. After around 1 second, however, design $\mathcal{D}_\infty$ generally shows greater magnitude reduction than design $\mathcal{C}_\infty$. As with Δx, the pitch angle responses in the $\mathcal{H}_2$ designs resemble those in the corresponding $\mathcal{H}_\infty$ designs, but with a lower oscillation frequency, and with this frequency difference most pronounced between designs $\mathcal{C}_\infty$ and $\mathcal{C}_2$. The $\mathcal{H}_2$ designs show smaller oscillation amplitudes

than the corresponding $\mathcal{H}_\infty$ designs in the first 2 seconds of the response, but show slightly larger oscillation amplitudes afterwards. In all of the designs, the response of θ_m $(-\theta_s)$ stays within the bounds of specification (S.3).

In all of the designs, the cyclic control responds very rapidly, reaching equilibrium in around 3 seconds. Design $\mathcal{D}_\infty$ shows a larger amplitude and higher frequency than design $\mathcal{C}_\infty$. The responses of B_{lcm} $(-B_{lcs})$ in the $\mathcal{H}_2$ designs are lower in frequency and smaller in amplitude than those in the corresponding $\mathcal{H}_\infty$ designs, with the frequency difference between designs $\mathcal{C}_\infty$ and $\mathcal{C}_2$ being far more significant than that between designs $\mathcal{D}_\infty$ and $\mathcal{D}_2$. In all of the designs, the cyclic control response meets specification (S.13).

(IC.2)

Figures 6-32 to 6-37 show the TLHS response to (IC.2). The responses of $x_L - \Sigma x$ in designs $\mathcal{C}_\infty$ and $\mathcal{D}_\infty$ are similar in shape, with that in design $\mathcal{C}_\infty$ achieving significantly greater magnitude reduction. Each of these $\mathcal{H}_\infty$ responses settles into equilibrium in around 20 seconds. The response of $x_L - \Sigma x$ in design $\mathcal{C}_2$ is nearly identical to that in design $\mathcal{C}_\infty$, with the main difference being a time delay of about 0.5 seconds present in the former design. Similarly, the response of $x_L - \Sigma x$ in design $\mathcal{D}_2$ is very close to that in design $\mathcal{D}_\infty$, with the main difference being a slightly greater magnitude reduction in the former design. In all of the designs, the response of $x_L - \Sigma x$ meets specification (S.2).

The pitch angle response to (IC.2) shows some low frequency small amplitude oscillation before settling into equilibrium in around 16 seconds. After initial undershoots exhibited in between 0 and 2 seconds, the $\mathcal{H}_\infty$ responses oscillate more slowly and with smaller amplitudes than the $\mathcal{H}_2$ responses. In this same time period, θ_m (θ_s) in design $\mathcal{C}_\infty$ responds more quickly and with a slightly smaller amplitude than in design $\mathcal{D}_\infty$. Similarly, the response of θ_m (θ_s) in this period is smaller in design $\mathcal{C}_2$ than in design $\mathcal{D}_2$. During the initial seconds of the response, where the undershoots are occur, the pitch angle behavior differs substantially from that later on, with design $\mathcal{C}_\infty$ responding the most quickly and with a larger magnitude than design $\mathcal{D}_\infty$, and design $\mathcal{D}_2$ showing the smallest magnitude among all of the designs. In all of the designs, θ_m (θ_s) remains within $\pm 0.6°$, and hence specification (S.3) is easily satisfied.

The response of Δz to (IC.2) bears many of the characteristics seen in the response of the load deviation from center. In each design, Δz shows several small amplitude oscillations

before gradually achieving equilibrium in around 16 seconds. Design $\mathcal{C}_\infty$ shows significantly greater magnitude reduction and a slightly shorter settling time than design $\mathcal{D}_\infty$. Each $\mathcal{H}_2$ response closely follows its corresponding $\mathcal{H}_\infty$ response, with the main differences being a time lag present in design $\mathcal{C}_2$, and a magnitude reduction seen in design $\mathcal{D}_2$, both similar to those observed in the response of $x_L - \Sigma x$. In all of the designs, the response of Δz easily stays within the bounds of specification (S.4).

In all of the designs, the response of $\Sigma\dot{x}$ remains small, never exceeding a magnitude of 0.7 ft/s. In designs $\mathcal{C}_\infty$ and $\mathcal{D}_\infty$, $\Sigma\dot{x}$ shows some small amplitude oscillation before settling into equilibrium in around 25 seconds. The responses in these two designs are similar in shape, with that in design $\mathcal{D}_\infty$ showing a larger oscillation amplitude and a slightly shorter settling time. In the first 5 seconds of the response, the $\mathcal{H}_2$ designs produce smaller amplitude oscillations than the corresponding $\mathcal{H}_\infty$ designs. After this initial period, however, the $\mathcal{H}_2$ responses show the largest magnitudes and longest settlings times, with the response in design $\mathcal{C}_2$ taking an especially long time to reach equilibrium. In all of the designs, the small magnitude response of $\Sigma\dot{x}$ easily meets specification (S.5).

The collective control response to (IC.2) shows several oscillations of decreasing amplitude before settling into equilibrium in around 4 seconds. In designs $\mathcal{C}_\infty$ and $\mathcal{D}_\infty$, the responses are similar in shape, with design $\mathcal{D}_\infty$ producing a much larger amplitude and slightly higher frequency. Both designs also show some high frequency dips and peaks superimposed with the response's first oscillation. These higher frequency dips and peaks die out significantly more slowly in design $\mathcal{C}_\infty$ than in design $\mathcal{D}_\infty$. Each $\mathcal{H}_2$ response is smaller in amplitude and lower in frequency than its corresponding $\mathcal{H}_\infty$ response. In designs $\mathcal{C}_\infty$ and $\mathcal{C}_2$, the more substantial difference is in frequency, whereas in designs $\mathcal{D}_\infty$ and $\mathcal{D}_2$, the difference in amplitude is the more pronounced. In all of the designs, the response of Θ_{cm} $(-\Theta_{cs})$ stays within the bounds of specification (S.12).

In all of the designs, the cyclic control response is characterized by high frequency rapidly decaying oscillations superimposed with a lower frequency more slowly decaying oscillation. The lower frequency components among the four designs are close in both amplitude and frequency, with design $\mathcal{D}_\infty$ producing the largest amplitude, and design $\mathcal{C}_\infty$ the smallest. Design $\mathcal{D}_\infty$ also produces the highest frequency among the four lower frequency components, followed by design $\mathcal{C}_\infty$, and then by the two $\mathcal{H}_2$ designs. The higher frequency components of the four responses are also close in frequency, but the amplitude in design $\mathcal{C}_\infty$ far exceeds

that in the other designs, initially reaching around 1.5°. In the other three designs, the amplitude of the higher frequency component never exceeds 0.25°, with the $\mathcal{H}_2$ designs producing the smallest amplitudes. In spite of the large initial magnitude differences, B_{lcm} (B_{lcs}) in all of the designs settles into equilibrium in around 3 seconds. The magnitude of this cyclic response easily meets specification (S.13).

6.3.1.2 Stochastic Response

For each of the controller designs, the closed loop response is observed to the stochastic inputs $d_p(t)$ and $d_s(t)$, generated as described in section 5.2.1 of chapter 5. These process and sensor noises are the same as those used in the stochastic simulations of the $\mathcal{H}_2$ designs. In addition to stochastic plots of the TLHS variables and controls, steady state RMS values are generated for these outputs, calculated from the state covariance matrices. Table 6.3 lists the RMS values when only the process noise $d_p(t)$ is included as an input. It is from this table that the scaling factors r_i for each sensor noise $d_{si}(t)$ are taken. Table 6.4 then lists the RMS values when the input includes both the process and sensor noises.

Figures 6-38 to 6-46 show the stochastic response of the TLHS to the inputs $d_p(t)$ and $d_s(t)$. For the variable Δx, the responses in all of the designs are similar in shape, but differ in magnitude. Design $\mathcal{D}_\infty$ shows slightly more magnitude reduction than design $\mathcal{C}_\infty$. This magnitude difference is reflected in the RMS values for these two designs, of 1.20 and 1.54 respectively. The magnitude of Δx in each $\mathcal{H}_2$ design is larger than in its corresponding $\mathcal{H}_\infty$ design, with the difference most pronounced between designs $\mathcal{C}_\infty$ and $\mathcal{C}_2$. Again, this result is consistent with the RMS values calculated for designs $\mathcal{C}_2$ and $\mathcal{D}_2$, of 2.16 and 1.40

Variables/ Controls	**Design**			
	$\mathcal{C}_\infty$	$\mathcal{D}_\infty$	$\mathcal{C}_2$	$\mathcal{D}_2$
Δx	1.5374	1.2028	2.1557	1.3953
$x_L - \Sigma x$	1.4810	1.1685	2.1258	1.6162
θ_m, θ_s	1.6131	3.3995	2.3973	2.8309
Δz	2.3614	5.3309	2.1568	3.2043
$\Sigma \dot{x}$	19.477	1.5979	16.195	3.5619
Θ_{cm}, Θ_{cs}	1.3799	2.8341	1.1548	1.7072
B_{lcm}, B_{lcs}	1.9815	1.5287	1.9617	1.6047
$\Sigma\theta$	0.5917	3.1516	1.3702	2.4150

Table 6.3: RMS Values of Variables and Controls with Input $d_p(t)$

Variables/ Controls	Design			
	$\mathcal{C}_\infty$	$\mathcal{D}_\infty$	$\mathcal{C}_2$	$\mathcal{D}_2$
Δx	1.5390	1.2039	2.1582	1.3966
$x_L - \Sigma x$	1.4813	1.1735	2.1267	1.6202
θ_m, θ_s	1.7346	3.4638	2.4687	2.8950
Δz	2.3650	5.3780	2.1654	3.2281
$\Sigma \dot{x}$	19.477	1.6030	16.195	3.5639
Θ_{cm}, Θ_{cs}	1.4214	3.3417	1.1829	1.8579
B_{lcm}, B_{lcs}	2.1048	1.8567	2.0113	1.8366
$\Sigma\theta$	0.5926	3.1527	1.3716	2.4165

Table 6.4: RMS Values of Variables and Controls with Inputs $d_p(t)$ and $d_s(t)$

respectively. In designs $\mathcal{C}_\infty$, $\mathcal{D}_\infty$, and $\mathcal{D}_2$, the response of Δx meets the 6 ft magnitude constraint of specification (S.1). In design $\mathcal{C}_2$, however, Δx becomes as large as 8 ft, and hence specification (S.1) is violated.

As with Δx, the responses of the load deviation from center are similar in shape, but differ in magnitude. The oscillations in design $\mathcal{D}_\infty$ are generally smaller in amplitude than those in design $\mathcal{C}_\infty$. This magnitude difference is reflected in the RMS values for these two designs, of 1.17 and 1.48 respectively. Also similar to Δx, the responses of $x_L - \Sigma x$ show less magnitude reduction in the $\mathcal{H}_2$ designs than in the corresponding $\mathcal{H}_\infty$ designs. With $x_L - \Sigma x$, however, the magnitude difference between designs $\mathcal{D}_\infty$ and $\mathcal{D}_2$ is comparable to that between designs $\mathcal{C}_\infty$ and $\mathcal{C}_2$. The RMS values for the designs $\mathcal{C}_2$ and $\mathcal{D}_2$ are 2.13 and 1.62 respectively. In all of the designs, the load deviation from center remains within the bounds of specification (S.2).

The pitch angle responses in designs $\mathcal{C}_\infty$ and $\mathcal{D}_\infty$ show significant differences both in shape and in magnitude. In design $\mathcal{C}_\infty$, θ_m and θ_s exhibit uniformly high frequency oscillations never exceeding a magnitude of 6°. In design $\mathcal{D}_\infty$, while this same pattern of high frequency oscillations is present, it is superimposed with an additional lower frequency, but comparable amplitude oscillation. This lower frequency component of the design $\mathcal{D}_\infty$ response develops slowly, and hence Figures 6-40 and 6-41 show θ_m and θ_s over two separate time intervals. As each figure shows, the additional lower frequency component creates pitch angle magnitudes repeatedly near or equal to 9°, and hence much larger than those in seen design $\mathcal{C}_\infty$. This magnitude difference between designs $\mathcal{C}_\infty$ and $\mathcal{D}_\infty$ is aptly reflected in the RMS values calculated for these two designs, of 1.73 and 3.46 respectively. The $\mathcal{H}_2$

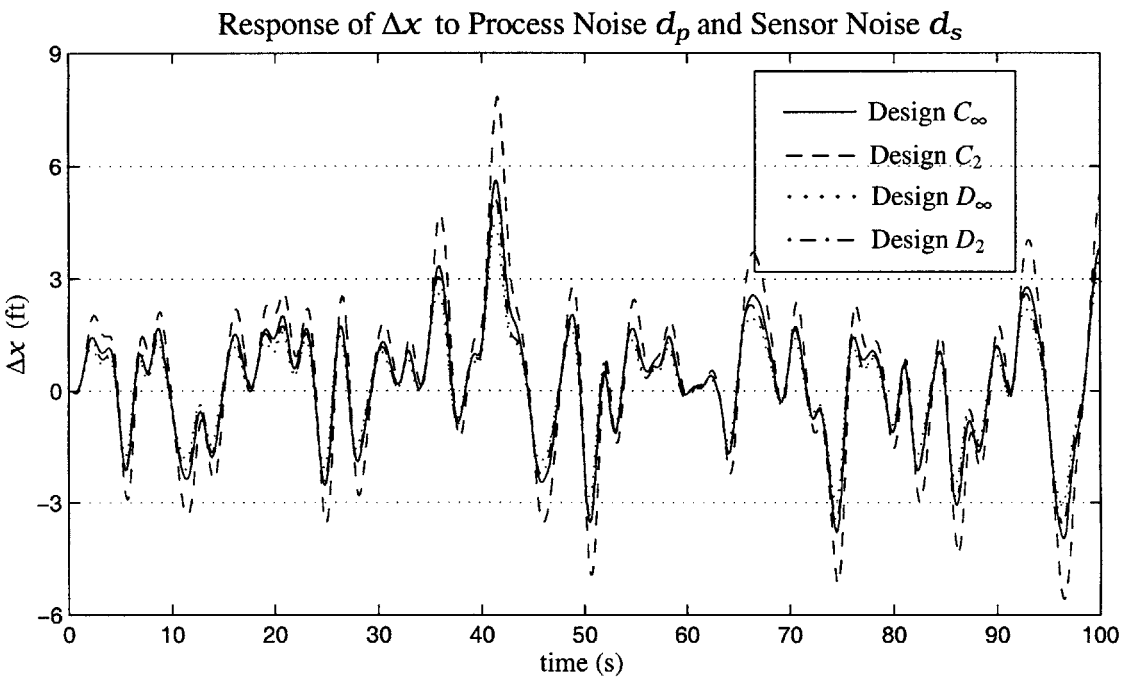

Figure 6-38: Stochastic Response of Δx to Process Noise d_p and Sensor Noise d_s

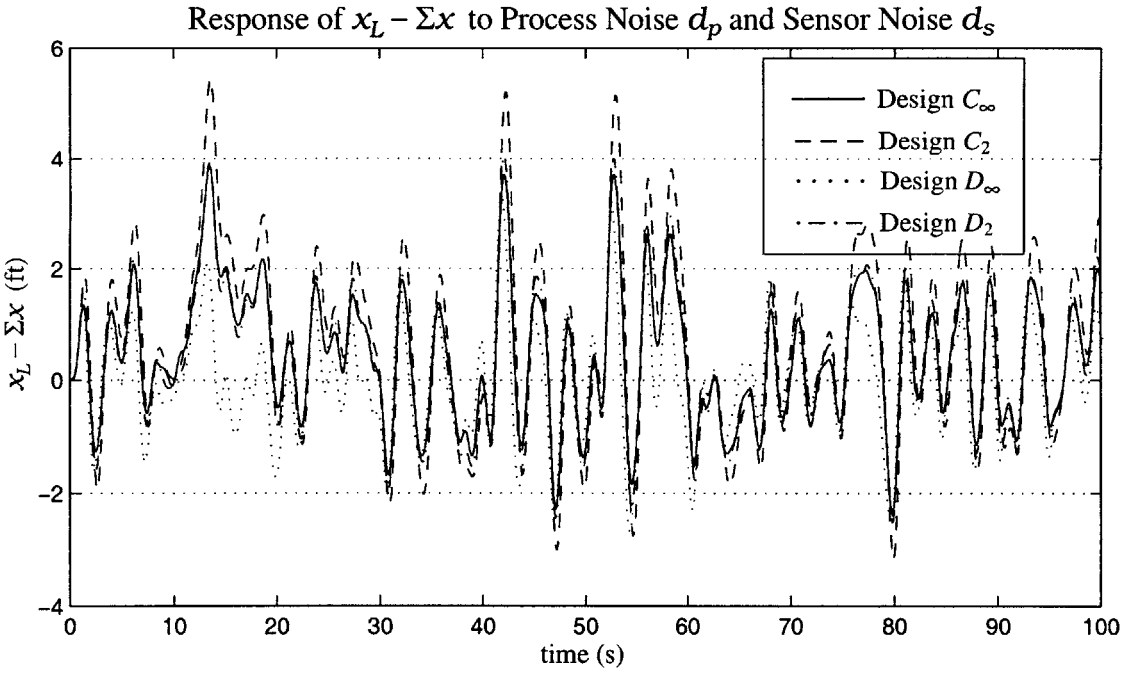

Figure 6-39: Stochastic Response of $x_L - \Sigma x$ to Process Noise d_p and Sensor Noise d_s

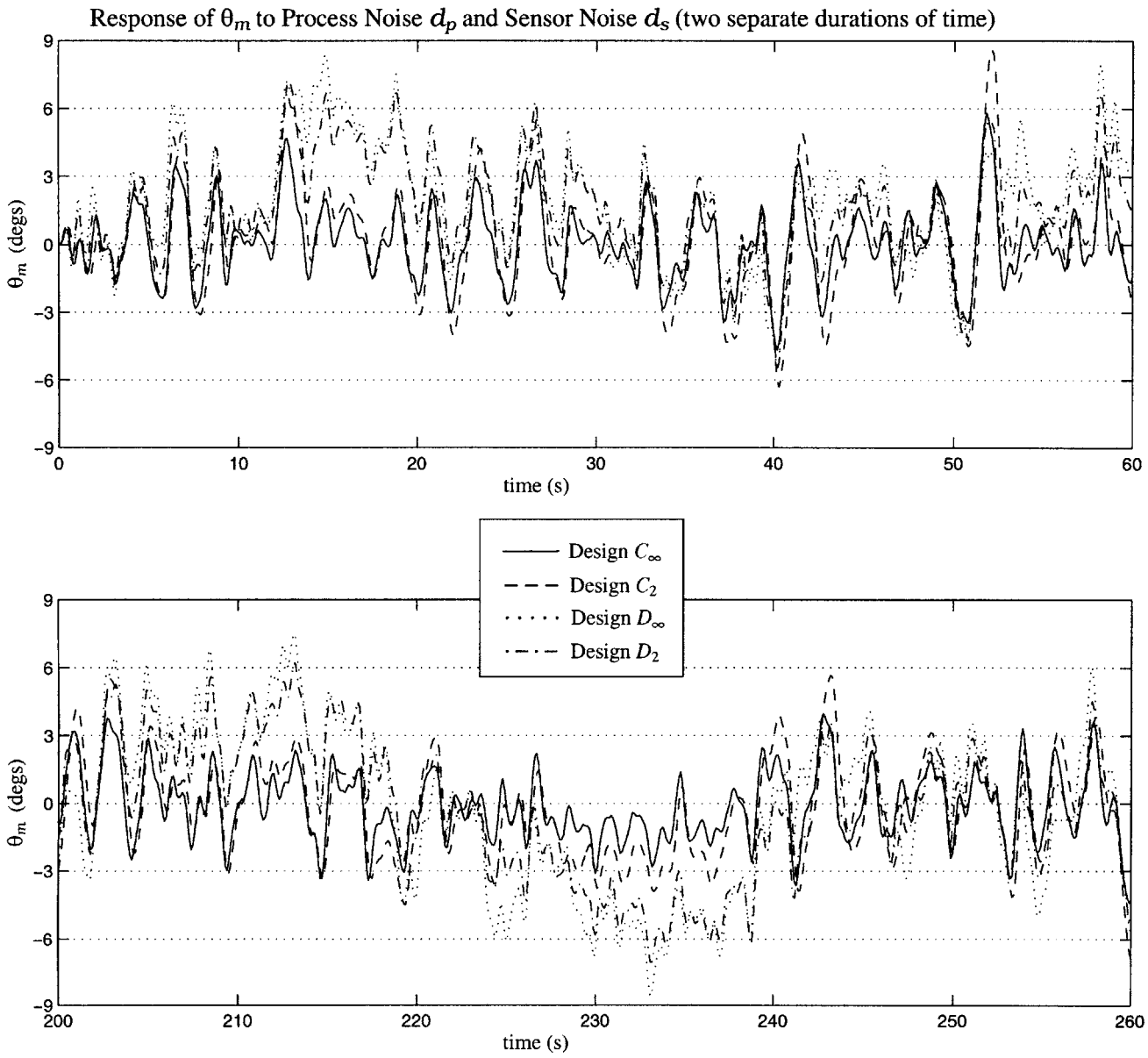

Figure 6-40: Stochastic Response of θ_m to Process Noise d_p and Sensor Noise d_s

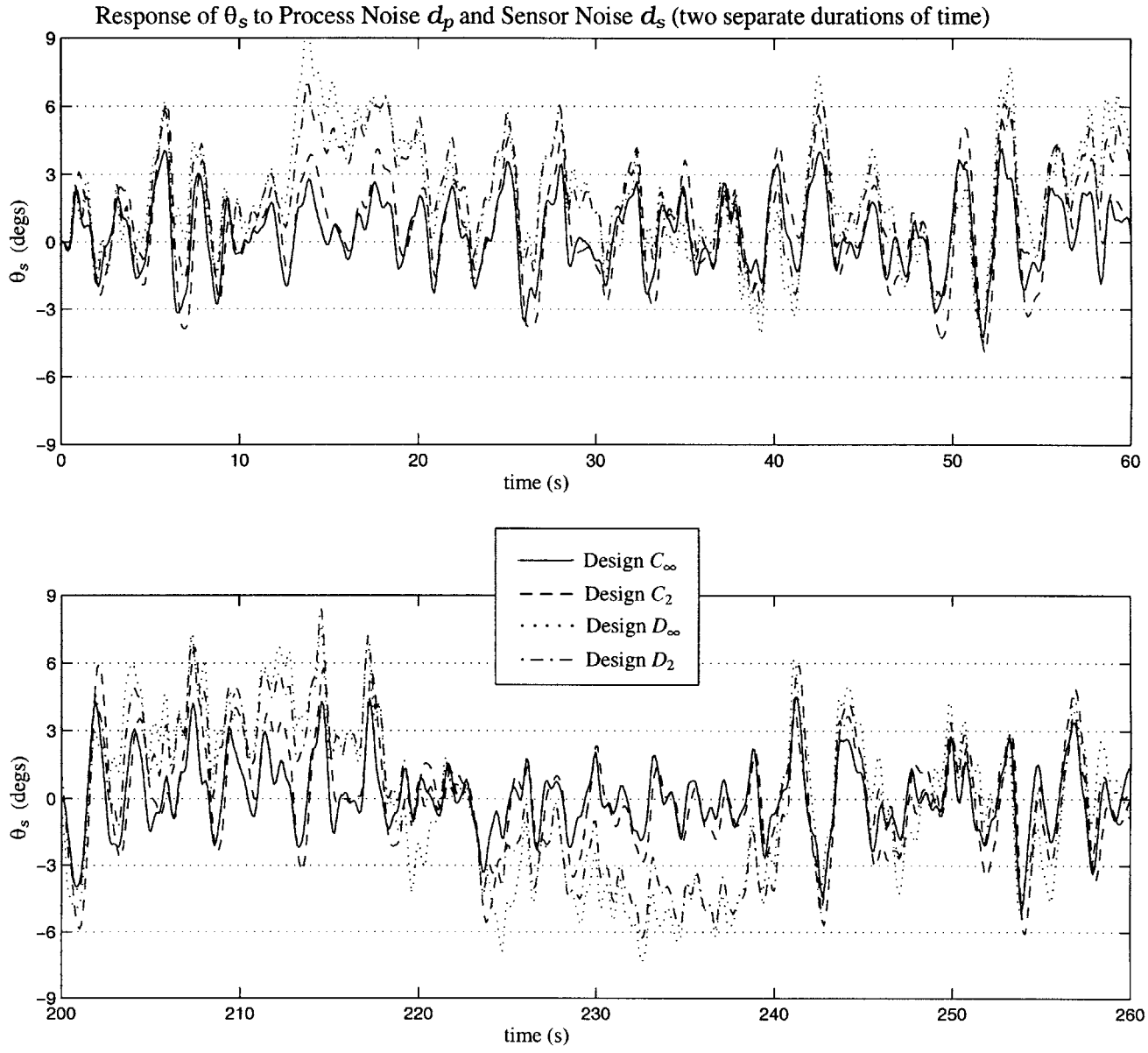

Figure 6-41: Stochastic Response of θ_s to Process Noise d_p and Sensor Noise d_s

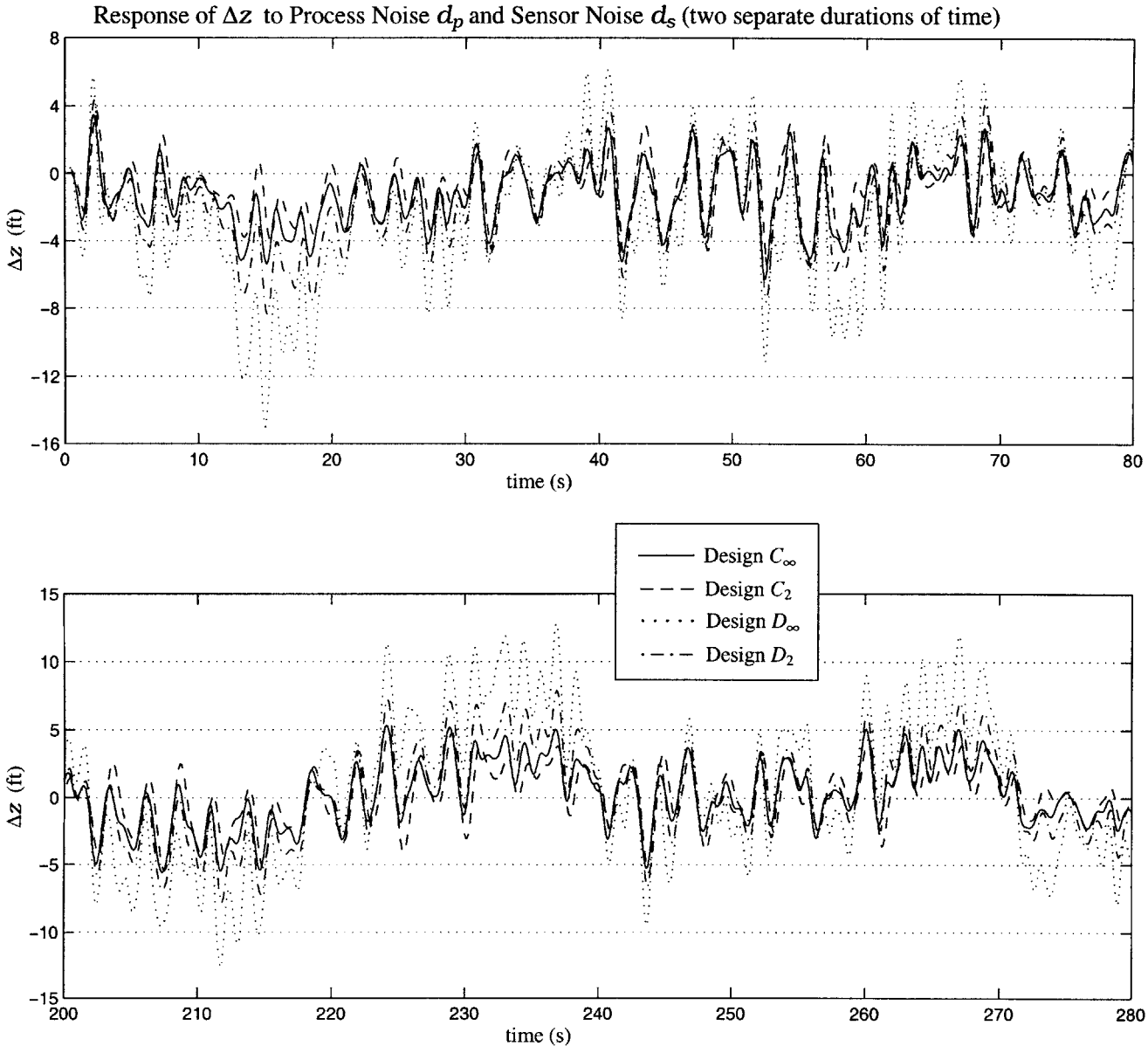

Figure 6-42: Stochastic Response of Δz to Process Noise d_p and Sensor Noise d_s

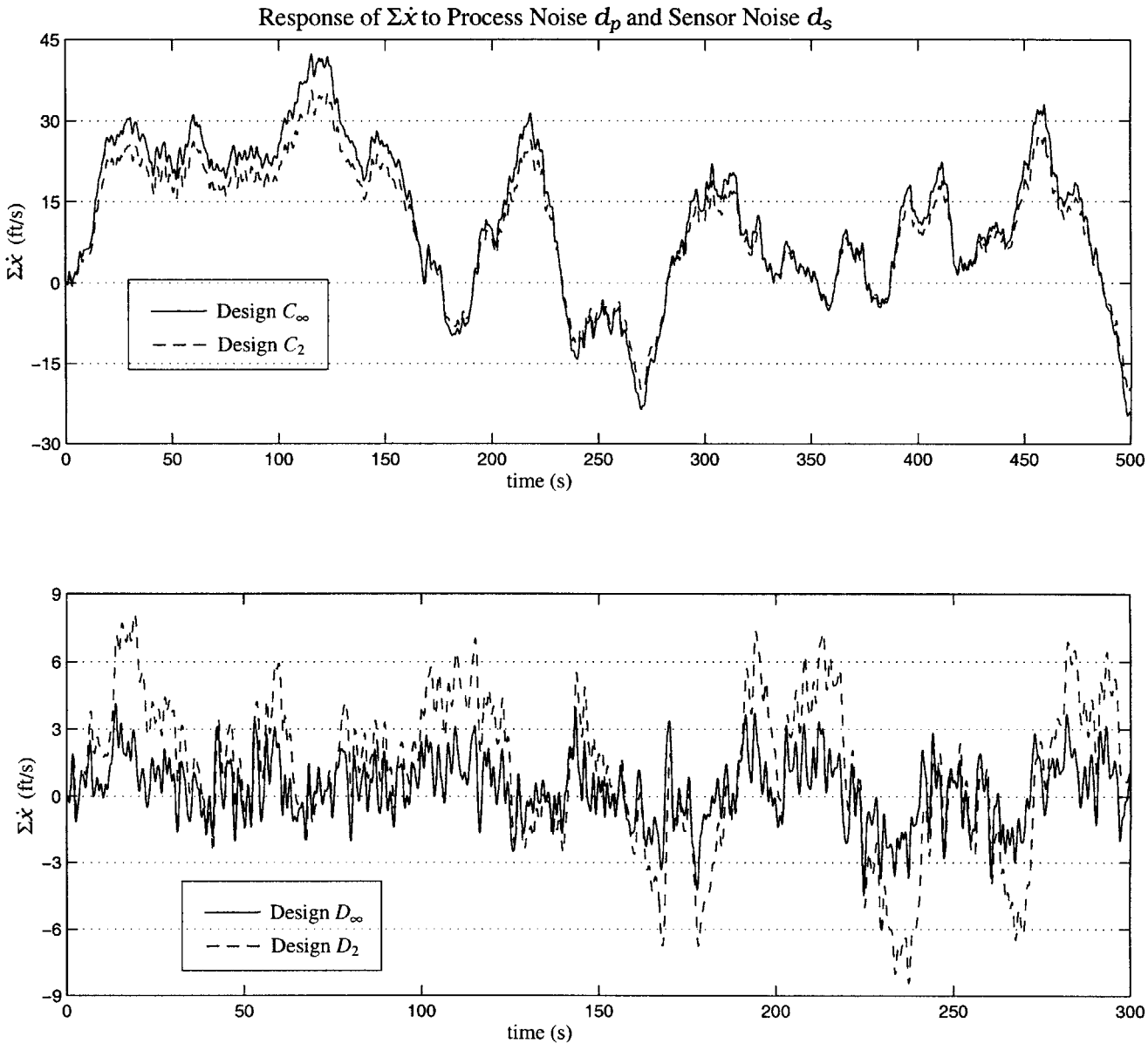

Figure 6-43: Stochastic Response of $\Sigma\dot{x}$ to Process Noise d_p and Sensor Noise d_s

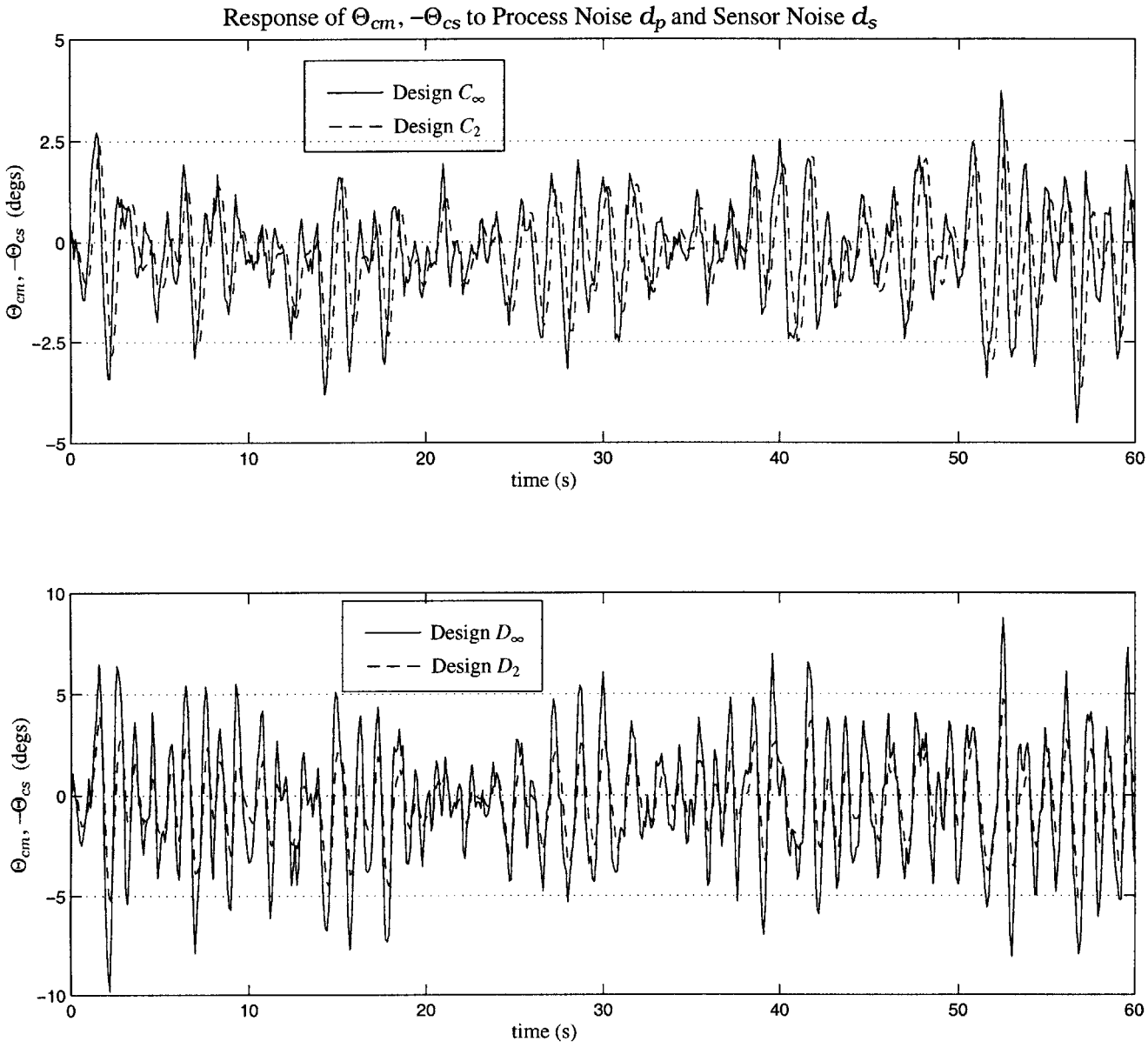

Figure 6-44: Stochastic Response of $\Theta_{cm}, -\Theta_{cs}$ to Process Noise d_p and Sensor Noise d_s

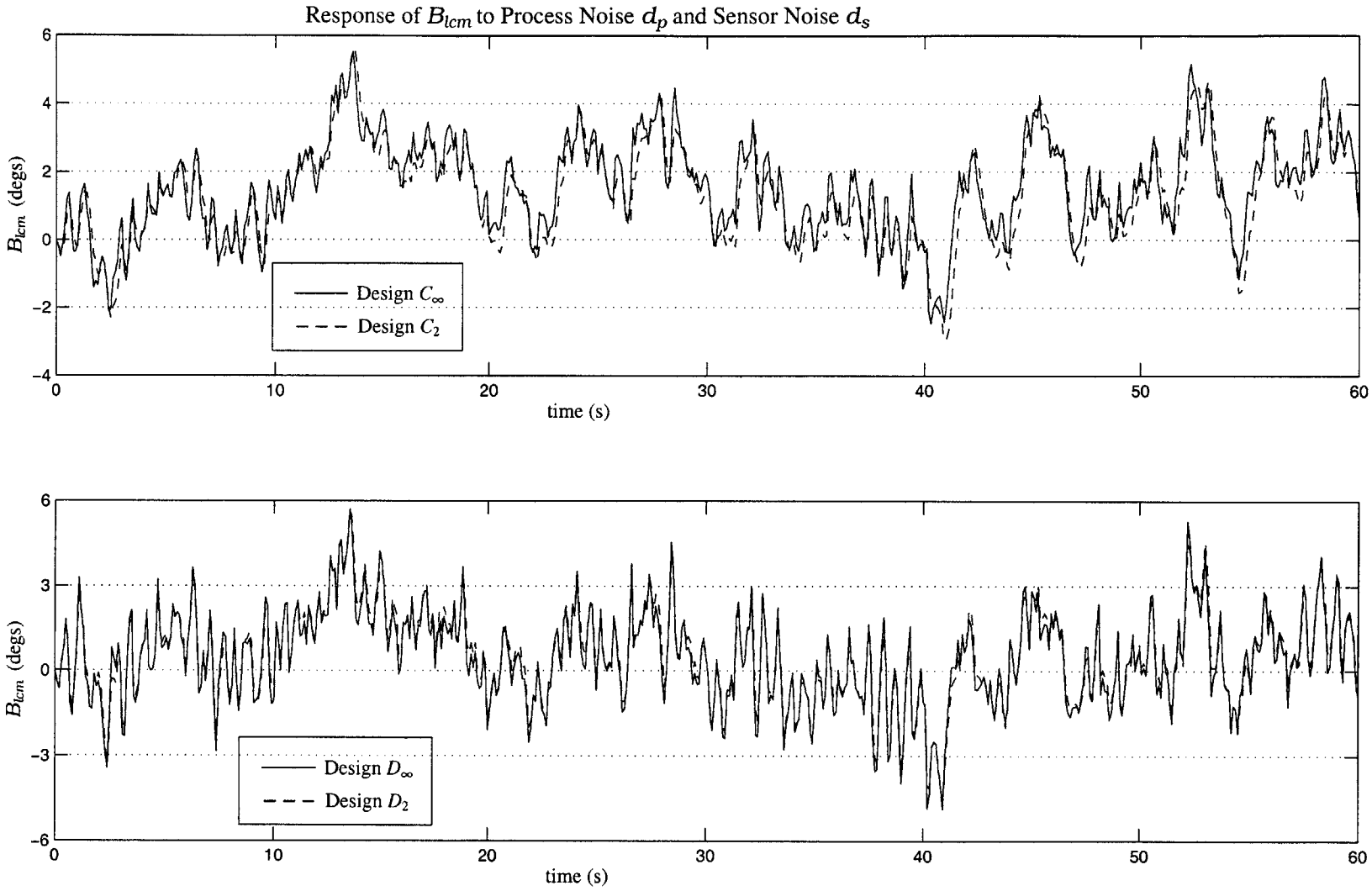

Figure 6-45: Stochastic Response of B_{lcm} to Process Noise d_p and Sensor Noise d_s

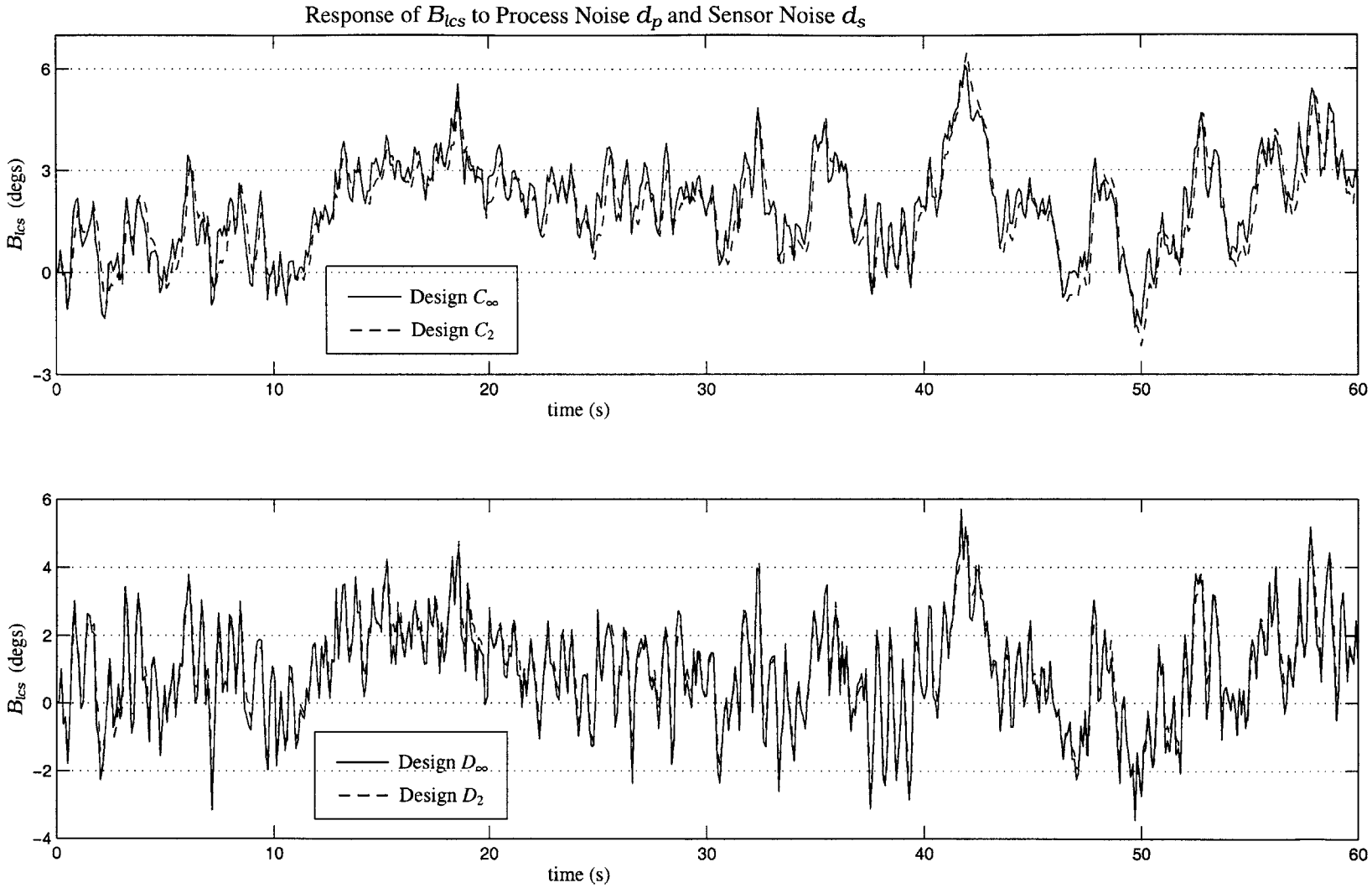

Figure 6-46: Stochastic Response of B_{lcs} to Process Noise d_p and Sensor Noise d_s

responses of θ_m and θ_s are each similar to their corresponding $\mathcal{H}_\infty$ responses, with the primary difference being one of magnitude. In this respect, design $\mathcal{D}_2$ achieves significantly more, and design $\mathcal{C}_2$ significantly less, magnitude reduction. The RMS values for these two $\mathcal{H}_2$ designs are 2.90 and 2.47 respectively. In all of the designs, the stochastic responses of θ_m and θ_s do not exceed the magnitude of 10°, and hence specification (S.3) is satisfied.

The stochastic response of Δz is characterized by high frequency oscillations superimposed with a lower frequency waveform. As with the pitch angles, the lower frequency component of the response becomes more prominent as time progresses, and hence Figure 6-42 shows Δz over two separate time intervals. The responses in designs $\mathcal{C}_\infty$ and $\mathcal{D}_\infty$ oscillate at the same frequencies, but exhibit widely differing magnitude characteristics. In particular, the high frequency component in design $\mathcal{C}_\infty$ oscillates with an average amplitude of around 2.5 ft, whereas that in design $\mathcal{D}_\infty$ shows an average amplitude of around 4 ft. In addition, the lower frequency waveform in design $\mathcal{C}_\infty$ has a smaller amplitude than the higher frequency one, whereas in design $\mathcal{D}_\infty$, the reverse is true. As a result, the magnitude of Δz in design $\mathcal{D}_\infty$ far exceeds that in design $\mathcal{C}_\infty$, a difference reflected in the RMS values for these two designs, of 5.38 and 2.36 respectively. The responses of Δz in the $\mathcal{H}_2$ designs show an oscillatory pattern similar to that in the $\mathcal{H}_\infty$ designs, but with differing magnitude characteristics. In design $\mathcal{C}_2$, the higher frequency component of the response has about the same amplitude as that in design $\mathcal{C}_\infty$, whereas the amplitude of the lower frequency component is significantly smaller. Hence design $\mathcal{C}_2$ shows overall a greater magnitude reduction than design $\mathcal{C}_\infty$, reflected in the RMS value calculated for this $\mathcal{H}_2$ design of 2.17. In design $\mathcal{D}_2$, both the higher and lower frequency components of the response show smaller amplitudes than the corresponding components in design $\mathcal{D}_\infty$. Consequently, design $\mathcal{D}_2$ achieves far greater magnitude reduction than design $\mathcal{D}_\infty$, reflected in the RMS value for this $\mathcal{H}_2$ design of 3.23. In designs $\mathcal{C}_\infty$, $\mathcal{C}_2$, and $\mathcal{D}_2$, the response of Δz never exceeds a magnitude of 8.5 ft, and hence specification (S.4) is satisfied. In design $\mathcal{D}_\infty$, however, the magnitude of Δz repeatedly exceeds the 10 ft magnitude constraint of this specification.

Like Δz, the stochastic response of $\Sigma \dot{x}$ shows a superposition of multiple different frequency waveforms. In designs $\mathcal{D}_\infty$ and $\mathcal{D}_2$, waveforms of two different frequencies are evident. While the amplitudes of the higher frequency components are similar in the two designs, the amplitude of the lower frequency component is much smaller in design $\mathcal{D}_\infty$ than in design $\mathcal{D}_2$. Consequently, design $\mathcal{D}_\infty$ shows significantly greater overall magnitude re-

duction. The RMS values for designs $\mathcal{D}_\infty$ and $\mathcal{D}_2$ are 1.60 and 3.56 respectively. In designs $\mathcal{C}_\infty$ and $\mathcal{C}_2$, the same two waveforms seen in designs $\mathcal{D}_\infty$ and $\mathcal{D}_2$ can be observed, but these waveforms are greatly diminished by their superposition with a third much larger amplitude and lower frequency oscillation. Hence the magnitude of $\Sigma\dot{x}$ in designs $\mathcal{C}_\infty$ and $\mathcal{C}_2$ is much larger than in designs $\mathcal{D}_\infty$ and $\mathcal{D}_2$, with design $\mathcal{C}_\infty$ showing the largest response among the four designs. The RMS values for designs $\mathcal{C}_\infty$ and $\mathcal{C}_2$ are 19.5 and 16.2 respectively. In designs $\mathcal{D}_\infty$ and $\mathcal{D}_2$, $\Sigma\dot{x}$ remains within the 15 ft/s magnitude constraint of specification (S.5). In designs $\mathcal{C}_\infty$ and $\mathcal{C}_2$, however, this constraint is severely and repeatedly violated.

The collective control response in all four designs shows high frequency oscillations which vary periodically in amplitude. While Θ_{cm} $(-\Theta_{cs})$ responds with a similar shape in designs $\mathcal{C}_\infty$ and $\mathcal{D}_\infty$, the former design shows much greater magnitude reduction. The RMS values for these two designs are 1.42 and 3.34 respectively. The $\mathcal{H}_2$ responses are similar in shape to but smaller in magnitude than their corresponding $\mathcal{H}_\infty$ responses, with the magnitude difference between designs $\mathcal{D}_\infty$ and $\mathcal{D}_2$ being far more significant than that between designs $\mathcal{C}_\infty$ and $\mathcal{C}_2$. The RMS values for designs $\mathcal{C}_2$ and $\mathcal{D}_2$ are 1.18 and 1.86 respectively. In all of the designs, the response of Θ_{cm} $(-\Theta_{cs})$ satisfies specification (S.12).

The cyclic control responses in designs $\mathcal{C}_\infty$ and $\mathcal{D}_\infty$ show similar oscillation patterns but differing magnitude characteristics. In each design, B_{lcm} and B_{lcs} exhibit high frequency oscillations superimposed with lower frequency waveforms. However while the lower frequency components in the two designs have similar amplitudes, the higher frequency components are much larger in design $\mathcal{D}_\infty$ than in design $\mathcal{C}_\infty$. In addition, the responses in design $\mathcal{C}_\infty$ are characterized by a positive offset from zero not seen in design $\mathcal{D}_\infty$, and hence design $\mathcal{C}_\infty$ achieves less in the way of overall magnitude reduction. The RMS values for designs $\mathcal{C}_\infty$ and $\mathcal{D}_\infty$ are 2.10 and 1.86 respectively. The $\mathcal{H}_2$ cyclic responses are similar to their corresponding $\mathcal{H}_\infty$ responses, with designs $\mathcal{C}_\infty$ and $\mathcal{C}_2$ showing the more significant contrast. In these two designs, the higher frequency components often differ in amplitude, with design $\mathcal{C}_\infty$ usually, but not always, showing the larger peaks. The cyclic responses in design $\mathcal{C}_2$ also exhibit a slight time lag relative to those in design $\mathcal{C}_\infty$. In designs $\mathcal{D}_\infty$ and $\mathcal{D}_2$, the only significant difference is in the amplitude of the higher frequency components, with that in design $\mathcal{D}_\infty$ generally exceeding that in design $\mathcal{D}_2$. The RMS values for designs $\mathcal{C}_2$ and $\mathcal{D}_2$, at 2.01 and 1.84 respectively, are just slightly smaller than their $\mathcal{H}_\infty$ counterparts. In all of the designs, the responses of B_{lcm} and B_{lcs} satisfy specification (S.13).

6.3.2 Frequency Domain

Figures 6-47 to 6-54 show the maximum singular value plots for each of the controller designs. The first set of plots are for the transfer functions from the wind disturbances, $d_p(t)$, to each of the TLHS regulated variables and controls. These plots also show the frequency domain specifications for process noise rejection put forward in sections 5.2.2.2 and 5.2.3.2 of chapter 5. The last plot, in Figure 6-54, is for the complementary sensitivity function $C(s)$. The two specifications relating to this transfer function are (S.11), for sensor noise rejection, and (S.16), for stability robustness to a time delay. Hence Figure 6-54 also includes markers of the coordinates relevant to specification (S.11), together with a plot of the bounding function in specification (S.16).

6.3.2.1 Wind Disturbance Transfer Functions

Figures 6-47 to 6-53 show the maximum singular values for the transfer functions from $d_p(t)$ to each of the regulated variables and controls. The maximum singular values for $T_{\Delta x, d_p}(j\omega)$ are very similar in shape, but differ in magnitude over the lower frequencies. In

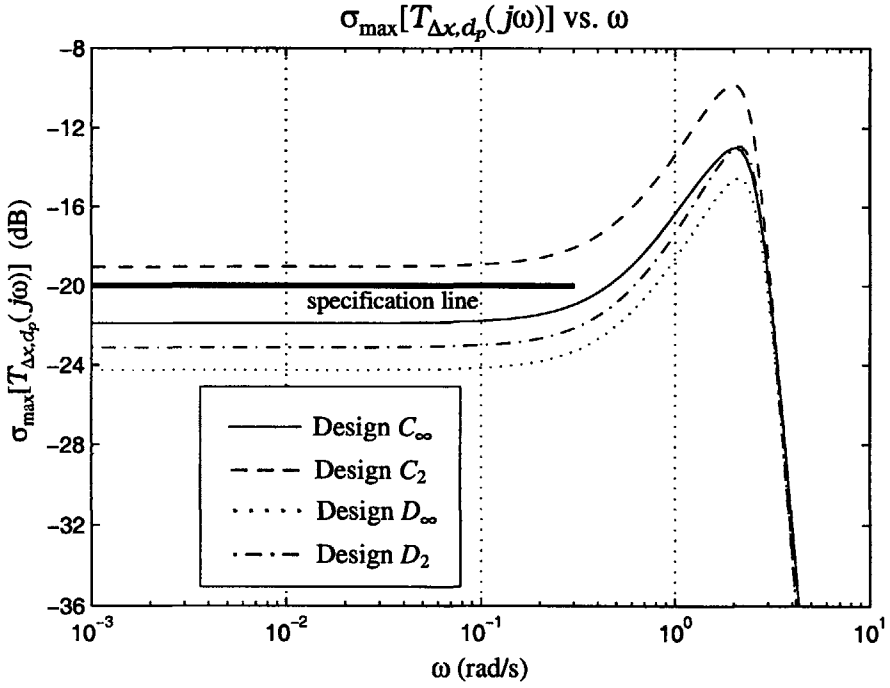

Figure 6-47: Maximum Singular Value of Transfer Function from d_p to Δx

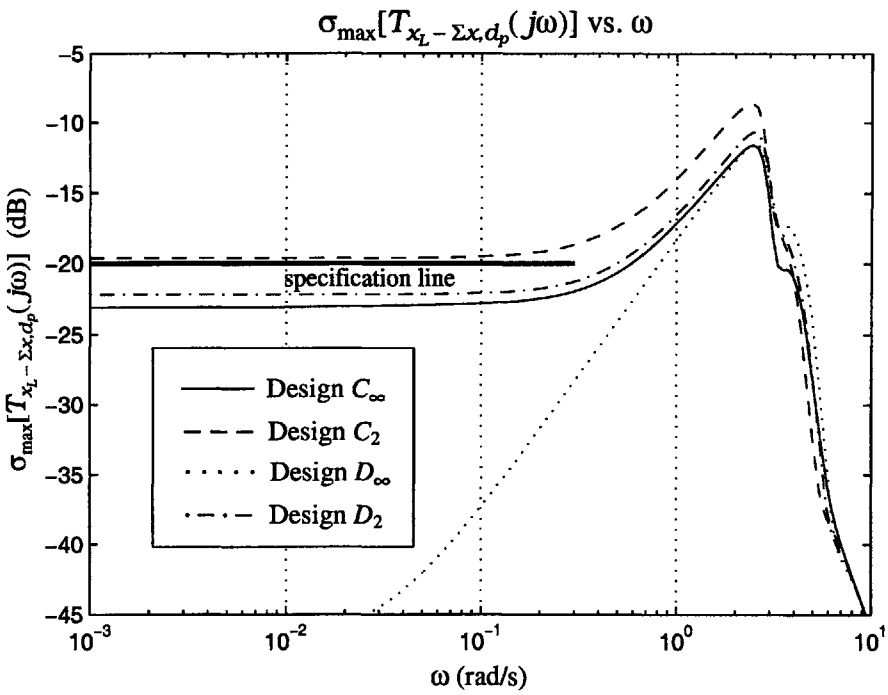

Figure 6-48: Maximum Singular Value of Transfer Function from d_p to $x_L - \Sigma x$

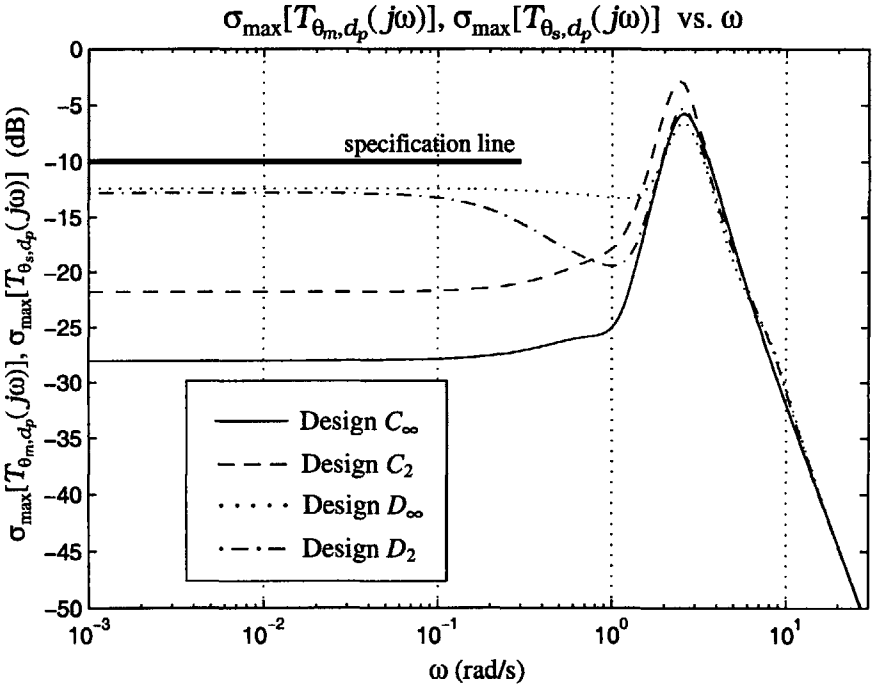

Figure 6-49: Maximum Singular Value of Transfer Function from d_p to θ_m, θ_s

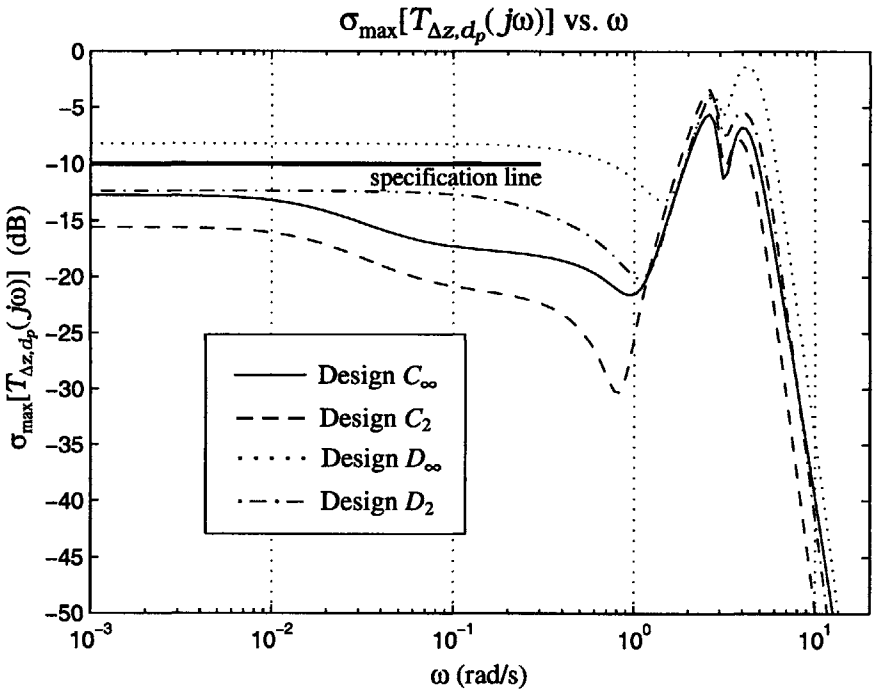

Figure 6-50: Maximum Singular Value of Transfer Function from d_p to Δz

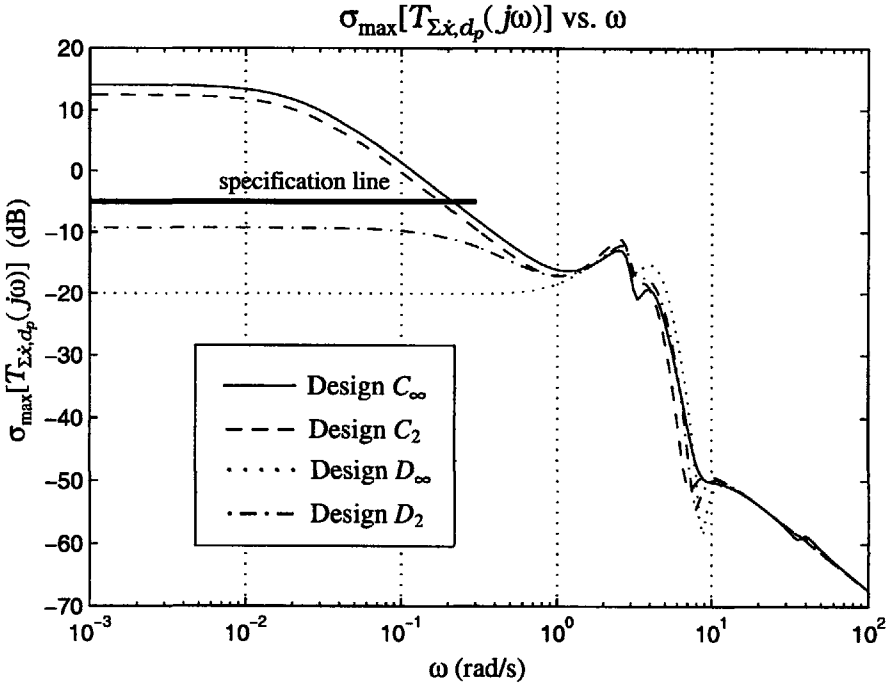

Figure 6-51: Maximum Singular Value of Transfer Function from d_p to $\Sigma\dot{x}$

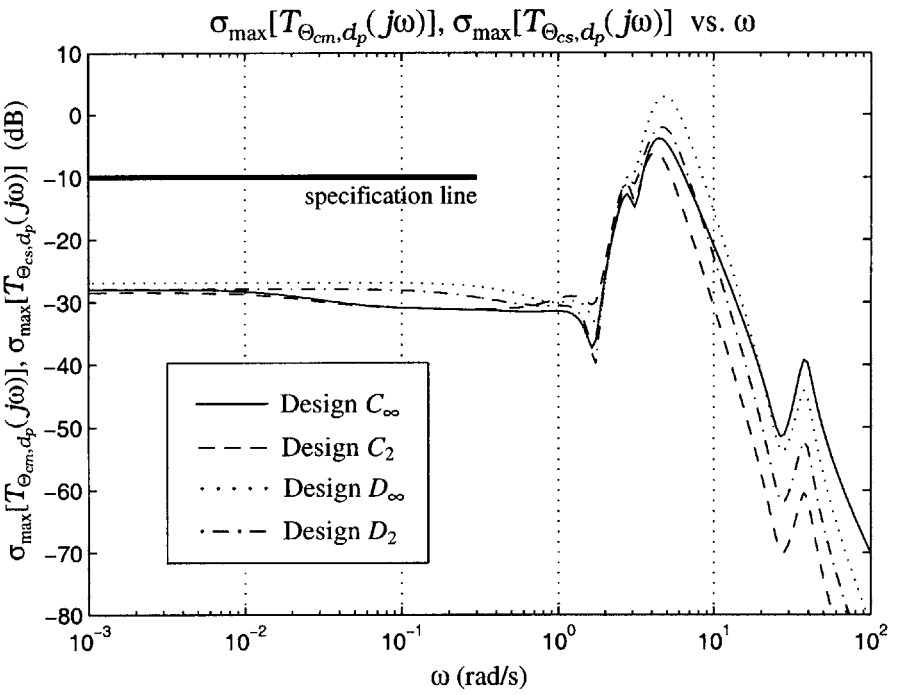

Figure 6-52: Maximum Singular Value of Transfer Function from d_p to Θ_{cm}, Θ_{cs}

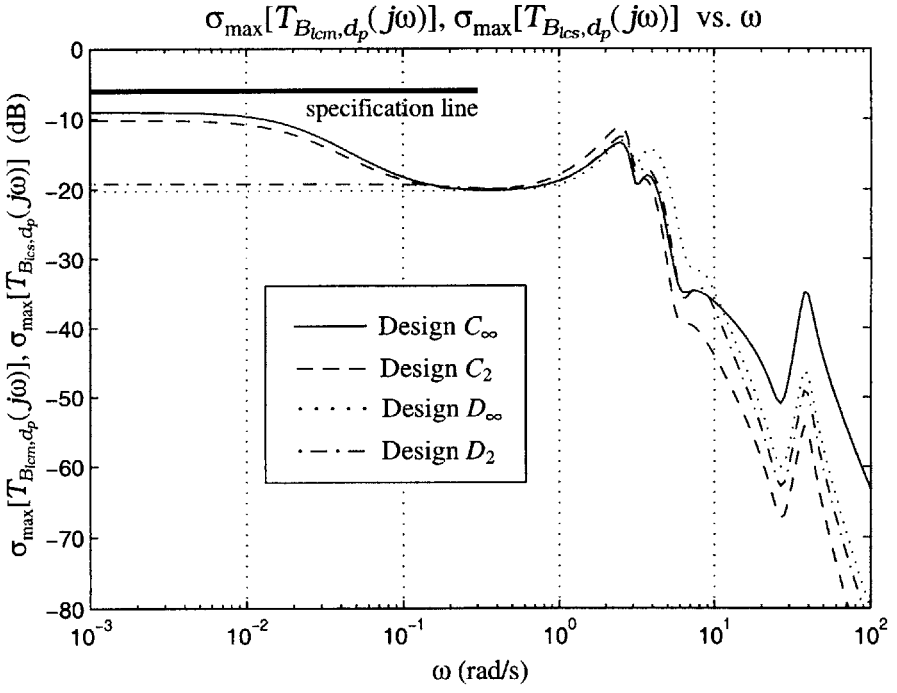

Figure 6-53: Maximum Singular Value of Transfer Function from d_p to B_{lcm}, B_{lcs}

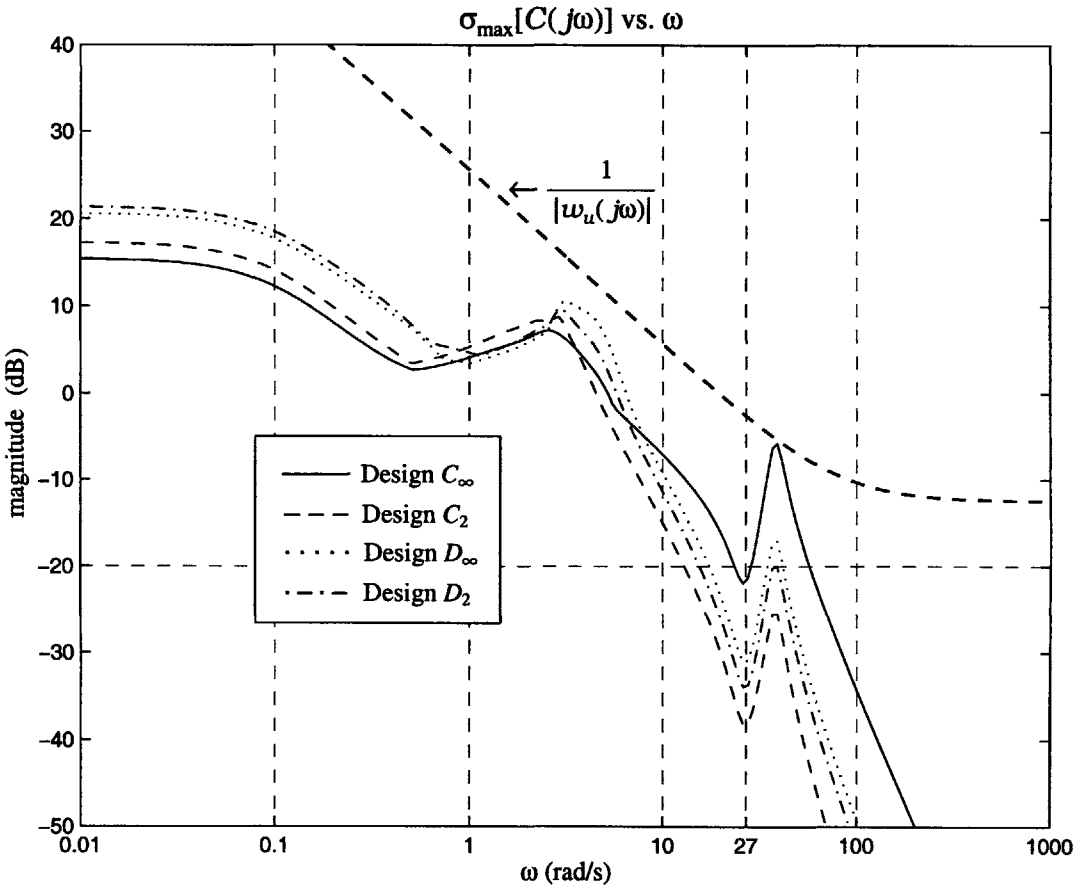

Figure 6-54: Maximum Singular Value of Complementary Sensitivity Function

each design, $\sigma_{\max}[T_{\Delta x,d_p}(j\omega)]$ remains relatively flat until around 0.2 rad/s, and then increases to peak at around 2 rad/s. After peaking, the responses converge and roll off. Before rolling off, design $\mathcal{D}_\infty$ shows the smallest gain, followed in order by design $\mathcal{D}_2$, $\mathcal{C}_\infty$, and lastly $\mathcal{C}_2$. This ordering exactly matches that produced by comparing the RMS values for Δx among the four designs. In designs $\mathcal{D}_\infty$, $\mathcal{D}_2$, and $\mathcal{C}_\infty$, $\sigma_{\max}[T_{\Delta x,d_p}(j\omega)]$ remains below -20 dB for $\omega \leq 0.3$ rad/s, and hence specification (S.6) is satisfied. Recall that the selected weighting functions for loop shaping given in section 5.3.2.2 guaranteed the meeting of this specification by the $\mathcal{H}_\infty$ designs. In design $\mathcal{C}_2$, $\sigma_{\max}[T_{\Delta x,d_p}(j\omega)]$ slightly exceeds the -20 dB constraint for $\omega \leq 0.3$ rad/s, and hence specification (S.6) is violated.

The responses of $\sigma_{\max}[T_{x_L-\Sigma x,d_p}(j\omega)]$ differ in both shape and magnitude over the lower frequencies. In design $\mathcal{C}_\infty$, $\sigma_{\max}[T_{x_L-\Sigma x,d_p}(j\omega)]$ remains relatively flat at around -23 dB until around 0.2 rad/s, at which point the response increases to peak at between 2 and 3 rad/s before rolling off. By contrast, $\sigma_{\max}[T_{x_L-\Sigma x,d_p}(j\omega)]$ in design $\mathcal{D}_\infty$ is not flat over the lower

frequencies, but instead increases steadily from a gain as low as -45 dB at 0.03 rad/s, to eventually peak and converge with the design $\mathcal{C}_\infty$ response. The two $\mathcal{H}_\infty$ designs then show a similar roll off behavior. The $\mathcal{H}_2$ responses show flat gains over the lower frequencies before increasing and peaking in a manner similar to the design $\mathcal{C}_\infty$ response. The flat gains and peaks in the $\mathcal{H}_2$ responses are larger than in the $\mathcal{H}_\infty$ responses, and as with Δx, ordering the designs according to these gains corresponds exactly to the ordering produced by comparing the RMS values for $x_L - \Sigma x$. After peaking, the responses in all four designs converge as they roll off. In designs $\mathcal{D}_\infty$, $\mathcal{C}_\infty$, and $\mathcal{D}_2$, specification (S.7) for process noise rejection is satisfied. As with Δx, the selected weighting functions for loop shaping guaranteed the meeting of this specification by the $\mathcal{H}_\infty$ designs. In design $\mathcal{C}_2$, the gain of $\sigma_{\max}[T_{x_L-\Sigma x,d_p}(\jmath\omega)]$ just slightly exceeds the -20 dB constraint for $\omega \leq 0.3$ rad/s, and hence specification (S.7) is violated.

The singular values for $T_{\theta_m,d_p}(\jmath\omega)$ ($T_{\theta_s,d_p}(\jmath\omega)$) in designs $\mathcal{C}_\infty$ and $\mathcal{D}_\infty$ remain relatively flat over frequencies below 0.2 and 0.7 rad/s respectively, with corresponding gains of around -28 and -12.5 dB. After 0.2 rad/s, the response in design $\mathcal{C}_\infty$ very gradually ascends until around 1 rad/s, and then increases sharply to peak at between 2 and 3 rad/s before rolling off. In design $\mathcal{D}_\infty$, $\sigma_{\max}[T_{\theta_m,d_p}(\jmath\omega)]$ ($\sigma_{\max}[T_{\theta_s,d_p}(\jmath\omega)]$) shows a very gradual descent until slightly over 1 rad/s, at which point the response increases to peak at the same frequency as in design $\mathcal{C}_\infty$, but with a slightly smaller gain. The response in design $\mathcal{D}_\infty$ then rolls off, converging with the design $\mathcal{C}_\infty$ response. In design $\mathcal{C}_2$, the response of $\sigma_{\max}[T_{\theta_m,d_p}(\jmath\omega)]$ ($\sigma_{\max}[T_{\theta_s,d_p}(\jmath\omega)]$) is nearly identical in shape to that in design $\mathcal{C}_\infty$, but shows a larger gain up until around 3.5 rad/s, at which point the two responses converge as they roll off. Over frequencies below 0.2 rad/s, $\sigma_{\max}[T_{\theta_m,d_p}(\jmath\omega)]$ ($\sigma_{\max}[T_{\theta_s,d_p}(\jmath\omega)]$) in design $\mathcal{C}_2$ maintains a relatively constant gain of around -22 dB. Similarly, the response of $\sigma_{\max}[T_{\theta_m,d_p}(\jmath\omega)]$ ($\sigma_{\max}[T_{\theta_s,d_p}(\jmath\omega)]$) in design $\mathcal{D}_2$ closely resembles that in design $\mathcal{D}_\infty$, but shows an earlier descent, at around 0.1 rad/s, and then reaches a significantly lower gain before peaking with a gain slightly larger than that in design $\mathcal{D}_\infty$. The two responses then converge as they roll off. Over frequencies below 0.1 rad/s, design $\mathcal{D}_2$ shows a relatively constant gain just slightly smaller than that in design $\mathcal{D}_\infty$. The relative gains of $\sigma_{\max}[T_{\theta_m,d_p}(\jmath\omega)]$ ($\sigma_{\max}[T_{\theta_s,d_p}(\jmath\omega)]$) over the lower frequencies corresponds exactly with the relative pitch angle RMS values. In all of the designs, the response of $\sigma_{\max}[T_{\theta_m,d_p}(\jmath\omega)]$ ($\sigma_{\max}[T_{\theta_s,d_p}(\jmath\omega)]$) meets specification (S.8).

The responses of $\sigma_{\max}[T_{\Delta z,d_p}(j\omega)]$ in designs $\mathcal{C}_\infty$ and $\mathcal{D}_\infty$ vary both in shape and in magnitude. In design $\mathcal{C}_\infty$, $\sigma_{\max}[T_{\Delta z,d_p}(j\omega)]$ remains relatively flat at around -13 dB until around 0.01 rad/s, at which point the response begins gradually decreasing to a minimum of around -22 dB at around 1 rad/s. The response then increases sharply to peak twice, once at between 2 and 3 rad/s, and again at around 4 rad/s, before rolling off. In design $\mathcal{D}_\infty$, $\sigma_{\max}[T_{\Delta z,d_p}(j\omega)]$ shows a constant gain of about -8 dB until around 0.5 rad/s, at which point the response gradually descends to a minimum of around -14 dB at between 1 and 2 rad/s. The response then increases to peak twice at the same frequencies as the design $\mathcal{C}_\infty$ response, but with larger magnitudes. The two $\mathcal{H}_\infty$ responses roll off together, with that in design $\mathcal{D}_\infty$ showing a slightly larger gain. The responses of $\sigma_{\max}[T_{\Delta z,d_p}(j\omega)]$ in the $\mathcal{H}_2$ designs closely resemble those in the corresponding $\mathcal{H}_\infty$ designs, with several notable differences. First, each $\mathcal{H}_2$ response shows a smaller gain over the lower frequencies, and also dips to a minimum at a slightly lower frequency than does its corresponding $\mathcal{H}_\infty$ response. Second, the amplitude of the first peak in design $\mathcal{C}_2$ is larger than that in design $\mathcal{C}_\infty$, and the amplitudes of the second peaks in both $\mathcal{H}_2$ designs are smaller than those in the corresponding $\mathcal{H}_\infty$ designs. Lastly, the $\mathcal{H}_2$ responses roll off with slightly smaller gains than their corresponding $\mathcal{H}_\infty$ responses. The relative gains of $\sigma_{\max}[T_{\Delta z,d_p}(j\omega)]$ over the lower frequencies corresponds exactly with the relative RMS values calculated for Δz. In designs $\mathcal{C}_\infty$, $\mathcal{C}_2$, and $\mathcal{D}_2$, the response of $\sigma_{\max}[T_{\Delta z,d_p}(j\omega)]$ meets specification (S.9) for process noise rejection. In design $\mathcal{D}_\infty$, however, $\sigma_{\max}[T_{\Delta z,d_p}(j\omega)]$ exceeds the -10 dB constraint for $\omega \leq 0.3$ rad/s, and hence specification (S.9) is violated.

The singular values for $T_{\Sigma\dot{x},d_p}(j\omega)$ show large gain differences between the $\mathcal{C}$ and $\mathcal{D}$ designs over the lower frequencies. In design $\mathcal{C}_\infty$, $\sigma_{\max}[T_{\Sigma\dot{x},d_p}(j\omega)]$ maintains a relatively constant gain of around 14 dB until around 0.02 rad/s, and then slopes to a minimum of around -16 dB at around 1 rad/s. By contrast, design $\mathcal{D}_\infty$ shows a constant gain of -20 dB until around 0.4 rad/s, at which the point the response begins a gentle upward slope. The two responses converge at slightly over 1 rad/s, each peaking at between 2 and 3 rad/s, and again at around 4 rad/s, before rolling off. The $\mathcal{H}_2$ responses closely resemble their corresponding $\mathcal{H}_\infty$ responses, with the primary difference being in the gains over the lower frequencies. In this respect, design $\mathcal{C}_2$ achieves slightly more, and design $\mathcal{D}_2$ significantly less, process noise rejection. The relative gains over the lower frequencies correspond exactly with the relative RMS values calculated for $\Sigma\dot{x}$. While $\sigma_{\max}[T_{\Sigma\dot{x},d_p}(j\omega)]$ in designs $\mathcal{D}_\infty$ and

$\mathcal{D}_2$ remains below the -5 dB constraint of specification (S.10), the large gains in designs $\mathcal{C}_\infty$ and $\mathcal{C}_2$ violate this specification.

In all of the designs, the singular values for $T_{\Theta_{cm},d_p}(j\omega)$ ($T_{\Theta_{cs},d_p}(j\omega)$) show a similar shape. In design $\mathcal{C}_\infty$, $\sigma_{\max}[T_{\Theta_{cm},d_p}(j\omega)]$ ($\sigma_{\max}[T_{\Theta_{cs},d_p}(j\omega)]$) maintains a relatively constant gain of around -28 dB until 0.01 rad/s, and then decreases slightly to maintain another constant gain of around -31 dB at between 0.06 and 1 rad/s. At between 1 and 2 rad/s, the response then dips to a minimum of around -37 dB. In design $\mathcal{D}_\infty$, $\sigma_{\max}[T_{\Theta_{cm},d_p}(j\omega)]$ ($\sigma_{\max}[T_{\Theta_{cs},d_p}(j\omega)]$) remains relatively constant at -27 dB until around 0.2 rad/s, at which point the response gradually decreases to a minimum of -34 dB at slightly under 2 rad/s. At around 2 rad/s, the two $\mathcal{H}_\infty$ responses converge and peak twice, at between 2 and 3 rad/s, and again at between 4 and 5 rad/s, before rolling off. The response of $\sigma_{\max}[T_{\Theta_{cm},d_p}(j\omega)]$ ($\sigma_{\max}[T_{\Theta_{cs},d_p}(j\omega)]$) in design $\mathcal{C}_2$ closely follows that in design $\mathcal{C}_\infty$, but shows a slightly smaller magnitude over frequencies under 0.1 rad/s, a slightly larger magnitude over frequencies between 0.3 and 4 rad/s, and then a smaller magnitude again for frequencies above 4 rad/s. Similarly, the response in design $\mathcal{D}_2$ closely resembles that in design $\mathcal{D}_\infty$, but with a slightly smaller gain throughout. The ordering of the gains over the lower frequencies exactly matches the ordering of the RMS values calculated for Θ_{cm} (Θ_{cs}). Also note that in all of the designs, $\sigma_{\max}[T_{\Theta_{cm},d_p}(j\omega)]$ ($\sigma_{\max}[T_{\Theta_{cs},d_p}(j\omega)]$) shows a downward peak at around 27 rad/s, the frequency where sensor noise energy is greatest. The response of $\sigma_{\max}[T_{\Theta_{cm},d_p}(j\omega)]$ ($\sigma_{\max}[T_{\Theta_{cs},d_p}(j\omega)]$) in all of the designs easily meets specification (S.14).

The responses of $\sigma_{\max}[T_{B_{lcm},d_p}(j\omega)]$ ($\sigma_{\max}[T_{B_{lcs},d_p}(j\omega)]$) in designs $\mathcal{C}_\infty$ and $\mathcal{D}_\infty$ differ significantly in magnitude at frequencies below 0.01 rad/s, with approximately constant gains of around -9 and -20 dB respectively. The response in design $\mathcal{C}_\infty$ then decreases to -20 dB, converging with that in design $\mathcal{D}_\infty$ at around 0.2 rad/s. After peaking at between 2 and 3 rad/s, the two responses then roll off, exhibiting several peaks and dips in the process. The response in design $\mathcal{C}_2$ is similar to that in design $\mathcal{C}_\infty$, but with a slightly smaller gain over frequencies below 0.2 rad/s, a slightly larger gain over frequencies between 0.2 and 3 rad/s, and a smaller gain at frequencies above 3 rad/s. Similarly, the response of $\sigma_{\max}[T_{B_{lcm},d_p}(j\omega)]$ ($\sigma_{\max}[T_{B_{lcs},d_p}(j\omega)]$) in design $\mathcal{D}_2$ closely follows that in design $\mathcal{D}_\infty$, but shows a slightly larger gain over frequencies below 3 rad/s, and a slightly smaller gain for frequencies above 3 rad/s. Consistent with the relative singular value magnitudes over frequencies under 0.2 rad/s, the RMS values for B_{lcm} (B_{lcm}) in designs $\mathcal{D}_\infty$ and $\mathcal{D}_2$ are

smaller than those in designs $\mathcal{C}_\infty$ and $\mathcal{C}_2$. While the RMS in design $\mathcal{C}_\infty$ is slightly larger than that in design $\mathcal{C}_2$, the RMS in design $\mathcal{D}_\infty$ just slightly exceeds that in design $\mathcal{D}_2$. This RMS reduction by design $\mathcal{D}_2$ over design $\mathcal{D}_\infty$ becomes a slight amplification, however, when the sensor noise is not included as an input. As with the collective control, $\sigma_{\max}[T_{B_{lcm},d_p}(j\omega)]$ ($\sigma_{\max}[T_{B_{lcs},d_p}(j\omega)]$) in all of the designs shows a downward peak at around 27 rad/s. All of the cyclic responses meet specification (S.15) for process noise rejection.

6.3.2.2 Complementary Sensitivity Function

Figure 6-54 shows the maximum singular values of $C(j\omega)$ for all four designs, together with the bounding function $1/|w_u(j\omega)|$ in specification (S.16). The coordinates 27 rad/s and -20 dB are also marked for assessing the meeting of specification (S.11). All of the responses of $\sigma_{\max}[C(j\omega)]$ follow a similar shape, showing a downward peak at 27 rad/s followed by an upward peak at around 40 rad/s. In all of the designs, the downward peaks fall beneath -20 dB, and hence specification (S.11) for sensor noise rejection is satisfied. At this downward peak frequency of 27 rad/s, the $\mathcal{H}_2$ responses show smaller gains than the $\mathcal{H}_\infty$ responses, with design $\mathcal{C}_\infty$ showing the least amount of magnitude reduction among the four designs. As with specification (S.11), specification (S.16) for stability robustness is also met by all four designs. While designs $\mathcal{C}_2$, $\mathcal{D}_\infty$, and $\mathcal{D}_2$ meet this specification with some remaining margin for error, the response in design $\mathcal{C}_\infty$ peaks at 40 rad/s to nearly touch the bounding function in this specification.

6.3.3 Conclusions

Both of the $\mathcal{H}_\infty$ controller designs, $\mathcal{C}_\infty$ and $\mathcal{D}_\infty$, meet all of the specifications considered mandatory for acceptable design performance. The nature of the responses in each design, however, differ considerably. The two designs also vary in the extent to which they each meet (or do not meet) the specifications, both those mandatory and those desirable. These differences are often explainable in terms of variations in the output matrix and weighting functions used to construct the respective generalized plants.

In general, design $\mathcal{C}_\infty$ achieves superior performance in the regulated variables θ_m (θ_s) and Δz, whereas design $\mathcal{D}_\infty$ achieves superior performance in the regulated variables Δx and $\Sigma\dot{x}$. These performance differences are most pronounced in the stochastic simulations and wind-to-variable singular value plots. In design $\mathcal{C}_\infty$, $\Sigma\dot{x}$ violates specification (S.5) in

the stochastic simulation, as well as specification (S.10) in the plot of $\sigma_{\max}[T_{\Sigma\dot{x},d_p}(j\omega)]$. This reduced performance of $\Sigma\dot{x}$ results from the omission of this variable as one of the outputs. Design $\mathcal{C}_\infty$ not having $\Sigma\dot{x}$ as an output, however, translates into more focused control on $\Sigma\theta$, and hence design $\mathcal{C}_\infty$ shows much greater magnitude reduction in θ_m (θ_s) than design does $\mathcal{D}_\infty$. This improved performance in the pitch angle response is accompanied by a significant improvement in the response of Δz. Hence, in design $\mathcal{C}_\infty$, Δz meets both specification (S.4) in the stochastic simulation and specification (S.9) in the plot of $\sigma_{\max}[T_{\Delta z,d_p}(j\omega)]$, whereas in design $\mathcal{D}_\infty$, both of these specifications are violated. The collective control in design $\mathcal{C}_\infty$ is consistently significantly smaller than that in design $\mathcal{D}_\infty$. Conversely, design $\mathcal{D}_\infty$ usually shows a smaller magnitude cyclic. As seen in Figure 6-54, while both designs meet specification (S.16) for stability robustness, $\sigma_{\max}[C(j\omega)]$ in design $\mathcal{C}_\infty$ peaks much higher than in design $\mathcal{D}_\infty$ at around 40 rad/s, actually touching the bounding function in this specification. Over the lower frequencies, however, $\sigma_{\max}[C(j\omega)]$ in design $\mathcal{C}_\infty$ actually shows a smaller gain than in design $\mathcal{D}_\infty$. Table 5.5 shows that in these two $\mathcal{H}_\infty$ designs, the selected weighting functions $w_2(s)$, used to shape $\sigma_{\max}[C(j\omega)]$, differ only by a constant scaling factor. This scaling factor was introduced into design $\mathcal{C}_\infty$ to ensure that $\sigma_{\max}[C(j\omega)]$ achieve the sensor noise rejection requirement. Figure 6-54 shows that both $\mathcal{H}_\infty$ designs do indeed meet specification (S.11) for sensor noise rejection. The success of meeting this specification is also seen by comparing the RMS values in Tables 6.3 and 6.4. In each design, the difference between output RMS values with the sensor noise input and without it, is negligible.

Each $\mathcal{H}_2$ design differs significantly from its corresponding $\mathcal{H}_\infty$ design, and these differences exhibit some noticeable trends. In general, the $\mathcal{H}_\infty$ designs achieve greater magnitude reduction in the variables included among the outputs, whereas the $\mathcal{H}_2$ designs achieve greater magnitude reduction in the other regulated variables and in the controls. These differences are most apparent in the stochastic simulations and the wind-to-variable singular value plots. In addition, the deterministic time domain simulations show that the $\mathcal{H}_\infty$ designs generally produce faster responses, both in the regulated variables and in the controls, than the corresponding $\mathcal{H}_2$ designs. The $\mathcal{H}_2$ designs, however, achieve more in the way of stability robustness and sensor noise rejection, with the differences between designs $\mathcal{C}_2$ and $\mathcal{C}_\infty$ being especially prominent in this regard.

In design $\mathcal{C}_2$, the TLHS generally produces larger magnitudes in Δx, $x_L - \Sigma x$, and θ_m

(θ_s) than in design $\mathcal{C}_\infty$, but shows greater magnitude reduction in Δz, $\Sigma\dot{x}$, Θ_{cm} (Θ_{cs}), and B_{lcm} (B_{lcs}). The only exception to this pattern is in the pitch angle response to (IC.1), where θ_m ($-\theta_s$) in design $\mathcal{C}_\infty$ initially oscillates with a larger amplitude than in design $\mathcal{C}_2$. The poorer performance of design $\mathcal{C}_2$ in regulating Δx and $x_L - \Sigma x$ leads to the violation by this design of the time and frequency domain specifications (S.1) and (S.6) on Δx, and the frequency domain specification (S.7) on $x_L - \Sigma x$. While design $\mathcal{C}_2$ does achieve greater magnitude reduction in $\Sigma\dot{x}$ than design $\mathcal{C}_\infty$, the former design still violates the time and frequency domain specifications (S.5) and (S.10) on this variable. Figure 6-54 shows that design $\mathcal{C}_2$ achieves the greatest amount of sensor noise rejection among the four designs, and compared to design $\mathcal{C}_\infty$, meets the stability robustness requirement with a much larger margin for error.

In design $\mathcal{D}_2$, the TLHS generally produces larger magnitudes in Δx, $x_L - \Sigma x$, and $\Sigma\dot{x}$ than in design $\mathcal{D}_\infty$, but shows greater magnitude reduction in θ_m (θ_s), Δz, Θ_{cm} (Θ_{cs}), and B_{lcm} (B_{lcs}). The only exceptions to this pattern are in the responses of θ_m ($-\theta_s$) to (IC.1) and $x_L - \Sigma x$ to (IC.2). The variables Δz and $\Sigma\dot{x}$ show the largest magnitude contrasts between the two designs. Conversely, the cyclic control responses exhibit only very small magnitude differences. As a result of the greater magnitude reduction in Δz produced by design $\mathcal{D}_2$, this design, unlike design $\mathcal{D}_\infty$, satisfies both the time and frequency domain specifications (S.4) and (S.9) on this variable. Figure 6-54 shows that the response of $\sigma_{\max}[C(j\omega)]$ in design $\mathcal{D}_2$ is very similar to that in design $\mathcal{D}_\infty$, but achieves slightly better sensor noise rejection, and meets the stability robustness requirement with a slightly greater margin for error.

6.4 Conclusion

Both the $\mathcal{H}_2$ and $\mathcal{H}_\infty$ design methodologies with frequency weightings produce controllers that satisfy the mandatory design specifications put forward in chapter 5. Within each approach, performance trade offs are achieved through intuitive variations in the output matrices and weighting functions. Such trade offs include improved performance in the regulated variable $\Sigma\dot{x}$ and improved stability robustness, resulting from including the variable $\Sigma\dot{x}$ as a fourth output, versus improved performance in the regulated variables θ_m (θ_s) and Δz, resulting from having only three outputs. The design selected for implementation

will depend on which specifications are deemed the most important. In general, the $\mathcal{H}_\infty$ approach to design produces the desired results more efficiently than the $\mathcal{H}_2$ approach. This greater efficiency is attributable to the predictability inherent in using frequency weights for direct loop shaping, especially when design requirements are specified in the frequency domain. Both methodologies, however, provide an intuitive and effective means for achieving the performance and stability robustness desired of the closed loop system.

Chapter 7

Conclusion

7.1 Summary

In this thesis, the $\mathcal{H}_2$ and $\mathcal{H}_\infty$ control methodologies are used to design automatic flight control systems for a twin lift helicopter system. The theory of the two methodologies is developed within a generalized plant framework, where the goal of $\mathcal{H}_2$ and $\mathcal{H}_\infty$ control is to minimize the "size" of this generalized plant with feedback from the controller. The norms used to measure this plant's size, and which differentiate the two methodologies, are defined and interpreted, and characteristics of each type of controller discussed. The theoretical development concludes with a discussion and illustration of how frequency dependent weighting functions can be incorporated into the generalized plant to target specific performance and stability robustness requirements on the closed loop system. Particular emphasis is placed on the ability in $\mathcal{H}_\infty$ design to use design weights for direct singular value loop shaping.

After establishing the theoretical framework for $\mathcal{H}_2$ and $\mathcal{H}_\infty$ control, these two methodologies are applied to control a twelfth order multi-input multi-output TLHS. To motivate the generalized plant designs for controller synthesis, performance and stability robustness specifications are put forward based upon assumed external disturbances and an assumed unmodeled time delay of up to 0.05 s. With these specifications established, four generalized plants, two for $\mathcal{H}_2$ and two for $\mathcal{H}_\infty$ synthesis, are designed, with the parameters and weighting functions for these plants targeted to achieve the performance and stability robustness objectives. Analysis of the resulting controllers reveals that both the $\mathcal{H}_2$ and $\mathcal{H}_\infty$ design methodologies, when used with frequency weightings, are able to meet the specifications put

forward for closed loop system behavior. Differences and performance trade offs amongst the controllers are shown to correlate intuitively with variations in the weighting functions and other parameters used to define the generalized plant. In addition, the ability in $\mathcal{H}_\infty$ design, but not $\mathcal{H}_2$ design, to directly shape singular values, makes this former approach generally more efficient in producing the desired results. The controller analyses illustrate, however, that both design methodologies provide an intuitive and effective means within the multivariable setting for specifically targeting, and hence achieving, the performance and stability robustness desired of the closed loop system.

7.2 Future Work

The two design methodologies described and applied in this thesis can be readily used to design controllers for any number of multi-input multi-output systems. Frequency weightings can be constructed to represent particular stability robustness and performance requirements, and the weightings can be placed in a configuration similar to, or very different from, that shown in Figure 4-4. In addition, future work might extend the Small Gain Theorem and $\mathcal{H}_\infty$ loop shaping to enable non-conservative controller analysis and synthesis for stability robustness to "structured" uncertainty and/or for performance robustness [11], [12], [9]. Such an extension involves computing the *structured singular value* [13], and much research has been done to demonstrate the power and versatility of making such a computation. See [14], [15], [16], [17], and [18] for additional information on the structured singular value, its computation, and its applications.

Bibliography

[1] H. C. Curtiss Jr. and F. W. Warburton. Stability and control of the twin lift helicopter system. *American Helicopter Society*, pages 33–48, May 1984.

[2] Armando A. Rodriguez. Multivariable control of a twin lift helicopter system. Master's thesis, Massachusetts Institute of Technology, May 1987.

[3] A. R. S. Bramwell. *Helicopter Dynamics.* John Wiley and Sons, New York, 1976.

[4] Michael Athans. 6.245 class notes. For graduate course at Massachusetts Institute of Technology, 1997.

[5] Leonard Lublin, Simon Grocott, and Michael Athans. $\mathcal{H}_2$ (LQG) and $\mathcal{H}_\infty$ control. In W. S. Levine, editor, *The Control Handbook*, chapter 40, pages 651–661. CRC Press Inc., 1996.

[6] Munther Dahleh, George Verghese, and Mohammed Dahleh. 6.241 class notes. For graduate course at Massachusetts Institute of Technology, 1996.

[7] Leonard Lublin and Michael Athans. Linear quadratic regulator control. In W. S. Levine, editor, *The Control Handbook*, chapter 39, pages 635–650. CRC Press Inc., 1996.

[8] Alan Chao and Michael Athans. Stability robustness to unstructured uncertainty for linear time invariant systems. In W. S. Levine, editor, *The Control Handbook*, chapter 30, pages 519–535. CRC Press Inc., 1996.

[9] Gary J. Balas, John C. Doyle, Keith Glover, Andy Packard, and Roy Smith. *μ-Analysis and Synthesis Toolbox.* MUSYN Inc. and The Mathworks, Inc., Apr 1991.

[10] Michael Athans. 6.245 class problem sets. For graduate course at Massachusetts Institute of Technology, 1997.

[11] John Doyle. Analysis of feedback systems with structured uncertainties. *IEE Proceedings*, 129(6):242–250, Nov 1982.

[12] John C. Doyle. Structured uncertainty in control system design. In *Proceedings of the 24th IEEE Conference on Decision and Control*, pages 260–265, Fort Lauderdale, FL, Dec 1985.

[13] Gary J. Balas and Andy Packard. The structured singular value (μ) framework. In W. S. Levine, editor, *The Control Handbook*, chapter 42, pages 671–687. CRC Press Inc., 1996.

[14] Michael K. H. Fan, André L. Tits, and John C. Doyle. Robustness in the presence of mixed parametric uncertainty and unmodeled dynamics. *IEEE Transactions on Automatic Control*, 36(1):25–38, Jan 1991.

[15] Peter M. Young, Mathew P. Newlin, and John C. Doyle. Computing bounds for the mixed μ problem. *International Journal of Robust and Nonlinear Control*, 5:573–590, 1995.

[16] Leonard Lublin. *The Use of Additional Actuators to Enhance Performance Robustness.* PhD thesis, Massachusetts Institute of Technology, Jun 1996.

[17] Gunter Stein and John C. Doyle. Beyond singular values and loop shapes. *Journal of Guidance, Control, and Dynamics*, 14(1):5–16, Jan-Feb 1991.

[18] Peter M. Young and John C. Doyle. Computation of μ with real and complex uncertainty. In *Proceedings of the 29th IEEE Conference on Decision and Control*, volume 3, pages 1230–1235, Honolulu, HI, Dec 1990.